The Development of an *in-situ* ATR-FTIR Technique for the Study of Nanomaterials

A Thesis

Presented to

The Faculty of Graduate Studies

Lakehead University

By

R. Matthew Asmussen

In partial fulfillment of the requirements

For the degree of

Master of Science

September 2009

Abstract

Robert Matthew Asmussen
Lakehead University, 2009
Advisor: Dr. Aicheng Chen

The Fourier Transform Infrared Spectroscopy technique utilizes a short acquisition time and high sensitivity to function as a strong analytical tool in electrochemical studies. This work will focus on the development of an ATR-FTIR technique and its introduction into our laboratory.

The ATR-FTIR technique was designed to gather information from two areas of an electrochemical system: an internal system for the monitoring of species at a catalyst surface, and an external system to detect species as they desorb from the catalyst surface. With the systems designed, their performance was characterized using the adsorption of CO and its electro-oxidation on Pt and the electrochemical oxidation of methanol. The functional systems were then utilized in the study of nanostructured materials.

The nanostructured materials were fabricated using a hydrothermal technique. Upon fabrication, the nanomaterials were characterized using scanning electron microscopy (SEM), energy dispersive X-ray spectrometry (EDS), x-ray diffraction (XRD) and x-ray photoelectron spectroscopy (XPS). Their electrochemical properties were monitored by using cyclic voltammetry (CV), chronoamperometry (CA), and linear voltammetry (LV).

A novel trimetallic PtRuIr catalyst was prepared to improve on the performance of the PtRu catalyst in the oxidation of methanol. A nanoporous structure was observed with SEM and XRD data identified a face-centered cubic structure for the catalyst. In the oxidation of methanol, the PtRuIr outperforms the PtRu . This process was monitored with ATR-FTIR, and a change in

the behaviour of water species in addition to a lower level of CO-poisoning at the electrode surface lead to the enhanced performance.

Nanoporous Pt, PtRu, PtIr and PtPb were also prepared to test their potential as a non-enzymatic glucose sensor. The oxidation of glucose at nanostructured surfaces is not yet fully understood but is a key to the development of a functional sensor. Several poisoning species can arise as intermediates during the complete oxidation of glucose, and the addition of a co-catalyst to a Pt catalyst can improve performance. From the ATR-FTIR analysis of the oxidation of glucose, PtPb is clearly the most promising catalyst as the final product, CO_2, is observed without the formation of a CO poisoning intermediate.

More complex nanostructured materials, PtPd and PtPb nanodendrites, were also studied. A 50:50 PtPb nanodendrites system shows the strongest performance towards the oxidation of formic acid. A phase conversion from face-centered cubic to hexagonal (from 0% Pb to 50% Pb) is observed from XRD, and with an ATR-FTIR analysis, it is found that this phase conversion prevents CO from adsorbing to the PtPb catalyst surface. A 50:50 PtPd nanodendritic system shows the highest performance in the oxidation of methanol. Its improvement arises from a different source, a synergistic effect between the Pt and Pd sites. These highly ordered systems represent a key step in the integration of nanosystems into our everyday life.

The versatility of the ATR-FTIR was also studied in the degradation of nitrophenol molecules. This study was based on the strong performance of photoelectrochemical bifunctional electrodes. The ATR-FTIR technique allows for monitoring of intermediate species from a photochemical TiO_2 surface, one of which is an increase in aromatic-OH species, leading to the eventual degradation to CO_2. This data is important in understanding the degradation mechanisms of organic pollutants. The system also monitored the electrochemical oxidation of

nitrophenol using a Ti/Ta_2O_5-IrO_2 electrode. All the above results have demonstrated that the in situ electrochemical ATR-FTIR systems developed during my M.Sc. project are powerful techniques to study nanostructured catalyst – solution interfaces for medical and environmental applications.

Acknowledgements

I would like to thank my supervisor, Dr. Aicheng Chen, for his guidance and wisdom while pursuing my M. Sc. degree. I would also like to thank my committee members Dr. Robert Mawhinney and Dr. Craig MacKinnon for their insight and feedback on my thesis.

I would like to thank my fellow lab mates, former and current, Jingpeng Wang, Kallum Koczkur, Brad Miller, Brian Adams, Peter Holt-Hindle, Stephanie Nigro, Linda Bakovic, Duncan MacDonald, Samantha Nigro, Nelson Matayovsky, Paul Benvenuto, Rasha Tolba, Cassie Ostrom, Monica Malig, Jiali Wen, Asieh Amahjedizan, Dr. Q. Yi, Dr. G. Wu, Dr . AKM Kafi, A special thank you to Dr. Min Tian for his extended assistance and insight throughout my studies. A special thank you goes to Ed Drotar for his help in the Science Workshop and Al MacKenzie and Keith Pringnitz for their assistance in the L.U. Instrumentation lab.

Finally I would like to thank my parents and brother and sister for their love and support. To all of my close friends through the years, especially you for helping to keep my sanity during my writing, the YMFT hockey team, the Labatt brewing company, and the rest of the chemistry department at Lakehead University I extend a big thank you.

Table of Contents

Table of Figures

List of Tables

List of Abbreviations and Symbols

AIRE	Abnormal Infrared Effects
ATR	Attenuated Total Reflection
CA	Chronoamperometry
CP	Chronopotentiometry
CV	Cyclic Voltammetry
EDS	Energy Dispersive Spectroscopy
EIS	Electrochemical Impedance Spectroscopy
FTIR	Fourier Transform Infrared Spectroscopy
GC	Gas Chromatography
HPLC	High Performance Liquid Chromatography
IR	Infrared Spectroscopy
IRAS	Infrared Absorption Spectroscopy
IRE	Internal Reflection Element
LV	Linear Voltammetry
MS	Mass Spectroscopy
NPh	Nitrophenol
SEIRA	Surface Enhanced Infrared Absorption Spectroscopy
SEM	Scanning Electron Microscopy
SNIFTIRS	Subtractively Normalized Interfacial FTIR
TOC	Total Organic Carbon
W	Watt
XPS	X-ray Photoelectron Spectroscopy
XRD	X-ray Diffraction
ΔR	Reflectance

Chapter 1

Introduction

1.1 Fourier Transform Infrared Spectroscopy

Infrared (IR) spectroscopy stands as a very powerful analytical tool in many facets of chemical research. All molecules with 'n' atoms contain 3n degrees of freedom, six of which are vibrational modes (3 rotational and 3 translational). This leaves 3n-6 vibrational modes (3n-5 if linear).[1] All of these vibrational modes absorb infrared energy at differing frequencies, depending on the force constant of the bond and the reduced mass of the molecules involved. These modes appear in an IR spectrum if the vibration mode creates a change in the overall dipole of the molecule, this is the IR selection rule.[2] There exist five normal vibrational modes: rocking, bending, stretching, scissoring, and twisting.

IR spectroscopy is very useful in the identification of molecules. In electrochemistry and photochemistry, there is a need to identify species that exist at a catalyst surface, some of which can be very short lived. The standard IR spectroscopy method is far too time consuming, (scanning through each individual frequency from high to low) to be effective for this purpose. A variation of IR spectroscopy, Fourier Transform IR (FTIR), suits the requirements for use in electrochemical studies. The Fourier transform is a mathematical linear operation which can decompose a signal into its frequency components.[3] For spectroscopy applications this is a very powerful tool. FTIR utilizes what is known as a Michelson interferometer to distinguish itself from other IR methods (seen in Figure 1.1). The interferometer consists of a set of mirrors, one stationary and one moving, to deflect the IR signal.[4] The IR beam leaves the light source and is deflected at a half-silvered mirror to the stationary mirror, as well as the moving mirror, inducing

a time delay in the signal. The beams interfere with one another, with the time delay being recognized for different mirror positions, and the beam is now essentially a single pulse of light with a decaying signal of all frequencies. Upon reaching the detector, the Fourier transform can be applied to break this signal pulse into its frequencies, producing an IR spectrum.

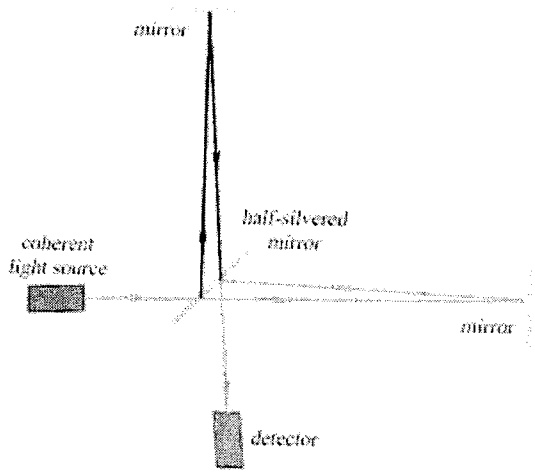

Figure. 1.1[4] The Michelson Interferometer used to induce a time delay to the IR beam, creating FTIR spectroscopy

The main advantage of FTIR spectroscopy is the rapid acquisition. Since the IR beam is made up of single pulses, a very short time is required to produce a single spectrum (~0.6 s). Due to this rapid acquisition, this technique can easily be used to identify short-lived species (<1 s) at a catalyst surface. These species may be difficult to observe in a single spectrum due to inherent noise, however this is rectified by co-adding a series of spectra to improve the signal to noise ratio.

In a reflection study of species occurring at a catalyst surface, there is a second selection rule which needs to be met in order for a signal to appear in the IR spectrum: the surface

selection rule. At a metal surface, the IR beam creates an electric field, of which the portion that is parallel to the surface is screened.[5] What remains is the component of the beam which is perpendicular to the surface, and it carries this information from the metal surface to the detector. Vibrational peaks appear if their dipole change for the vibrational mode occurs perpendicular to the electrode surface.[6,7]

A second effect occurring at the surface of a metal is the enhancement of IR signal, first reported by Osawa. [7,8] IR signals from species adsorbed onto metal surfaces such as gold and platinum achieve an enhancement of their signal due to an electric field at the metal surface, which is produced by excitation of the metal plasmon from the incident infrared radiation.[9,10] This enhancement decreases rapidly as the species move away from the metal surface, but provides a ten-fold improvement over conventional external infrared absorption, as long as the surface electrode has a nanometer-scale roughness.[11, 12]

It is these benefits that make FTIR spectroscopy a powerful tool in the analysis of *in-situ* electrochemical experiments, first pioneered by Bewick in the early 1980's.[13, 14] The primary FTIR technique applied in the study of electrochemical interfaces is external reflection infrared absorption spectroscopy (IRAS). Herein a reflective bulk electrode is pressed against an IR window with low refractive index, thus creating a thin solution layer, only a few microns thick.[15,16] This configuration is advantageous for the study of consumption of reactants and formation of products as well as intermediates. However, the decrease of mass transport, high electric resistance and need for a reflective electrode surface make this set-up non-co-operative for kinetic electrochemical studies.[10,17] There also exists a large interference from water present in the bulk solution, a very undesirable trait.

Prevention of interference from the bulk solution is a necessity in electrochemical FTIR experiments. The use of the attenuated total reflection (ATR) mode of FTIR accomplishes this.[18] A semi-hemispherical semiconductor crystal has the IR beam deflected into it; if the angle of incidence is greater than the critical angle of the material, a standing evanescent wave is created above the surface of the ATR crystal, as seen in Figure 1.2 below.

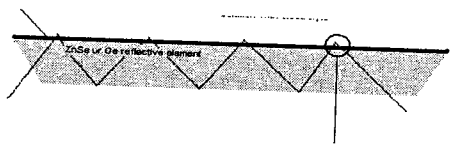

Figure 1.2 The basis of ATR-FTIR spectroscopy, showing the generation of a standing evanescent wave above the ATR-crystal surface.

The evanescent wave of the IR beam can collect information from immediately above the surface of the crystal, limiting the information from the bulk solution. Further correction of the bulk solution is achieved in the spectral analysis. Subtractively normalized interfacial FTIR spectroscopy (SNIFTIRS) can be used to remove background information which is not desired in the penultimate spectrum.[19] For SNIFTIRS, two spectra are collected with a variable changed, e.g. applied potential , with the base spectrum denoted $R_{(E1)}$ and the second chronologically called $R_{(E2)}$. The spectra are subtracted from one another and normalized to the base in the following function:[20]

$$\Delta R/R = (R_{(E2)}-R_{(E1)})/R_{(E1)}$$

The resulting spectrum contains only information from species which are altered between $R_{(E1)}$ and $R_{(E2)}$ and the constant signal from the bulk solution is removed. A positive orientated band corresponds to a larger amount of the species at $R_{(E1)}$ conditions, while a negative-going

band represents an increase in species at the $R_{(E2)}$ conditions. A third type of band can also appear, one having a bipolar feature. This spectral feature is the result of the Stark effect, seen throughout spectroscopy.[21-23] In the presence of an electrical field at the surface of an electrode, the frequency at which specific bands are shifted changes with applied potential to the electrode. With SNIFTIRS, these small shifts in band position create the bipolar bands, as seen in Figure 1.3

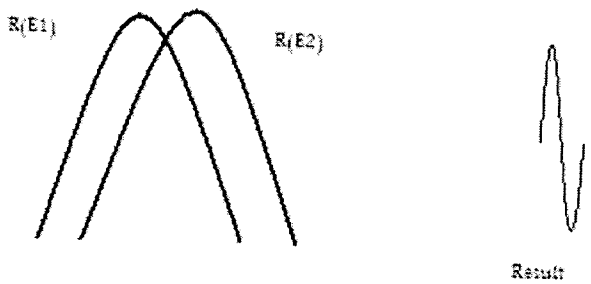

Figure 1.3 Generation of bipolar bands due to the Stark effect in an ATR-FTIR spectrum using the SNIFTIRS technique.

These bipolar bands in a spectrum with $R_{(E1)}$ at a lower applied potential than $R_{(E2)}$ have the negative going lobe at a higher frequency. This trend is observed for all species, with an exception being CO absorbed on a metal surface, in which case abnormal IR is observed.[24] The phenomenon arises from the enhanced electric field at the electrode surface and the strong bonding of the CO molecule to metal surface.[25,26] In Pt nanomaterials, there exists interparticle interactions and electron hole damping which play a large role in creating this abnormal effect.[27]

ATR-FTIR spectroscopy is fast becoming a widely used tool in electrochemical research,[28-36] having been applied to many systems such as electrochemical oxidation, metal

corrosion, and absorption. Potentially this system can be utilized in many areas of the study of nanomaterials including electrocatalysis and photocatalysis.

1.2 Nanomaterials

Nanomaterials, which are made up of at least one dimension under 100nm, are the building blocks in the booming field of nanotechnology. Despite existing on such a miniscule scale, nanomaterials have the potential to forever change our world. Throughout the development of society, mankind strove to build bigger and better, and we have since seen a change in this belief as we now move to refine and develop on a much smaller scale.

The advantage of nanomaterials lies in their physical properties, including a very large surface to volume ratio, strong electrical and heat conductivities, and photoemission.[37] A key chemical property, electrocatalytic activity, is essential to the benefit of using nanomaterials in fuel cell reactions. This role in fuel cells is just one area where nanomaterials are making an impact; they can also be found in bioengineering, molecular electronics, renewable energy, sensors and wastewater purification.[38] In all of these areas, nanomaterials can be applied in as both electrocatalysts and photocatalysts.

Nanomaterials are grouped into four classes: 1) zero dimensional nanoparticles, 2) one dimensional nanotubes and nanorods, 3) two dimensional thin films, and 4) three dimensional nanostructures.[39] They can be fabricated through two methods. The first is chemical synthesis, which is used to economically form a larger quantity of nanomaterials.[37] Along with the economic benefit, chemical synthesis also allows for stoichiometric control over composition and particle size. There is also a negative impact of this route, as the precursor solutions may deposit themselves onto the exterior of the particles, thus contaminating them. Examples of this

technique are the thermal decomposition technique,[40] hydrothermal technique[41] and sol-gel process.[42] The second method is physical synthesis, in which evaporation and condensation of a material can form nanomaterials. This method allows for the nanomaterials to have controlled size with very minimal contamination. Two examples are laser ablation[43] and physical vapour deposition.[44] Nanomaterials are going to play a large part in our future, with prominent positions coming in the development of fuel cells and solar energy.

1.3 Methanol and Formic Acid Oxidation

As the energy demand of our world undergoes a rapid increase, the need for an alternate energy source to fossil fuels is fast becoming a top priority. Fuel cells present a solution with both high efficiency and low levels of harmful emission.[45] The two prominent fuel cell set ups are proton exchange membrane fuel cells (PEMFCs)[46] (hydrogen fuel source) and direct methanol fuel cells (DMFCs).[47] PEMFCs are limited due to their use of hydrogen, which is still without a safe storage method. DMFCs consume methanol that can be safely stored. Also, methanol has a higher energy density than an equivalent amount of hydrogen.[48] While this technology is promising, there are several hurdles that need to be overcome before commercialization of a practical DMFC can occur. A big step can be taken by studying the reactions of methanol and other simple fuels, such as formic acid, at catalyst surfaces.

In the development of nanostructured materials for use in fuel cells, one of the main reactions to be studied is the oxidation of methanol.[45] The prominent catalyst on which the oxidation of methanol is studied is platinum. The mechanisms of methanol oxidation have been researched extensively, with information still needed to be gained. A possible mechanism of methanol oxidation at a Pt electrode is summarized below:[45]

$CH_3OH \rightarrow (CH_3OH)_{ads}$ (Methanol adsorption)

$(CH_3OH)_{ads} \rightarrow (CO)_{ads} + 4H^+ + 4e^-$ (C-H bond activation)

$H_2O \rightarrow (H_2O)_{ads}$ (Water adsorption)

$(H_2O)_{ads} \rightarrow (OH)_{ads} + H^+ + e^-$ (Water activation)

$(CO)_{ads} + (OH)_{ads} \rightarrow CO_2 + H^+ + e^-$ (CO oxidation).

All adsorption occurs at Pt sites. A drawback of this process is the slow kinetics due to the methanol adsorption and CO oxidation steps. Three adjacent Pt sites are required for initial adsorption of the methanol, two of which become vacant as the methanol is oxidized to CO.[49] This generated CO poisons at the Pt catalyst through a strong bond. Since only two sites are vacated during the oxidation process, it is difficult for a new methanol molecule to be adsorbed, until the third is freed from the adsorbed CO through oxidation. New experimental techniques are required to fully understand and improve upon this process.

The final product of the oxidation of methanol is CO_2, with significant amounts of CO, formic acid, methyl formate and formaldehyde also formed along the pathway.[50] It has been suggested that multiple reaction mechanisms exist. In the production of CO on a pure Pt electrode, a strongly poisoning species is created. For it to be oxidized, an activated water species must be employed to oxidize this molecule, requiring a high level of energy, thus creating an undesirable trait for an efficient fuel cell catalyst. This is overcome through addition of co-catalysts to improve the performance of the Pt by an electronic effect and weakening the strength of the Pt-CO bond, or a bifunctional effect through which the co-catalyst assists in the oxidation of Pt-CO.[51]

Also an intermediate in the methanol oxidation process, formic acid is studied as a prototype for the oxidation of methanol to gain more information on the molecular level of the methanol oxidation reaction. It is accepted that formic acid becomes oxidized to CO_2 through a dual pathway mechanism:[52-53] a direct path via an adsorbed intermediate, called a dehydrogenation pathway, and an indirect path creating a poisoning CO species called the dehydration pathway. A carboxylic acid, COOH, has been suggested as the reactive intermediate in the direct path.[54] A second candidate for this intermediate is formate, $HCOO^-$. Both have been observed adsorbing to Pt and Pd surfaces.[55-57] By understanding the oxidation of this simple molecule, it becomes easier to understand the reaction process of the oxidation of methanol. The oxidation of methanol and formic acid are used to study the performance of nanomaterials in simple fuel cell processes before moving to a more advanced system. Nanomaterials can also be used to degrade harmful compounds in an environmentally friendly process, photocatalysis.

1.4 Photocatalysis

Harnessing our greatest energy source, the sun, is a driving force in chemical research. Much work has been done in the development of new technologies to harness the solar energy for applications in batteries, self-cleaning and wastewater treatment.[58-60] One of the common compounds used in this research is TiO_2 due to its low cost, high efficiency and recyclability. For a photocatalyst to become photochemically active, an energy zone must be overcome by an electron. When the photocatalyst absorbs a light energy which is higher than the energy gap, this energy can be used to promote the electron present in the valence band to the conduction band, leaving behind a photogenerated hole with a positive charge. The energy required to overcome this band jump is referred to as the band gap energy. TiO_2 has a band gap of 3.2eV,[61] where UV light can provide sufficient energy to promote electrons to the conduction band. With the

addition of dopants, e.g. Ni, S, N,V, Fe, B or F[62-66] to the TiO_2 structure, this band gap can be reduced to a level where light in the visible spectrum can be utilized to activate the photocatalyst, making it a very environmentally friendly and efficient photocatalyst.

While TiO_2 and the other photocatalysts have many potential applications, a major facet is their use in the degradation of organic pollutants.[67] With light serving as the driving force behind the process, photocatalytic degradation of organic pollutants is a very green technique. The process through which this degradation occurs is still open to debate with two potential pathways proposed. The first is a surface reaction where the organic pollutant can accept the conduction band electron to be reduced, or be oxidized directly from the photogenerated hole. The second process involves the formation of hydroxyl radicals from the activation of water at the catalyst surface. The photogenerated hole will oxidize a water molecule to a hydroxyl radical, which in turn can attack the organic pollutant molecules leading to their subsequent degradation.[68-71] Knowledge of the exact mechanism through which the pollutants are degraded is essential to the further improvement of this technique, as different types of photocatalyst are more successful in the degradation of various compounds.

As can be seen, the photogenerated hole plays a key role in both pathways; however, its existence can be short lived. Upon promotion of an electron to the conduction band, there now exists a charge separation between the negative electron and positive photogenerated hole. Recombination of the two is expected and occurs rapidly, thus hindering the performance of the catalyst. To prevent this, the catalyst can be immobilized on a dimensionally stable anode, through which an external potential bias can be applied.[72-73] This added energy provides the additional stability needed to have the electron remain in the conduction band and overcome the

charge separation between itself and the photogenerated hole. The electron can then be used to reduce a molecule or picked up by an electron scavenger (eg. O_2)

Previous work has been done using ATR-FTIR to study degradation of organics using TiO_2 photocatalyst,[60, 74-76] the majority dealing with a flow cell set up, where the reaction solution is monitored using ATR-FTIR, yet information is not gained from the catalyst surface. Many compounds have been tested using this technique, with different reaction schemes selected. The potential for *in-situ* photochemical FTIR from the catalyst surface is great as it will lead to further identification of reaction products and intermediates.

1.5 Rationale and Scope of the Thesis.

An overview of the fundamentals of infrared spectroscopy, mainly the Fourier Transform method was presented in this chapter. Reasons for its use and benefits of the system were presented relating to its use in the study of nanostructured systems. Two main techniques which heavily influence this thesis are the surface enhanced infrared absorption (SEIRA) and abnormal infrared effects (AIRE). Also, an introduction into nanomaterials, their synthetic roots and potential applications were given, all stemming from the unique chemical, physical and electronic properties which the nanomaterials possess. Two of the main systems in the study of fuel cell development using Pt-based nanomaterials, methanol and formic acid, were discussed, focusing mainly their oxidation mechanisms, which still require research into their understanding. These systems will be utilized throughout this thesis work. Photocatalysis was discussed as well, as this is a novel area of research using ATR-FTIR spectroscopy. The objective of my thesis is to develop a new ATR-FTIR technique in our laboratory for *in-situ*

monitoring of both surface and solution species as well as its role in the study of electrocatalysis of novel Pt-based nanomaterials and photocatalytic degradation of organic pollutants.

The following chapter, Experimental Methods, will give information regarding the fabrication of nanostructured materials with the hydrothermal and thermal decomposition techniques and the corresponding surface analysis and characterization. Electrochemical and photochemical testing and ATR-FTIR experiments will be described as well. Chapter 3 will present the development and performance of the ATR-FTIR technique. Chapters 4-7 will present experimental data collected using ATR-FTIR in the study of several systems; Chapter 4 : PtRuIr for methanol oxidation; Chapter 5: the oxidation of glucose using Pt, PtRu, PtIr, PtPb; Chapter 6: PtPb (formic acid) and PtPd (methanol) nanodendrites; Chapter 7: electrochemical and photochemical degradation of pollutants. Chapter 8 will provide a summary of the results and conclusions.

1.6 References

1. Atkins, P.; de Paula, J. *Physical Chemistry*, 7th Edition, **2003**, W.H. Freeman and Company, New York, NY. 520
2. Atkins, P.; de Paula, J. *Physical Chemistry*, 7th Edition, **2003**, W.H. Freeman and Company, New York, NY. 513
3. Sneddon, I. N. *Fourier Transforms.* New York: Dover, **1995**
4. Gray, Dwight E. ed. *American Institute of Physics Handbook 3rd Ed.* McGraw-Hill: New York. **1982**
5. Greenler, R.G. *J. Chem. Phys.*, **1966**, 44, 310
6. Osawa, M.; Ataka, K.I.; Ypshii, K.; Nishikawa, Y. *App. Spectro.*, **1993**, 47, 1497
7. Osawa, M.; Yoshii, K.; Ataka, K.I.; Yotsuyanagi, T. *Langmuir*, **1994**, 10, 641
8. Noda, H.; Ataka, K.; Wan, L.J; Osawa, M. *Surf. Sci.* **1999**, 427/428, 190
9. Osawa, M.*Top. App. Phys.* **2001**, 81, 163

10. Osawa, M. *Bull. Chem. Soc. Jpn.* **1997**, 70, 2861

11. Miyake, H.; Ye, S.; Osawa, M. *Electrochem. Commun.* **2002**, 4, 973

12. Osawa, M.; Ataka, K. *Surf. Sci. Let.*, **1992**, 262, L118

13. Bewick, A.; Kunimatsu, K. *Surf. Sci.* **1980**, 101, 131

14. Bewick, A.; Kunimatsu, K.; Pons, B.S. *Electrochim. Acta.* **1980**, 25, 465

15. Iwasita, T.; Nart, F.C. *in*: Gerischer, H.; Tobias, C.W. *Advances in Electrochemical Science and Engineering*, Vol 4, VCH, Weinheim, **1995**, CH. 3

16. Korzeniewski, C. *Crit. Rev. Anal. Chem.* **1997**, 27, 81

17. Wandlowski, T.; Ataka, K.; Pronkin, S.; Diesing, D. *Electrochim. Acta.* **2004**, 49, 1233

18. Perkin-Elmer *Technical Report* "FT-IR Spectroscopy: Attenuated Total Reflection" Shelton, CT. **2005**

19. Pons, B.S.; Davidson, T.; Bewick, A. *J. Electroanal. Chem.* **1984**, 169, 63

20. Li, H.Q.; Chen, A.; Roscoe, S.G.; Lipkowski, J. *J. Electroanal. Chem.* **2001**, 500, 299

21. Zou, S.; Gomez, R.; Weaver, M.J. *J. Electroanal. Chem.* **1999**, 474, 155

22. Lambert, D.K. *Electrochim. Acta.* **1996,** 41, 623

23. Ikezawa, Y.; Sawatari, T.; Kitazame T.; Goto, H.; Toriba, K. *Electrochim. Acta.* **1998,** 43, 3297

24. Lu, G.Q.; Sun, S.G.; Cai, L.R.; Chen, S.P.; Tian, Z.W.; Shui, K.K. *Langmuir* **2000**, 16, 778

25. Sun, S.G.; Cai, L.R.; Chen, S.P.; Tian, Z.W.; Shiu, K.K. *Langmuir*, **2000**, 16, 778

26. Lu, G.Q.; Sun, S.G.; Chen, S.P.; Cai, L.R. *J. Electroanal. Chem*, **1997,** 421, 19

27. Wu, C.X.; Lin, H. *J. Chem. Phys.* **2004**, 121, 1553

28. Berna, A.; Rodes, A.; Feliu, J.M. *J. Electroanal. Chem.* **2004**, 563, 49

29. Chen, X.Y.; Miki, A.; Ye, S.; Sakai, H.; Osawa, M. *J. Am. Chem. Soc.* **2003**, 125, 3680

30. Ataka, K.; Yotsuyanagi , T.; Osawa, M. *J. Phys. Chem.* **1996,** 100, 10664

31. Huo, S.J.; Xue, X.K.; Li, Q.X.; Xu, S.F.; Cai, W.B. *J. Phys. Chem. B.* **2006**, 110, 25721

32. Wang, M.L.; Zhang, Y.Y.; Xie, Q.J.; Yao, S.Z. *Electrochim. Acta.* **2005**, 51, 1059

33. Mondelli, C.; Ferri, D. Grunwalkdt, J.D.; Krumerich, F.; Mengold, S.; Psaro, R.; Baiker, A. *J. Catal.*, **2007**, 252, 77

34. Ohman, M.; Persson, D. *Electrochim. Acta.* **2007**, 52, 5159

35. Librini, M.; Fontaine, G.; Gengembre, L.; Traisnel, M.; Leralsle, O.; Genet, N. *Corr. Sci.* **2009**, 51, 1201

36. Bae, S.E.; Yoon, J.H.; Lee, C.W.J. *J. Phys. Chem. C.* **2008**, 112, 1533

37. Pandey, P.; Datta, M.; Malhotra, B. D. *Anal. Lett.* **2008**, 41, 159

38. Masala, O.; Seshadri, R. *Annu. Rev. Mater. Res.* **2004,** 34, 41

39. Siegel, R.W. Nanophase Materials, *Encyclopedia of Applied Physics*, VCH Publishers **1994**, 11, 173

40. Chen, F.C.; Jiang, C.C.; Liu, J.F.; He, D.L.; Zhang, X.H.; Wen, J.X.; Wang, Y.L. *Appl. Surf. Sci.* **2007**, 253, 5155

41. Li, X.L.; Chen, X.J.; Chen, X.Y.; Han, C.L.; Shi, C.W. *J. Cryst. Gro.* **2007**, 309, 43

42. Li, Z.J.; Hou, B.; Xu, Y.; Wu, D.; Sun, Y.H.; Hu, W.; Deng, F. *J. Sol. St. Chem.* **2005**, 178, 1395

43. Gonzalez, J.J.; Liu, C.Y.; Wen, S.B.; Mao, X.L.; Russo, R.E. *Talanta* **2007**, 73, 567

44. Zhou, M.; Feng, C.H.; Wu, C.X.; Ma, W.W.; Cai, L. *J. Nanosci. Nanotech.* **2009,** 9, 4211

45. Liu, H.; Song, C.; Zhang, L.; Zhang, J.; Wang, H.; Wilkinson, D.P. *J. Pow. Sour.* **2006**, 155, 95.

46. Wang, H.; Turner, J.A.; Li, X.; Bhattacharya, R. *J. Pow. Sour.* **2007**, 171, 567

47. Lai, C.M.; Lin, J.C.; Hsueh, K.L.; Hwang, C.P.; Tsay, K.C.; Tsai, L.D.; Peng, Y.M. *J. Electrochem. Soc.*, **2008,** 155, B843

48. Kamarudin S.K.; Daud, W.R.W.; Ho, S.L.; Hasran, U.A. *J. Pow. Sour.* **2007**, 163, 743.

49. Wasmus, S.; Kuver, A. *Journal of Electroanal. Chem.* **1999,** 461, 14.

50. Jingyu, S.; Jianshu, H.; Yanxia, C.; Xiaogang, Z. *Int. J. Electrochem. Sci.* **2007**, 2, 64.

51. Antolini, E.; Salgado, J.R.C.; Gonzalez, E.R.C. *Applied Catalysis B: Environmental* **2006**, 63, 137

52. Parsons, R.; VanderNoot, T. *J. Electroanal. Chem.* **1988**, 257, 9

53. Markovic, N.M.; Ross, P.N. *Surf. Sci. Rep.* **2002**, 45, 11

54. Sun, S.G.; Claviler, J.; Bewick, A. *J. Electroanal. Chem.* **1988**, 240, 147

55. Samjeske, G.; Osawa, M. *Agnew. Chem. Int. Ed.* **2005**, 44, 5694

56. Samjeske, G.; Miki, A.; Ye, S.; Osawa, M. *J. Phys. Chem. B.* **2006**, 110, 16559

57. Chen, Y.X.; Heinen, M.; Jusys, Z.; Behm, R.J. *Angew. Chem. Int. Ed.* **2005**, 45, 981

58. Fujishima, A.; Honda, K. *Nature*, **1972**, 238, 37

59. Asahi, R.; Morikawa, T.; Ohwaki, T.; Aoki, K. Taga, Y. *Science* **2001**, 293, 269
60. Nadtochenko, V.A.; Rincon, A.G.; Stanca, S.E.; Kiwi, J. *J. Photochem. Photobio. A: Chem.* **2005**, 169, 131
61. Hariharan C. *Appl. Catal. A.* **2006**, 304, 55
62. Kostecki, R.; Richardson, T.; McLaron, D. *J. Electrochem. Soc.* **1998**, 145, 2380
63. Nishijima, K.; Ohtani, B.; Yan, X.L.; Kamai, T.; Chiyoya, T.; Tsubota, T.; Murakami, N.; Ohno, T. *Chem. Phys.* **2007**, 339, 64
64. Martin,S.; Morrison, C.; Hoffmann, M. *J. Phys. Chem.* **1994**, 98, 13695
65. Damm, C. *J. Photochem. Photobio* **2007,** 181, 297
66. Reyes-Garcia, E.A.; Sun, Y.P.; Raftery, D. *J. Phys.Chem.C.* **2007**, 111, 17146
67. Wang, R.; Hashimoto, K.; Chikumi, M.; Kojima, E.; Kitamura, A.; Shimohigashi, M.; Watanabe, TY. *Nature*, **1997,** 388, 431
68. Chen, A.; Peng, X.; Holt-Hindle, P. In *Frontal Nanotechnology Research*; M. V. Berg, M.V., Ed.; Nova Science Publishers, Inc., **2007**; pp 131-159
69. Ryu, J.; Choi, W. *Environ. Sci. Technol.* **2006**, *40*, 7034
70. Amano F.; Suzuki S.; Yamamoto T.; Tanaka T.. *Appl. Catal. B. Environ.* **2006**, *64*, 282.
71. Yoon, S.H.; Lee, J.H. *Environ. Sci. Technol.* **2005**, *39*, 9695
72. Agrios, A.; Pichat, P.. *J. Appl. Electrochem.* **2005**, *35*, 655
73. Wu, G.; Nishikawa, T.; Ohtani, B.; Chen, A.. *Chem. Mater.* **2007**, *19*, 4530
74. Nakamura, R.; Imanshi, A.; Murakoshi, K.; Nakato Y. *J.Am.Chem. Soc.* **2002**, 125, 7443
75. Huang, M.; Xu, C.; Wu, Z.; Huang, Y.; Lin, J.; Wu, J. *Dyes. Pig.* **2008**, 77, 327
76. Weisz, A.D.; Regazzoni, A.E.; Blesa, M.A. *Sol. St. Ion.* **2001,** 143, 125
77. Hug, S.J.; Bahnemann, D. *J. Elec. Spec. Rel. Phen.* **2006**, 150, 208

Chapter 2

Experimental Methods

2.1 Materials

The substrates, Ti plates (99.2%), were purchased from Alfa Aesar and were cut into 1.25x0.8 cm with 0.5 cm thickness. H_2PtCl_6- $6H_2O$, $RuCl_3$, $IrCl_3$, $PdCl_2$, $Pb(NO_3)$, , D-glucose, methanol (99.9%), ethanol (90%), formic acid (99%), formaldehyde (37%), ammonium formate, hydrofluoric acid (34%), sulphuric acid (99.999%), sodium hydroxide, 4-nitrophenol, 2-nitrophenol, $TaCl_5$, $Ti(OBu_4)$, potassium phosphate monobasic, isopropanol, butanol, potassium chlorate, and perchloric acid were used as received from Aldrich. P-25 Aeroxide was received from Degussa. The ZnSe ATR crystal was used as received from Spectral Optics.

2.2 Electrode Fabrication

2.2.1 Nanoporous Pt Networks –Electrochemical Testing

The hydrothermal technique was chosen for the fabrication of both Pt- and Pd-based nanomaterials. Titanium plates were etched in 18% HCl for 20 min at 85°C, after which they were rinsed in Nanopure ® ($18 m\Omega / cm^2$) water and transferred to a Teflon® vessel. To the vessel, pre-determined amounts of 0.05M H_2PtCl_6-$6H_2O$, 17% formaldehyde, and Nanopure® were added. The vessel was sealed in an autoclave and heated at 180°C for 10 hr. Upon completion and cooling, the substrates were removed and washed again with Nanopure® water.

Other Pt- and Pd based networks were fabricated in a similar fashion with the following compositions in the hydrothermal vessel:

Sample	Solution (all 0.05M)	Reducing Agent	Duration
PtIr	H_2PtCl_6-$6H_2O$, $IrCl_3$	17% formaldehyde, + 1% HCl	10 hr
PtRu	H_2PtCl_6-$6H_2O$, $RuCl_3$	17%Formaldehyde	10 hr
PtRuIr	H_2PtCl_6-$6H_2O$, $IrCl_3$, $RuCl_3$	17%formaldehyde, + 1% HCl	10 hr
PtPb - porous	H_2PtCl_6-$6H_2O$, $Pb(NO_3)$	17%formaldehyde	10 hr
PtPb- dendrites	H_2PtCl_6-$6H_2O$, $Pb(NO_3)$	99% Formic Acid	10 hr
PtPd	H_2PtCl_6-$6H_2O$, $PdCl_2$ +1%HCl	99% Formic acid	10 hr
PtPd Dendrites	H_2PtCl_6-$6H_2O$, $PdCl_2$+1%HCl	Ammonium formate	10 hr
Pd	$PdCl_2$ + 1%HCl	Ammonium formate	2 hr

Table 2.1 Conditions for the fabrication of nanomaterials using the hydrothermal technique

2.2.2 Nanoporous and Nanodendrites Synthesis –Surface FTIR Studies

To fabricate the nanoparticles for testing using the internal configuration of the ATR-FTIR system, the hydrothermal technique was again used. The precursor metal solutions and reducing agent were placed into a Teflon® vessel along with Nanopure® water, sealed and placed into an autoclave and heated for a certain period of time. (see section 2.2.1 for

compositions and heating times) Upon cooling the particles were transferred, in reaction solution, into a centrifuge tube. The synthesized particles were centrifuged at 12000 R.P.M for 10 min to separate them from the solution. The particles are then ultrasonicated in Nanopure® water for 20 min, centrifuged again, decanted, then placed into clean Nanopure® water. The resulting suspension had a concentration of 50 g/L.

2.2.3 Nanoporous and Nanodendrite Synthesis- Solution FTIR Studies

For study of solution species using ATR-FTIR, the nanomaterials were immobilized onto a bulk electrode. A cylindrical Ti substrate with 1.5 cm diameter and flat face was sanded to obtain a clean surface. The substrate was then coated with Teflon® tape to expose only the clean face and prevent deterioration of the substrate. The substrate was etched in 18% HCl for 20 min at 85°C then transferred to a Teflon vessel along with metal precursors and a reducing agent. This was sealed in an autoclave and heated at 180°C for 10 hr. Upon cooling, the Teflon® coating was removed from the substrate.

2.3. Surface Analysis

The morphology of the nanostructures was characterized with scanning electron microscopy (SEM)(JOEL JSM 5900LV) and the composition with energy dispersive X-ray spectroscopy (EDS)(Oxford Links ISIS). From EDS analysis, an average of values from five different spots on the structure was used to determine the elemental composition. X-ray diffraction (XRD) was performed using a Phillips PW 1050-3710 Diffractometer with Cu Kα radiation. XRD patterns were compared and identified according to the database of the International Centre for Diffraction Data (ICDD). X-ray photoelectron spectroscopy (XPS) (Omicron EA-125 energy analyzer and a multi-channel detector), using a monochromatic Mg Kα

X-ray source (hν =1253.6 eV), was used to determine the metallic and oxide components of each metal.

2.4 Electrochemical Experiments

Cyclic voltammetry, linear sweep voltammetry, and chronoamperometry were all performed in a standard three-electrode cell system. Two reference electrodes, saturated calomel and Ag/AgCl, were employed with a Pt-coil as a counter electrode. The counter electrode was flame annealed prior to each electrochemical experiment. The cell was purged with ultra high purity Ar (99.999%) prior to testing and the cell was held constantly under an Ar atmosphere. These electrochemical tests were performed using a Voltalab 40 potentiostat PGZ301.

For the CO stripping experiments, the potential was held constant at -100 mV for 740s and CO purged into the solution for 600 s, followed by Ar for 120 s, then a 20s rest period prior to the cyclic voltammetric experiments.

2.5 ATR-FTIR Experiments

2.5.1 ATR-FTIR Surface Analysis

These experiments were performed using a Thermo Nicolet 6700 FTIR system with a liquid N_2 cooled MCT-B detector. The nanostructured thin film electrode on the ATR crystal was placed into a Teflon cell designed for this system. Potential control was provided using a HEKA PG 310 potentiostat with an in-house designed computer program controlling both the IR and electrochemical software simultaneously. A single beam background spectrum was collected prior to each experiment with the absence of analyte solution and under Ar atmosphere. The cell was kept under an Ar atmosphere for the duration of the experiments.

2.5.2 ATR-FTIR Solution Analysis

Solution analysis was performed using a Thermo Nicolet 8700 FTIR system with a MCT-A liquid N_2 cooled detector. Potential control was provided through a PARSTAT potentiostat and the in-house computer program. The Ti substrates were placed into a Ti rod to allow connection to the electrochemical system. A Teflon cell containing the bare ATR crystal and three electrodes was used for all experiments. Prior to each data collection the bulk electrode was lowered to the ATR crystal surface, trapping a thin layer of solution.

2.6 Photoelectrochemical Experiments.

2.6.1 Electrode Fabrication

The TiO_2/Ti/Ta_2O_5-IrO_2 bifunctional electrodes were prepared using the thermal decomposition technique. Pure titanium plates of 1.0x12.5x8 mm were first degreased by ultrsonication in acetone for 10 min, then washed with pure water, etched in 18% HCl at 85 °C for 15 min, then completely washed with pure water and finally dried in a vacuum oven at 40 °C. The TiO_2 precursor solution was prepared by adding 1.56 ml of $Ti(OBu)_4$ to 13.41 ml of butanol. The Ta_2O_5-IrO_2 precursor solution was made by mixing the iridium precursor solution (dissolving 0.30 g of $IrCl_3 \cdot 3H_2O$ in 2.5 ml of ethanol) and the tantalum precursor solution (0.13 g $TaCl_5$ dissolved in 7.5 ml of isopropanol).

The TiO_2 precursor was painted onto one side of the etched Ti substrates; the Ta_2O_5-IrO_2 precursor solution was painted onto the opposite face of the Ti substrates, and the solvent was evaporated in an air stream at 80 °C. The electrode samples were calcinated at 450°C for 10 min between each coat. This process was repeated to place six coats onto the one side of the Ti substrates, followed by a final calcination at 450 °C for 1 h. The prepared electrodes were

characterized by scanning electron microscopy (SEM) (JEOL JSM 5900LV) equipped with an energy dispersive x-ray spectrometer (EDS) (Oxford Links ISIS).

2.6.2 Activity Studies.

Electrochemical and photoelectrochemical experiments were carried out in a three electrode cell system controlled by a Voltalab 40 potentiostat (PGZ 301, Radiometer analytical). A Pt coil was used as the counter electrode and flame annealed before the experiments. A saturated Ag/AgCl electrode was employed as the reference electrode. The UV source was CureSpot 50 (ADAC systems) equipped with an Hg lamp. The wavelength range was from 280 nm to 450 nm, and the measured light irradiance was around 2.0 mW/cm^2. The light from the source was guided through a fibre and projected on the surface of the TiO_2 photocatalyst. A 0.5 M NaOH solution served as the supporting electrolyte. The initial concentration of 4-NPh and 2-NPh was 0.15 mM. *In-situ* UV-Vis spectroscopy (Stellar-Net EPP 2000) was used to monitor the concentration of 4-NPh and 2-NPh during the photochemical and photoelectrochemical degradation. The nitrophenolic solutions were constantly stirred in the course of the remediation of 4-NPh and 2-NPh. All the activity tests were performed at room temperature (20 ± 2 °C).

2.6.3 Photochemical ATR-FTIR

A TiO_2 suspension in Nanopure® water was prepared with a concentration of 5g/L. The TiO_2 used was Aeroxide P-25. The solution was placed onto the ZnSe window and dried at 50°C for 3 hr. Upon drying, the new thin layer photocatalyst was rinsed with Nanopure® water. Upon assembly of the ATR-FTIR cell, Ar was purged through the cell while a single beam background was collected. Next the reaction solution was added and allowed to come to equilibrium with the TiO_2 surface for 30 min, the $R_{(El)}$ collected without any UV irradiating the

surface. Following this, the catalyst was irradiated with UV light, and the $R_{(E2)}$ collected every 10 min. The cell was held under constant Ar atmosphere for the duration of the experiment.

2.7 Summary

This chapter presented the experiment details pertaining to the experimental data collected for this thesis work. The preparation of nanomaterials using the hydrothermal technique and their characterization was discussed. Electrochemical experiments, including CO stripping experiments, were described as well as analysis using ATR-FTIR. The fabrication of electrodes for photocatalytic degradation and related experiments along with relevant FTIR experiments was presented. The following chapter will present the development of the two ATR-FTIR systems and their initial use in the study of Pt-based nanomaterials.

Chapter 3

ATR-FTIR System Development

3.1 Introduction

Four main areas need to be studied to garner a full understanding of an electrochemical system:

1. Electrode surface morphology and composition: studied with SEM, EDS, XRD, XPS
2. Electrode electrochemical performance: studied with CV, LSV, CA, CP, EIS
3. Electrolytic solution: studied using HPLC, GC, TOC, MS, ICP
4. Electrode surface reactions: studied with IR spectroscopy, Raman spectroscopy

Infrared spectroscopy is one approach which is commonly used, specifically Fourier Transform Infrared Spectroscopy (FTIR) due to its rapid scan acquisition and high sensitivity.[1] One issue with trying to collect information from the electrode surface is interference from the bulk electrolyte solution, which consists of mostly water. To overcome this problem, Attenuated Total Reflection (ATR)-FTIR is used. Here, an internal reflection element (IRE), usually a ZnSe or Si semi-hemispherical crystal, is added to the system to remove interference from the bulk solution. The IR beam enters the IRE at an angle greater than the critical angle of the medium, $>60^{\circ}$ (for ZnSe), and a standing evanescent wave is produced at the crystal surface.[2] The IR signal collects information from above the crystal surface before returning to the detector.

ATR-FTIR has been used to study many electrochemical systems with the external reflection technique.[3-10] Here the IR beam is deflected off of the electrode surface which is present close to the IRE surface. The need for a reflective electrode surface is a short coming of this technique.[3]

There exist two ATR-FTIR configurations which have been utilized and developed in this thesis. The first is the Kretschmann configuration, where a thin film electrode is placed onto the ATR-crystal window to serve as the working electrode.[3] The thickness of the layer is held under 1μm to ensure the evanescent wave passes through the electrode to read information from its surface, assuming they meet the surface selection rule.[11] In the Otto configuration, a bulk electrode is lowered to the ATR crystal surface, trapping a thin layer of solution. The IR beam can now gather information from this thin layer before reaching the detector. The need for a reflective surface is removed as this configuration is used to monitor species which desorb from the electrode surface. This system has been developed for the purpose of studying the reactions occurring at the surface of nanostructured catalysts. (For the purposes here, the Kretschmann configuration will be referred to as the INTERNAL system, and the Otto configuration called the EXTERNAL system.)

As the move is made into the nanoscale realm, several advantages are gained including an increased surface to volume ratio and enhanced electrocatalytic activity.[12] Pt-based nanomaterials show great promise as potential catalysts in a wide range of applications from fuel cells to chemical sensors.[13] Through these applications, small organic molecules are oxidized by the Pt-nanomaterials. The intermediates and final products of the processes are important pieces of knowledge in the development of catalysts for these purposes. Some of these intermediates are harmful, and the prime culprit is CO, as its bond to Pt is very strong due to back bonding.[14] A high level of energy is required to oxidize this absorbed CO, an undesirable trait for an efficient catalyst. The oxidation of CO, formic acid and methanol are standard test reactions to study Pt-based catalysts.

Through characterization and electrochemical experiments there is much that can be learnt about these bimetallic catalysts. The key area to monitor is the reactions occurring at the surface of these catalysts. This will assist in identifying the role that the co-catalyst is playing in enhancing the performance of the Pt catalyst. The ATR-FTIR systems described in this chapter are capable of monitoring reactions occurring at the surface of a metal. By placing the Pt-based nanomaterials onto the IRE, information can be gathered from the processes occurring at the catalyst surface.

This chapter will first discuss the design and development of the two ATR-FTIR configurations for use in our research laboratory. The problems and their solutions associated with the system development will be discussed. This will be followed by initial studies performed on simple systems involving Pt electrodes. By developing two functional ATR-FTIR systems, we are able to garner a full understanding of the photo- and electrochemical systems studied.

3.2 Design and Development of ATR-FTIR system

3.2.1 Computer Control Software

The ATR-FTIR systems used , Thermo Nicolet 6700(internal) and 8700(external), were controlled by the OMNIC software program. Electrochemical control of the cell was provided by a HEKA PG 310 potentiostat and the POTMaster software program. To help with ease of data collection and accurate collection times, simultaneous control of both machines is required. During my M.Sc project, I developed a computer program written using C^{++} language. This program is launched through a Macro list for the OMNIC program. Upon its launch, the program calls the desired potential from the POTMaster software, and once the potential is set in

the cell, the program begins collection in the OMNIC program. The successful design of this program for the POTMaster/OMNIC was the first step in the development of the ATR-FTIR system. It allows for minimal error to occur between the potential step onset and spectra collection.

3.2.2 ATR system

To successfully develop an ATR-FTIR system, there must be limited interference from outside surroundings. Figure 3.1 shows the ATR-FTIR spectra for the electrochemical cell containing 0.1M $KClO_4$ sitting atop the mirrors. The base spectrum was collected, and 15 min later, the $R_{(E2)}$ was gathered. As can be seen, there exists peaks due to external CO_2 coming from the air around the ATR mirrors, and there is also an excess of noise surrounding 1600cm^{-1} due to the instability of behaviour of the water in the environment. Even with the collection of a single beam background to remove impurities from the system, there are undesirable traits in the spectrum. The ATR-FTIR system was further developed to solve this problem.

A plastic box was built to house the ATR mirrors and allow the electrochemical cell to sit above them. With the box under constant N_2 purge, there were no external sources of CO_2 or water to affect the spectral data. This box was sealed and altered to allow N_2 purging to remove impurities. This trait can be observed in the spectral data presented in the further sections. With the two systems built, the next step was to test electrochemical experiments using the two techniques, starting with the internal system to study surface species.

3.2.3 Kretschmann (Internal) System

To use the Kretschmann (Internal) configuration to study surface species, specific conditions must be decided upon to maximize results. With the window placed in the Teflon

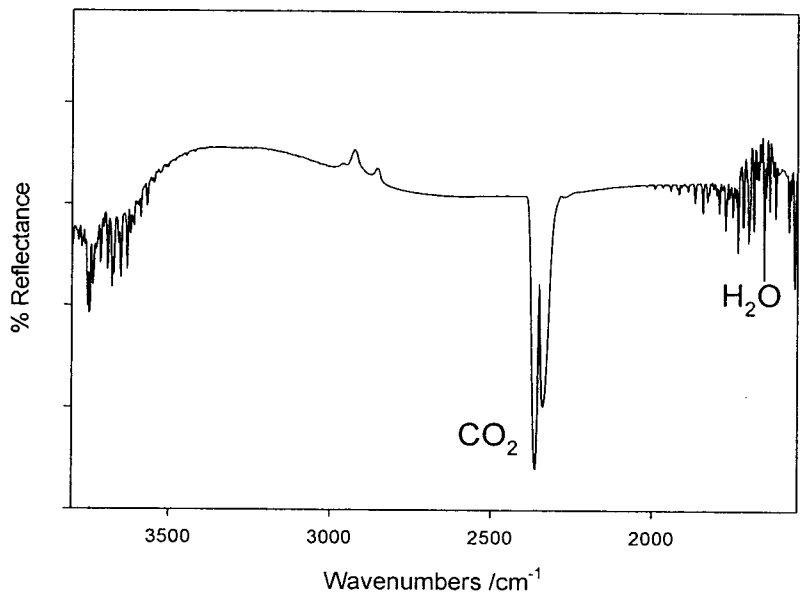

Figure 3.1- ATR-FTIR Spectra of ZnSe window in electrochemical cell perched above ATR mirrors with interference from the environment

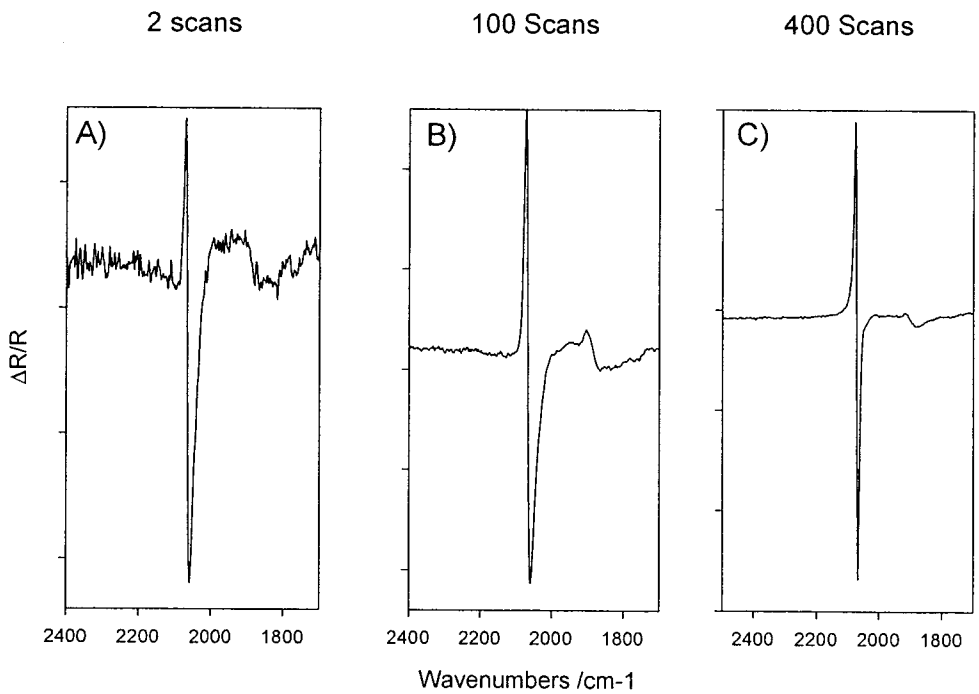

Figure 3.2 Improvement of signal with increasing scans. Pt electrode with 0.5M H_2SO_4 and CO bubbled through solution. $R_{(E1)}$=-200mV, $R_{(E2)}$= 100 mV with A) 2 scans, B) 100 scans, C) 400 scans.

cell, the correct position above the mirrors must be found. With the mirrors set at a constant 60°, adjusting the position of the cell allows the strength of signal to be monitored with the OMNIC software. The ideal condition occurs when the bare window provides a max signal of 14.1 (this signal is in general units). This spot was marked and used for each ATR-FTIR experiment.

The sensitivity of the system was tested next, using a standard experiment, CO adsorption on a Pt electrode. With the internal system, thin film electrodes can be deposited directly onto the IRE surface. For the sensitivity test, a Pt electrode was sputtered onto the ZnSe window. With the cell in place, 0.5M H_2SO_4 was added, followed by an Ar purge. The potential was held at -100 mV for 5 min while the CO purged through the solution, followed by a 1 min rest. The potential was lowered to -200 mV and the first spectrum, $R_{(E1)}$, was collected. The potential was then increased to 100 mV and the second, $R_{(E2)}$, spectrum collected. This produced a bipolar CO band in the final $\Delta R/R$ spectrum where the abnormal behaviour of CO is seen.[15] The number of scans was varied to 2, 100 and 400. These spectra can be seen in Figure 3.2. With a very small amount of scans, a very large bipolar CO peak is still seen in Figure 3.2A. Increasing the number of scans, the signal to noise ratio is improved, as can be seen in Figure 3.2B and 3.2C. 400 scans was selected as the standard number of scans for each ensuing experiment. This simple experiment shows the strong sensitivity of the system, and its ability to detect species at a catalyst surface during an electrochemical experiment can now be effectively studied.

3.2.4 CO oxidation on Pt – Internal Test

The study of CO adsorption on Pt showed our ability to monitor species known to be absorbed onto a thin film electrode. The next step is testing and observing the products of simple oxidation processes occurring at a Pt electrode. By sputtering a thin film Pt layer onto the ZnSe

window, a functional working electrode is produced. First, 0.5M H_2SO_4 was added to the cell to perform electrochemical tests to ensure the cell is suitable for these oxidation reactions. A layer of CO was adsorbed to the electrode's surface in a manner similar to that described in 3.2.3. Cyclic voltammetry was performed from -225 mV to 900 mV to oxidize the adsorbed CO. The corresponding CV curve is displayed in Figure 3.3A, the large band centred at 500 mV is due to the electron transfer during the oxidation of CO, and this band has its onset via a shoulder at 200mV. Following this there is the absence of a CO oxidation band in the second potential scan confirming the complete oxidation of CO.

The oxidation of CO was then monitored using ATR-FTIR to confirm the ability of the technique to identify species present at the catalyst surface. A CO layer was again created and the potential held at -200 mV to collect the base $R_{(E1)}$ spectrum. While increasing the potential in steps to 600 mV in 100 mV increments, the oxidation of CO at this Pt electrode is seen from Figure 3.3B. At first, a large bipolar band at 2060/2020 cm^{-1} appears, this is due to the CO at the Pt surface. The bipolar feature arises due to the Stark effect.[16] At 200 mV this band begins to lose its bipolar feature, corresponding to the onset of the oxidation seen in the CV in Figure 3.3A. At 600mV, the band becomes negative going as the CO is completely oxidized. Using this information, the ATR-FTIR system is able to identify a major species of interest, CO, on a metal surface.

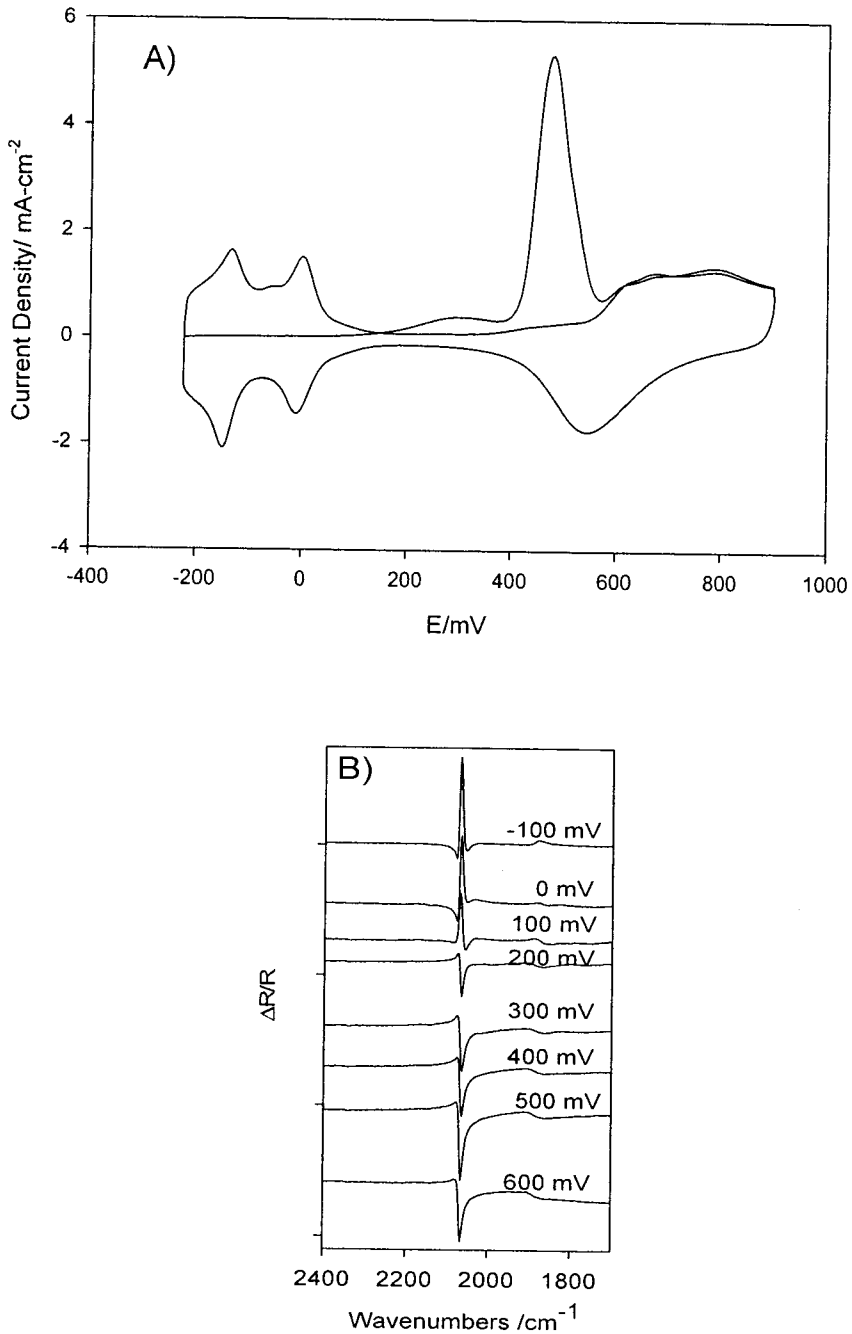

Figure 3.3 A) cyclic voltammogram of CO in 0.5M H_2SO_4 using a sputtered Pt electrode. B) ATR-FTIR spectra monitoring the oxidation of a single layer of CO on the sputtered Pt electrode with $R_{(E1)}$= -200 mV in 0.5M H_2SO_4

3.2.5 Oxidation of Methanol on Pt – External Testing

To confirm the ability of the external system to detect species as they desorb from the catalyst surface, the oxidation of methanol was used as a probe test (CO was not chosen here as the oxidation of methanol provides more information from an analysis of the thin layer). Methanol is a potential source of fuel for electrochemical fuel cells, as it provides safe storage and high energy output.[17] Using a bulk Pt electrode, the initial tests on the Otto (external) configuration were preformed. As the working electrode sat above the window, without a formed thin layer, a CV study was performed in 0.1M CH_3OH + 0.1M H_2SO_4. The CV collected is displayed in Figure 3.4A, and expected results, increasing current density as the methanol is oxidized, beginning at 200 mV, are seen as this matches a typical CV of methanol oxidation using a standard electrochemical cell.[18] Upon lowering the electrode to the ATR-crystal surface, trapping a thin layer of methanol, a standard ATR-FTIR experiment was performed, with $R_{(El)}$ set at -200 mV. The resulting spectra are displayed in Figure 3.4B. A CO_2 band is observed at 2343 cm^{-1} beginning at 200 mV, the onset potential of methanol oxidation, and grows as the potential increases. This is due to the methanol being completely oxidized at the Pt surface. Also, a small band at 1719 cm^{-1} appears at 400 mV, due to a carbonyl (C=O) intermediate (most likely formate[19]) as it desorbs from the catalyst surface. We also see positive going bands at 2956 cm^{-1} and 2841 cm^{-1} corresponding to C-H bands. These appear due to the -CH groups of the methanol being removed in the oxidation process. This data confirms that this technique can be utilized to monitor both intermediates and products of the oxidation processes as they desorb from the catalyst surface.

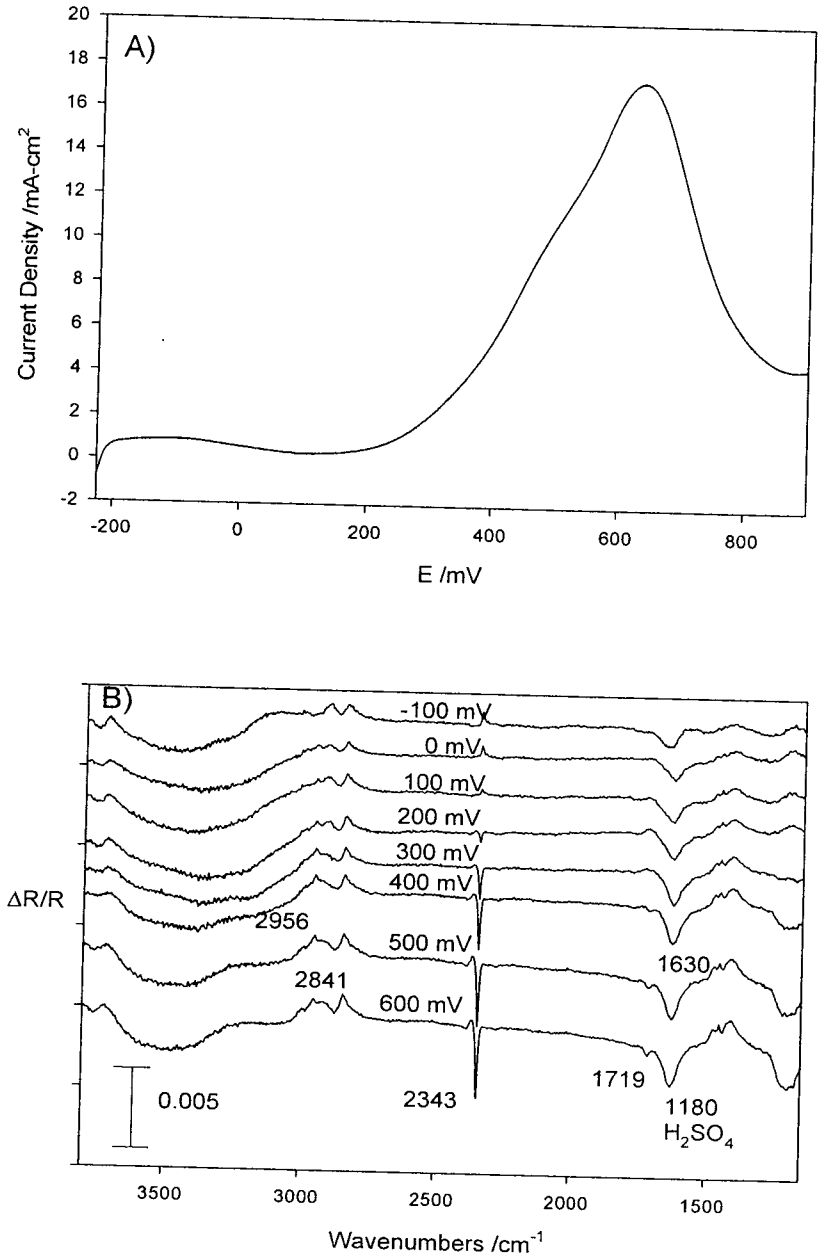

Figure 3.4 Using the external ATR-FTIR system and Pt electrode A) cyclic voltammogram in 0.1M H_2SO_4 + 0.1M CH_3OH at 20 mV/s B) ATR-FTIR spectra of the oxidation of methanol as species become desorbed from the Pt surface.

3.3 ATR-FTIR system for the study of Pt-based Nanomaterials

With the internal system proven to identify surface species throughout the oxidation of CO and the external system used to identify both intermediates and products, the main purpose can be sought for the system. With the testing done on sputtered and bulk Pt, the move must be made to study nanostructured materials using the ATR-FTIR techniques. The internal system will be further tested using nanostructured Pt in two processes, CO and formic acid oxidation.

3.3.1 Characterization of Pt-based Nanomaterials.

The nanostructured Pt catalyst was fabricated using the hydrothermal technique. The corresponding SEM image of the catalyst is displayed in Figure 3.5 and the Pt catalyst displays a nanoporous structure.

3.3.2 Preparation of Nanostructured Thin Films

Upon being placed into their suspension, the Pt was formed into a thin film electrode. A standard coating load must be determined as well as provide full surface coverage to allow conductivity from the contact electrode to the nanostructured catalyst. Figure 3.6 displays the single beam signal strength as a function of the coating load of Pt placed onto the window. Complete coverage is gained at just below 0.0500 g on the window surface. A maximum is seen at ~0.0800 g of the nanomaterials. This is the coating load used in all nanostructured experiments as a decrease in signal strength occurs above this coating load.

3.3.3 CO and Formic Acid Oxidation on Nanoporous Pt

The oxidation of carbon monoxide is an essential test in the performance of potential fuel cell catalysts; as said before, CO can exist as an intermediate or a poisoning species. With the nanoporous Pt thin film electrode deposited onto the ATR window, a CO stripping experiment

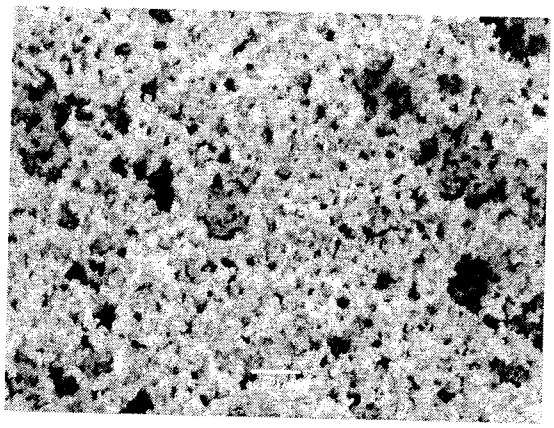

Figure 3.5 Scanning electron micrographs displaying the nanoporous structures of the as-synthesized Pt

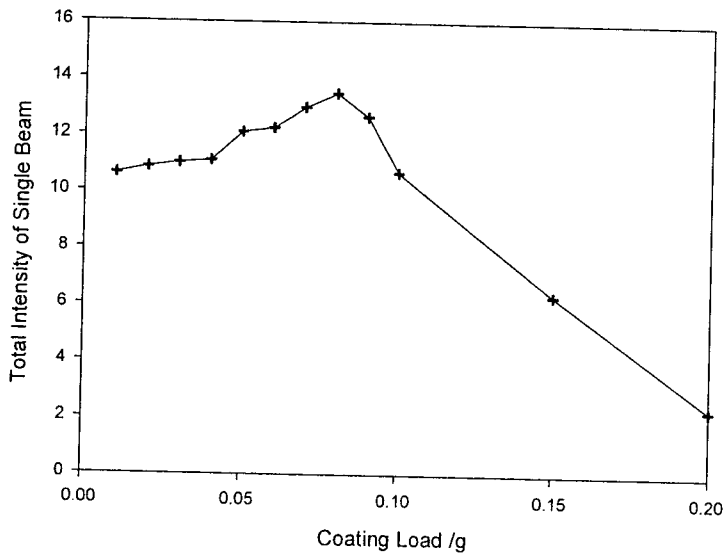

Figure 3.6 Plot of coating load of Pt deposited onto ATR window and the resulting signal intensity measured in the OMNIC software.

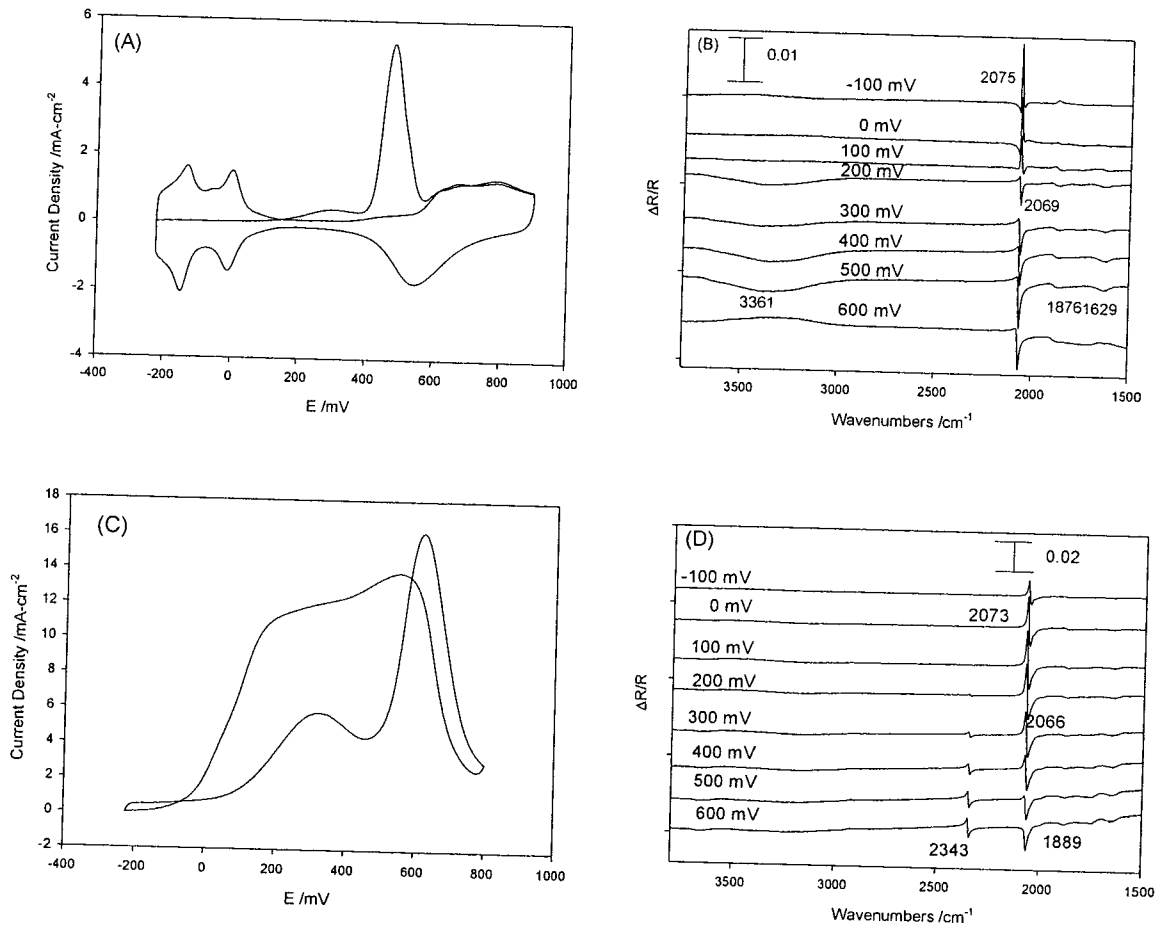

Figure 3.7 A) Oxidation of CO from nanoporous Pt in FTIR cell in 0.1 M H_2SO_4, B) Corresponding ATR-FTIR spectra monitoring the oxidation of CO with $R_{(E1)}$ set at -200 mV, C) oxidation of 0.1 M HCOOH + 0.1 M H_2SO_4 using nanoporous Pt in FTIR cell, D) monitoring the oxidation of HCOOH using ATR-FTIR with $R_{(E1)}$ set at -200 mV

was performed in 0.1 M H_2SO_4. In the CV (Figure 3.7 A), it is seen that the thin film electrode behaves in the same manner as a bulk electrode. A second thin film electrode was prepared with a single layer of CO present at its surface. A base spectrum, $R_{(E1)}$, was collected at -200 mV and subsequent spectra, $R_{(E2)}$, collected in 100 mV increments. The corresponding spectra can be seen in Figure 3.7B.

In Figure 3.7B, a large bipolar band is seen at 2070cm^{-1}/2040 cm^{-1} between -100 mV and 300 mV; this is due to the linearly bonded CO (CO_L). There also exists a band at 1843 cm^{-1} due to bridged CO (CO_B). This CO_L loses its bipolar feature in the 400 mV spectra, due to the oxidation of CO, corresponding to the CV seen in Figure 3.7A. The negative going feature of this band is consistent with the abnormal behaviour of CO at a metal electrode surface.[20]

Moving to a slightly more complex system, formic acid is possibly the simplest organic molecule fuel and also a common intermediate in the oxidation of other simple organic molecules, usually in the final step before CO formation.[21] The oxidation of formic acid on a nanoporous Pt electrode was performed with $R_{(E1)}$ set at -200 mV. A CV of 0.1M formic acid in 0.1M H_2SO_4 is presented in Figure 3.7C. A small shoulder appears at ~100 mV, followed by a large peak centered at 600 mV. The first is due to the formation of carbon monoxide from formic acid, the second is due to the oxidation of the CO at the electrode surface. In the ATR-FTIR spectra seen in Figure 3.7D, a bipolar CO_L band appears at 2070cm^{-1}/2062cm^{-1} growing in intensity with increasing potential until 500 mV. A band at 2343cm^{-1} appears first in the 200 mV spectra due to CO_2 (due to set up of system, CO_2 can return to bulk solution, but is detected when formed in large quantities) . At 1880 cm^{-1} a band appears throughout the spectral series, due to CO_B. Also, a new band, when compared to the oxidation of CO, appears at 1744cm^{-1}. This band can be attributed to a C=O carbonyl group, most likely from an aldehyde species

forming. These spectra remain flat until 600 mV in the νOH region, as Pt requires water to be activated to OH species to oxidize CO.

3.3.4 Explanation of spectral data

From the ATR-FTIR data, an explanation regarding the performance of nanoporous Pt, can be drawn. For Pt, the reactions mechanisms for CO and formic acid are known and reported in the literature.[34] For CO the reaction is:

$Pt + H_2O \rightarrow Pt\text{-}OH_{ad} + H^+$

$Pt\text{-}OH_{ad} + Pt\text{-}CO_{ad} \rightarrow CO_2 + Pt$

And formic acid:

$HCOOH + Pt \rightarrow Pt\text{-}CO_{ad} + H_2O$

$H_2O + Pt \rightarrow Pt\text{-}OH_{ad}$

$Pt\text{-}CO + Pt\text{-}OH \rightarrow CO_2 + H^+$

Our spectral data supports the proposed mechanisms, with a bipolar band, due to CO being present at both potential levels, appearing until 600 mV when the peak loses its bipolar feature as the CO is oxidized to CO_2, where Pt has sufficient energy to oxidize the CO. The reactants and product are both visible in the spectra. For formic acid, an intermediate step is present, in which CO can be formed. We see CO, both linear and bridged, along with a carbonyl band, due to the intermediate step. Finally we observe the final product, CO_2, completing the reaction scheme.

3.4 Summary

In conclusion, two ATR-FTIR configurations were designed, developed and tested using sputtered metal electrodes. Upon the optimizing of experimental conditions, and removing all contamination from the system, simple tests were performed to evaluate the abilities of the system. Using an in-house computer program to control both electrochemical and FTIR aspects of experiments, our system performed well in these tests. CO was detected at a Pt surface, with an increasing signal to noise ratio as the number of scans increased, showing the sensitivity of the system. This standard test proved the existence of a functional internal configuration ATR-FTIR system. The oxidation of methanol was used as the test reaction for the external configuration to monitor solution species. As the potential was stepped up, the appearance of a CO_2 band signified that the system can detect the final product in the oxidation of methanol.

Also in this chapter, the ATR-FTIR system was tested using two simple test oxidation reactions, CO and formic acid. Upon confirmation of ideal conditions including the coating load, nanoporous Pt was used as the test catalyst. From the gathered spectral data, correlation with electrochemical data is seen with the peak potentials and onset potentials for oxidation. Combining these tests, we can conclude that a functional ATR-FTIR has been constructed. The following chapter discusses the application of this system to the study of Pt-based nanostructured materials and their catalyst reactions. Chapter 4 will investigate the development of a trimetallic catalyst for the enhancement of the PtRu catalyst.

3.5 References

1. Yan, Y.G.; Li, Q.X.; Huro, S.J.; Ma, M.; Cai, W.B.; Osawa, M. *J. Phys. Chem. B.* **2005**, 109, 7900
2. Osawa, M. *Bull. Chem. Soc. Jpn.* **1997,** 70, 2861
3. Moon, S.M.; Bock, C.; MacDougall, B. *J. Electroanal. Chem.* **2004**, 568, 225

4. Chbihi, M.E.M.; Takky, D.; Hahn, F.; Huser, H.; Leger, J.M.; Lamy, C. *J. Electroanal. Chem.* **1999**, 463, 63
5. Lapuente, R.; Cases, F.; Garces, P.; Morallon, E.; Vazquez, J.L. *J. Electroanal. Chem.* **1998**, 451, 163
6. Lin, W.F.; Christensen, P.A.; Hamnett, A. *Phys. Chem. Chem. Phys.* **2001**, 3, 3312
7. Lin, W.F.; Christensen, P.A.; *Farad. Disc.* **2002**, 12, 121
8. Kardash, D.; Korzeniewski, C.; Markovic, N. *J. Electroanal. Chem.* **2001**, 500, 518
9. Osawa, M. *Top. Appl. Phys.* **2001**, 81, 163
10. Chalmers, J.M.; Griffiths, P.R., Handbook of Vibrational Spectroscopy, Vol. I, Wiley, Chichester, **2002**
11. Hoffman, F.M. *Surf. Sci. Rep.* **1983**, 3, 107
12. Pandey, P.; Datta, M.; Malhotra, B. D. *Analytical Letters* **2008**, 41, 159
13. Masala, O.; Seshadri, R. *Annu. Rev. Mater. Res.* **2004**, 34, 41.
14. Wasileski, S.A.; Weaver, M.J.; Koper, M.T.M. *J. Electroanal. Chem.* **2001**, 500, 344
15. Gong, H.; Sun, S.G.; Li, J.T.; Chen, Y.J.; Chen, S.P. *Electrochim. Acta* **2003,** 48, 2933
16. Lu, G.Q.; Sun, S.G.; Cai, L.R.; Chen, S.P.; Tian, Z.W.; Shui, K.K. *Langmuir* **2000**, 16, 778
17. Kamarudin S.K.; Daud, W.R.W.; Ho, S.L.; Hasran, U.A. *J. Pow. Sour.* **2007,** 163, 743.
18. Peng, X.S.; Koczkur, K.; Chen, A. *Nanotech.* **2007,** 18, 305605
19. Iwasita, T.; Camara, G.A.; in Sun, S.G.; Christensen, P.A.; Wieckowski, A. In-Situ Spectroscopic Studies of Adsorption at the Electrode and Electrocatalysis, **2007,** Elsevier, Amsterdam, Ch. 2
20. Greenler, R.G. *J. Chem. Phys.*, **1966**, 44, 310
21. Chen, A.; La Russa, D.; Miller, B. *Langmuir*, **2004**, 20, 9695

Chapter 4

Fabrication and ATR-FTIR study of trimetallic PtRuIr for methanol oxidation

4.1 Introduction

In recent years a worldwide increase in energy demands, coupled with increased pollution concerns and depleted fossil fuel reserves, has driven research toward novel means of creating energy with high efficiency and low emissions.[1] Fuel cells are potential solutions to this pressing problem, specifically direct methanol fuel cells (DMFCs) [2-3] holding advantages over such others as proton exchange membrane fuel cells. From a fuel consumption point of view, the DMFC hold preference over the PEMFC. Hydrogen still lacks a safe and reliable storage method, whereas methanol, with a higher energy density, is more easily stored and distributed at ambient temperatures.[1] DMFCs are a very complex system with several hurdles to overcome prior to their commercial availability. While Pt initially provided promise as a potential catalyst to drive these fuel cells, further research must now be done to improve on this source. In the development of a practical catalyst, the high cost and inefficiency of the Pt catalyst will hinder its potential commercialization. As for the inefficiency of a Pt catalyst, CO_2 is the main product of methanol oxidation, however, other species such as CO, formaldehyde, formic acid and methyl formate also arise during the oxidation, creating possible multiple degradation mechanisms.[3] The formation of CO is the most troublesome on Pt anodes, as CO can strongly adsorb to the catalytic sites, hindering the kinetics of methanol oxidation. CO can be removed from the Pt surface at high potentials through the activation of water in creating OH species, which carry out an oxidative step with the CO[1,4]:

$$(CO)_{ads} + (OH)_{ads} \rightarrow CO_2 + H^+ + e^-$$

This oxidation of CO occurring at high potential levels is an undesirable property for a potential DMFC. The Pt catalyst can be improved through advanced structural designs[5] and the addition a co-catalyst. A wide variety of studies have been carried out to rectify this problem using various co-catalysts such as Mo [6-7], Ru[8-12], Sn[13-15] W[16-17], Pb[18-19], Bi[18], and Os[20] coupled with Pt to enhance the performance of the Pt catalyst in the oxidation of many model fuel compounds. This coupling with other catalysts also does service to lower the level of Pt required in the catalyst, making the development more practical from a financial standpoint. An example of the enhancement of the performance in the oxidation of model fuels was shown by our group with a nanostructured $Pt_{62}Ru_{38}$ electrocatalyst.[21] This catalyst showed high performance in the oxidation of both CO and methanol through the production of oxygen species at the Ru sites. PtRu catalysts have become the research standard for comparison due to their strong performance.[22-25] They show strong performance due to the Ru sites assisting in the oxidation of adsorbed CO on Pt sites:

$$Ru\text{-}OH + Pt\text{-}CO \rightarrow CO_2 + H_2O$$

We believe this already powerful catalyst can be further improved through the addition of a third co-catalyst in a trimetallic electrocatalyst. IrO_2 is a powerful catalyst in the generation of oxygen species at the electrode surface[26-27], and we have previously shown the strong performance of PtIr nanomaterials in fuel cell based research. This work will focus on enhancing the already successful PtRu catalyst through the addition of Ir to the catalyst. In doing so, a lower level of Pt will be required, lowering the potential cost, as well as improving upon the activity towards the oxidation of methanol.

Fourier transform infrared spectroscopy (FTIR), due to its rapid scan rate and high sensitivity, is a powerful tool used in the monitoring of reactions at the electrode surface.[28]

Interference from the bulk electrolyte can cause many problems in the acquisition of spectral data, thus attenuated total reflection (ATR)-FTIR is employed to overcome this problem. A thin film electrode is deposited onto an internal reflection element (IRE), commonly made of Si[29-31], Ge[32], ZnSe[33] , and the IR beam is deflected off a mirror into the IRE at an angle greater than the critical angle of the IRE. This creates a standing evanescent wave above the surface of the IRE, passing through the thin film electrode where data can be collected from the electrode surface. Much work has recently been done to study electrode surface reactions in electrochemical cells using FTIR.[34-38] By collecting a spectrum at a base potential, denoted $R(E_1)$, the potential can then be stepped to a second level where a second spectrum is collected, $R(E_2)$[39] :

$$\Delta R/R = \frac{R(E_2) - R(E_1)}{R(E_1)}$$

The preceding formula is then applied to produce the final spectra, showing only changes occurring at the electrode surface.

In this arrangement of the ATR-FTIR cell, species which desorb from the electrode surface are lost to the bulk solution, thus becoming undetectable in the IR spectra. To overcome this problem, a second setup to monitor these desorbed species can be employed. A bulk cylindrical electrode is pressed to the surface of the ZnSe crystal, trapping a thin layer of solution. The IR beam now reads from in the thin layer, detecting any desorbed species, without any information from the electrode surface.

4.2 Surface characterization

The surface morphology of the nanoporous-Pt networks was studied using SEM at 10000 x magnification. Figure 4.1 shows the electrode surfaces of (A) nanoporous Pt, (B) PtRu, (C) PtRuIr, all of which display high surface coverage of the Ti substrate with random distribution of pores throughout the catalyst network. The PtRu and PtRuIr samples show particle sizes ranging from 50-500 nm with pores ranging from tens of nanometers to several micrometers in diameter.

EDS analysis was performed on the samples to determine their composition. From the quantitative study it was found that the composition of the samples are A) Pt_{100} B) $Pt_{60}Ru_{40}$ C) $Pt_{55}Ru_{30}Ir_{15}$, confirming the expected results from the composition of the precursors solutions. (compositions selected based on previous studies)

The presence of electronic interactions between the components was studied with XPS. In Figure 4.2A two 4f binding peaks of Pt, identified as $4f_{7/2}$ and $4f_{5/2}$, are evident for the nanoporous Pt, PtRu and PtRuIr electrodes. The Pt $4f_{7/2}$ and $4f_{5/2}$ doublets of the nanoporous Pt occur at 71.0 and 74.3 eV and at 71.3 and 74.7 eV for the nanoporous PtRuIr electrode. In Figure 4.2B , the Pt $4f_{7/2}$ and $4f_{5/2}$ doublets of the nanoporous PtRu electrode occur at 71.4 and 74.8 eV. The Ir $4f_{7/2}$ and $4f_{5/2}$ doublets for the PtRuIr electrode occurred at 60.6 and 63.6 eV versus the values for Ir metal of 60.9 and 63.9 eV[40-41] . Ru was also analyzed in the stronger Ru 3d region. Figure 4.2C and 4.2D show that the Ru $3d_{5/2}$ and $3d_{3/2}$ binding peaks occur at 280.2 and 284.4 eV for the PtRuIr electrode (2D) and at 280.3 and 284.5 eV for the PtRu electrode(2C), compared to 280.0 and 284.0 eV for Ru metal[42] . The XPS results for the PtRuIr electrode reveal shifts in the Pt 4f region, Ru 3d, and Ir 4f binding energies of 0.3, 0.3 and 0.2 eV, respectively. Similarly, for the PtRu electrode, a shift in the Pt 4f and Ru 3d binding energies of 0.4 and 0.3 eV,

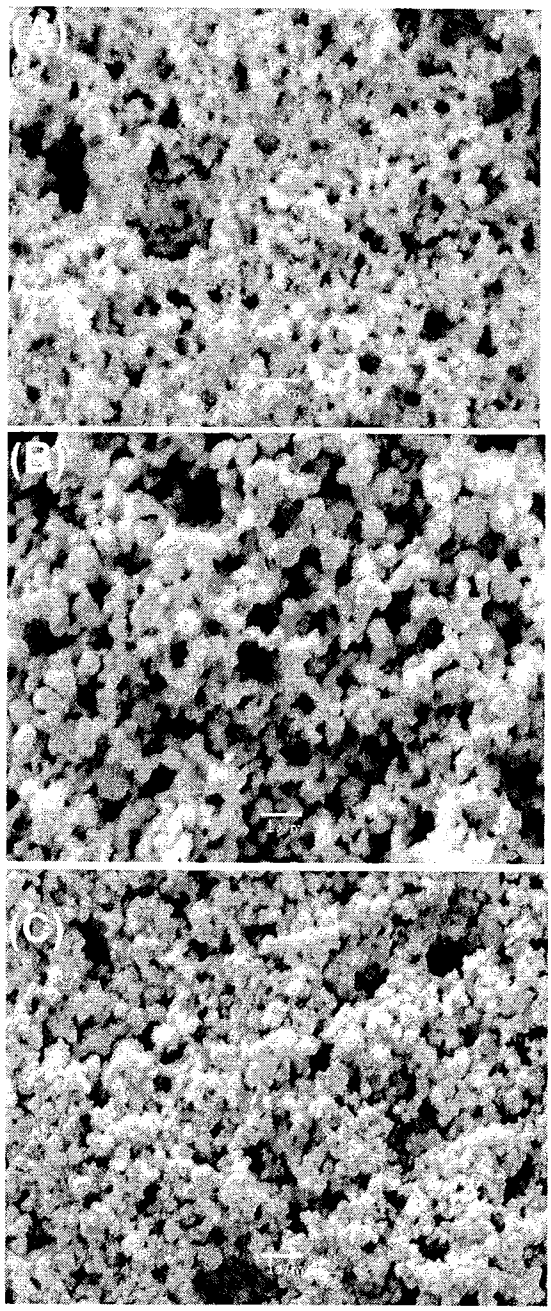

Figure 4.1 SEM images of the (A) Nanoporous Pt, (B) $Pt_{60}Ru_{40}$, (C) $Pt_{55}Ru_{30}Ir_{15}$

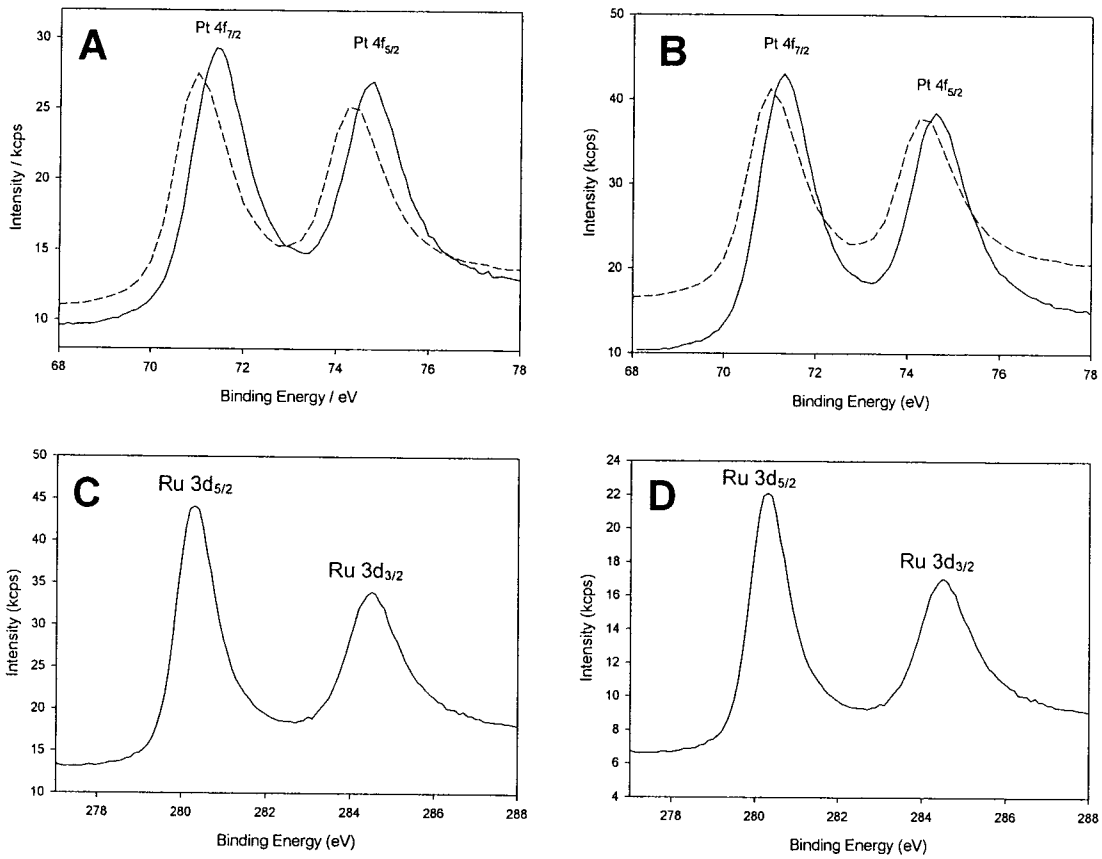

Figure 4.2 XP spectra of the Pt 4f region for the (A) PtRu and (B) PtRuIr electrodes, nanoporous Pt (dashed line) is included for comparison. XP spectra of the Ru 3d region for (C) PtRu and (D) PtRuIr electrodes.

respectively, was observed. Since a shift in the binding energy of core-level orbitals corresponds with a change in electron density, this indicates the presence of an electronic interaction between Pt and Ru and/or Ir, such as an intra-atomic charge transfer[42] .

XRD analysis was used to characterize the phase and structure of the as-synthesized nanoporous electrodes. As shown in Figure 4.3, the nanoporous (A)Pt, (B)PtRu and (C) PtRuIr electrodes all display the (111), (200) and (220) reflections characteristic of a face centered cubic (fcc) crystal structure. In comparison to nanoporous Pt, the PtRu and PtRuIr peaks have a positive shift in the 2θ values, which corresponds to decreased d-spacing values and lattice constants.

Further evidence was provided by quantitative calculations on the lattice constant (*a*) of the diffraction angles of the (220) reflection peak which revealed *a* values of 0.392, 0.390 and 0.390 nm for nanoporous Pt, PtRu and PtRuIr, respectively. The peak lines for the PtRu and PtRuIr electrodes appear between the reflections of pure Pt, Ru and Ir and there are no multiple (111), (200) or (220) reflections indicating the presence of pure metals in the XRD patterns.[43] The sum of this evidence indicates that the Pt, Ru and Ir are either fully or partially alloyed.[44-45]

4.3 CO oxidation on PtRuIr electrodes

CO has been identified as both an intermediate and poisoning species in the oxidation pathways of formic acid[46-47] , methanol[48-50] , and other small organic molecules on Pt. A desired characteristic of potential catalysts is a penchant towards removal of surface CO. At low potentials, CO can adsorb strongly to the Pt catalyst surface, thus inhibiting its performance. CO oxidation experiments, as described in section *2.3,* on the three nanoporous networks were performed in 0.5 M H_2SO_4 and the results are presented in Figure 4.4.

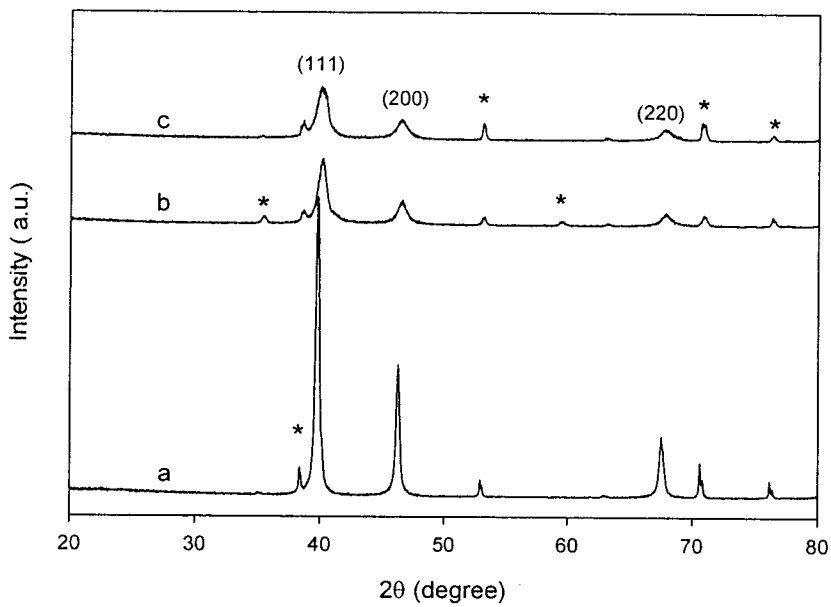

Figure 4.3. XRD Patterns (a) Nanoporous Pt, (b) $Pt_{60}Ru_{40}$, (c) $Pt_{55}Ru_{30}Ir_{15}$, (*) indicates Ti substrate peak.

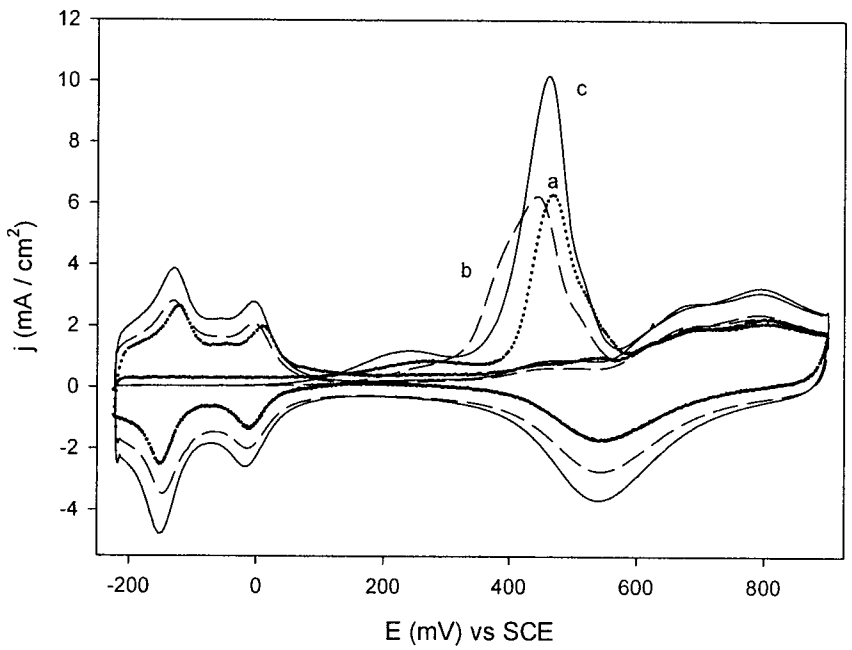

Figure 4.4 CO oxidation in 0.5M H_2SO_4 for (a) nanoporous Pt (dotted), (b)PtRu (dashed), (c) PtRuIr (solid)

The zero current at the beginning of the forward sweep in the hydrogen desorption region shows that hydrogen desorption from to the catalyst surface is completely repressed due to the adsorption of CO to the active sites. In the region from 0 to 600 mV a small, broad shoulder wave followed by a sharp peak representing CO oxidation can be seen for all three electrodes. In the reverse scan, the distinctive hydrogen adsorption peaks return and the CV resembles that of a CO free environment in H_2SO_4, showing complete removal of the adsorbed CO.

Nanoporous Pt shows an onset potential of 138 mV for the oxidation of adsorbed CO, while reaching its peak at 468 mV. Slightly out-performing this is the PtRu with an onset of CO oxidation at 15 mV and peak potential of 444 mV. This is due to the Ru sites on the nanoporous network generating oxygen species at lower potentials which serve to oxidize the adsorbed CO. The PtRuIr trimetallic electrode shows the greatest performance, with an onset potential of -47 mV and the highest current density at a peak potential of 450 mV. It is believed that this improvement can be attributed to the presence of Ir assisting in producing and stabilizing additional oxygen species, which in turn oxidize the adsorbed CO on the Pt sites.

The stripping of CO can also be used as a means of calculating the electroactive surface area of the catalysts.[19,51] The consumed charges from the CO stripping, calculated through the area under the CO oxidation peak are 19.98 mC, 25.98 mC and 30.32 mC for (a) nanoporous Pt, (b) PtRu, and (c) PtRuIr, respectively. By assuming a charge to surface area value of 420 $\mu C/cm^2$ for this process[19] , the electroactive surface areas of the electrodes were found to be 47.6, 67.9, 72.2 cm^2 for (a) nanoporous Pt, (b) PtRu, (c) PtRuIr. When compared to an electroactive surface area of $1 cm^2$ for polycrystalline Pt[43], it can be seen that an identical geometric surface for each electrode is not representative of the improvement provided through the nanostructured electrode surfaces.

4.4 Electrochemical Oxidation of Methanol

We first studied the electrochemical oxidation of methanol using cyclic voltammetry with the three samples with a 0.1M CH_3OH + 0.5 M H_2SO_4 solution and scan rate of 20 mV/s. The resulting voltammograms are displayed in Figure 4.5. (For the sake of clarity, only the forward sweeps are shown.) The addition of Ru to Pt, Figure 4.5A(b), lowers the onset potential and increases the peak current density of the oxidation of methanol; this is consistent with previous studies done within our group[43] . Figure 4.5A(c), the oxidation of methanol with the trimetallic PtRuIr, shows further improvement of the oxidation of methanol through the addition of Ir to the nanoporous network, producing a peak current density of 46 mA/cm^2. As with the oxidation of CO, the trimetallic alloy lowers the onset potential by 40 mV. Previous studies[43] have shown PtRu to give the lowest onset potential for methanol oxidation, but the addition of Ir further improves the ability of the catalyst. This can be attributed to the addition of Ir to the alloy, not to a simple increase in surface area. Previously in section *3.2*, the electroactive surface areas for all three electrodes were provided, and the largest electroactive surface area is provided by the trimetallic alloy. Figure 4.5B shows the methanol oxidation curve with the current densities corrected for the electroactive surface area. The PtRuIr, Figure 4.5B(c), once again shows the highest activity towards methanol oxidation when compared to the PtRu, thus showing that the addition of Ir, while providing a higher electroactive surface area, also enhances the performance of the catalyst.

The performance enhancement of the trimetallic alloy is also evident in a study of the steady state current densities of the electrodes in an identical solution as used in the methanol oxidation. The potential was held at 0 mV for 60s prior to stepping the potential up to the desired level of 300 mV or 600 mV where the potential is held for 500s. The amperometric responses of the Pt

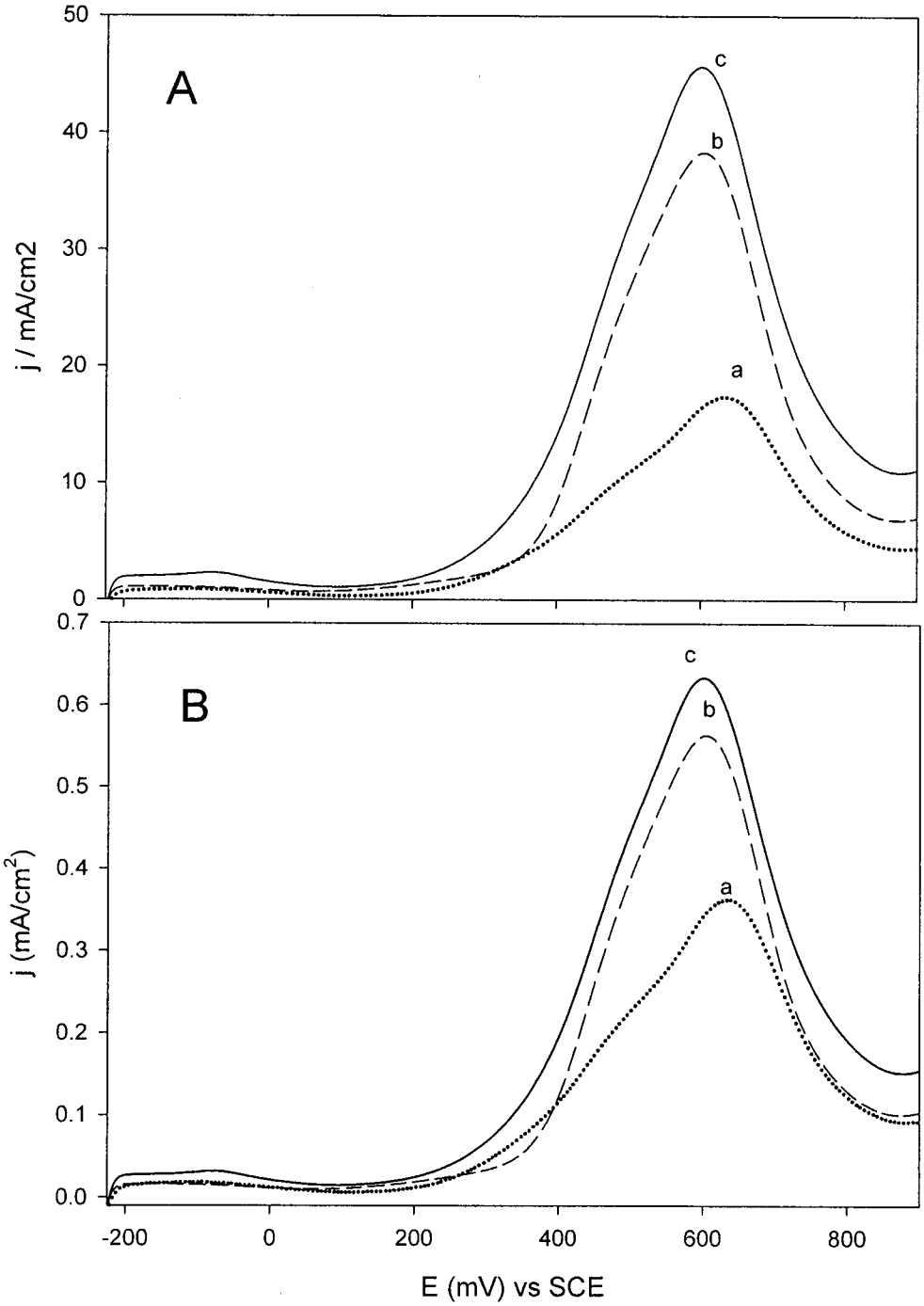

Figure 4.5 (A) MeOH oxidation 0.1M CH3OH + 0.5M H2SO4 for (a) nanoporous Pt, (b) PtRu (c) PtRuIr, (B) the CV for methanol oxidation, corrected for electroactive surface area

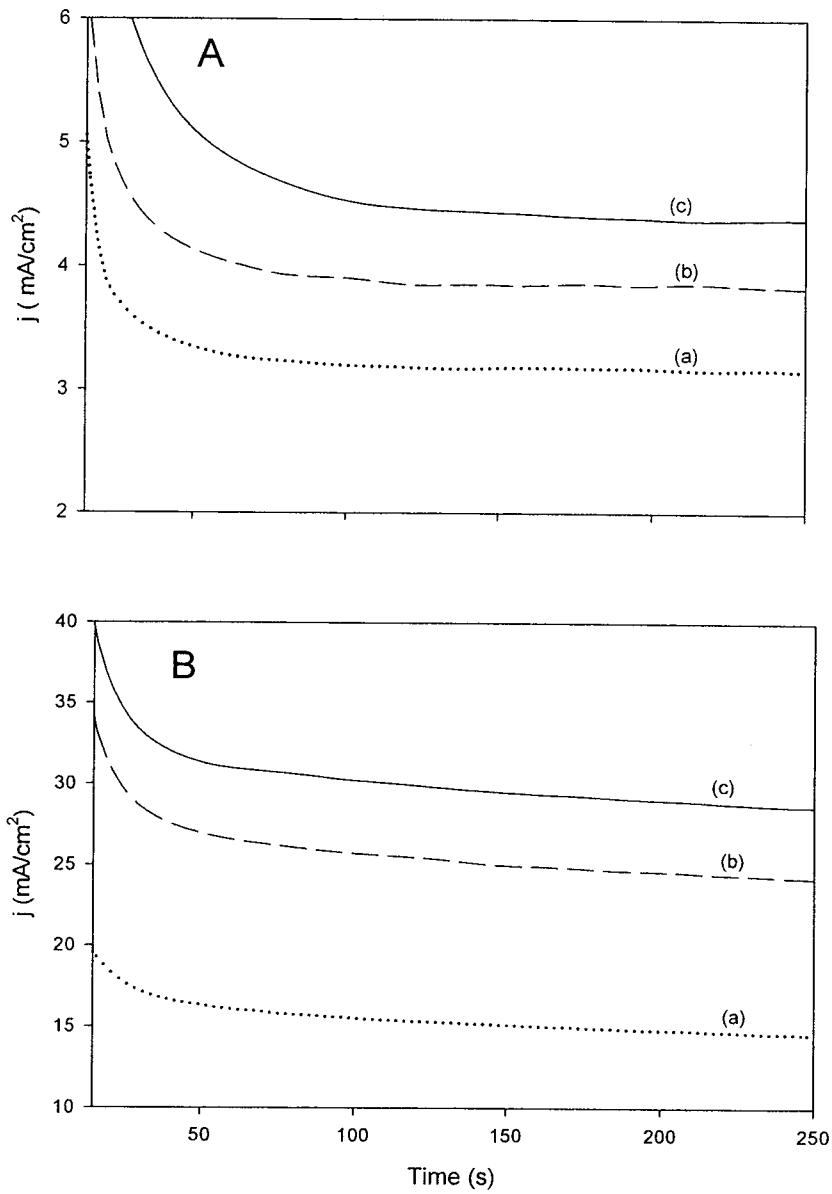

Figure 4.6 Chronoamperometry of the Nanoporous (a) Pt, (b) PtRu, and (c) PtRuIr in 0.5 M H_2SO_4 + 0.1 M CH_3OH at potentials of (A) +300 mV and (B) +600 mV. The potential was held at 0 mV for 60 s, before being stepped to desired potential for 300 s.

(a), PtRu (b) and PtRuIr (c), are shown in Figure 4.6A and 4.6B. After 200 s the electrodes achieve their steady-state currents. 300 mV is approximately the onset potential for methanol oxidation for all three electrodes, and at this potential the PtRuIr achieves the highest steady state current compared to Pt and PtRu. This can be attributed to the bifunctional pathway[52-53] of the PtRu being enhanced through the presence of Ir. The same trend is shown in Figure 4.6B, at 600 mV, where the peak current density for methanol oxidation is seen in the CV curves in Figure 4.5 prior to the electrode surface oxidation. The PtRuIr therefore shows high performance through the production of larger currents at low anodic potentials, assisting in the oxidation of methanol at these points, as well as at the point of the highest oxidation levels.

4.5 ATR-FTIR analysis of trimetallic alloy methanol oxidation.

The FTIR spectra collected in 0.1M CH_3OH + 0.5M H_2SO_4 can be seen in Figure 4.7. The base spectra, $R(E_1)$ was taken with an applied potential of -200 mV, while the $R(E_2)$ was collected with the applied potential varying from -100 mV to 600 mV, with each individual spectra displayed for (A) Nanoporous Pt, (B) PtRu, (C) PtRuIr. In Figure 4.7A, a negative going peak, corresponding to an increased amount of species at $R(E_2)$, appears at 3415 cm^{-1}; this is created by the ν(OH) mode of water at the platinum electrode[3] . Further, at 2343 cm^{-1}, a peak appears in the 600 mV spectra, due to the creation of CO_2 from the complete oxidation of methanol. Due to the design of our spectroelectrochemical system, CO_2 is free to exit the electrode surface to the bulk solution, however, it is detected upon creation in high quantity. (This trait will be further discussed with Figure 4.10) At 2054/2013 cm^{-1}, a bipolar band, which loses its bipolar feature to turn negative going at 600 mV, is present from linearly bonded CO_L, This peak shows abnormal behaviour with the positive portion appearing at higher frequency,

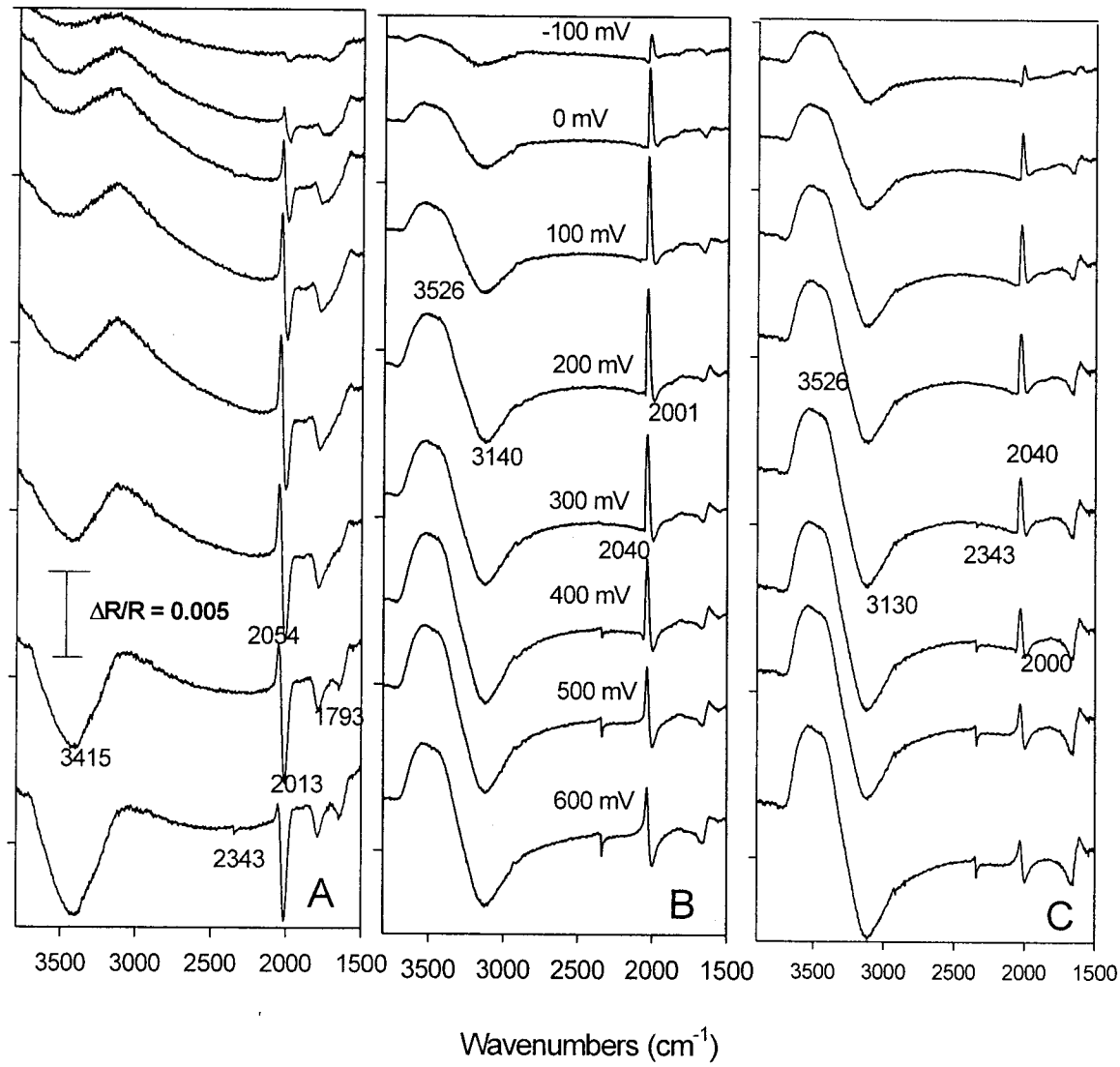

Figure 4.7. ATR-FTIR spectra of (A) Nanoporous Pt, (B) PtRu and (C) PtRuIr in 0.1M CH_3OH + 0.5 M H_2SO_4 with $R_{(El)}$ at -200 mV

which is the expected behaviour of CO at nanostructured Pt surfaces[54]. Also appearing at near the same rate is a negative going band at 1793 cm^{-1}, from the appearance of bridged CO,(CO_B). At higher potentials, a negative going band also appears at 1630 cm^{-1}. This peak is the bending mode of water $\delta_{(HOH)}$.

Figure 4.7B displays the spectra collected using the PtRu thin film electrode. A large broad peak with bipolar features is now present, the positive portion at 3526 cm^{-1} and the negative portion at 3140 cm^{-1}. We believe this bipolar feature arises due to the presence of the Ru co-catalyst. OH species are formed at the Ru sites at lower potentials than Pt, and Ru-OH has a higher IR absorption energy than Pt-OH[3] , thus creating this bipolar feature. The band at 2343 cm^{-1} (CO_2) appears first at 400 mV and grows until 600 mV. The bipolar CO_L peak is also present at 2040/2001 cm^{-1}. The final peak in the spectra is a band at 1647 cm^{-1}, with a bipolar feature. Figure 4.7C , from the oxidation of methanol using the trimetallic PtRuIr thin film electrode, shows similar features to that of Figure 4.7B, with the first bipolar band in the ν(OH) region appearing at a lower potential and having greater intensity. Also, the CO_2 peak at 2343 cm^{-1}, albeit small, appears earlier at 300 mV; this can be identified as a sign of the better performance of the trimetallic catalyst at lower potentials.

More information about the performance of the trimetallic catalyst's performance is found by studying the behavior of the CO present in the FTIR spectra of each catalyst. From Figure 4.7, we are unable to perform integration of the CO peaks to measure the extent of CO poisoning at the surface, due to their bipolar orientation. However, if a spectra at a high potential, $R_{(E1)}$ = 1000mV, where the catalyst surface is free of CO poisoning, is used as a reference, we can monitor the change in amount of CO. Figure 4.8 shows the FTIR spectra collected using this

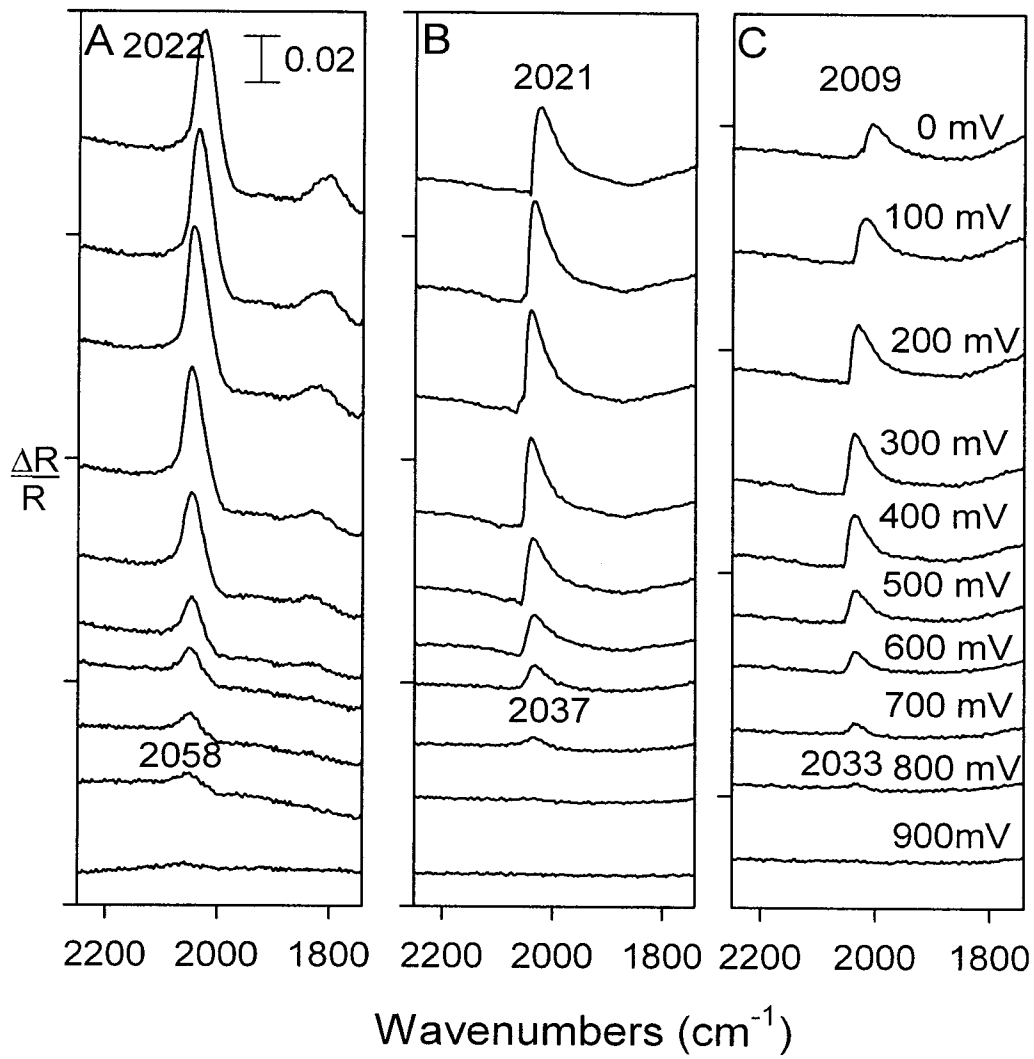

Figure 4.8 FTIR spectra for A) Pt, B) PtRu, C) PtRuIr with R(E1)=1000 mV showing the oxidation of CO in 0.5M H_2SO_4

method for A) Pt, B) PtRu, C) PtRuIr starting at 600mV. Now, the positive going peak present at 2027 cm^{-1} is due to the presence of larger amounts of CO present at the lower potential $R_{(E2)}$, once again displaying the abnormal behaviour of CO. Also, the CO_B band at 1807 cm^{-1} can only be seen in Figure 4.8A with Pt. In comparison, the trimetallic PtRuIr catalyst shows the least amount of CO on its surface, represented by the lower intensity of the CO_L peaks. The intensity of the total CO compared with potential is presented in Figure 4.9. At high potentials, little CO is present as it has been oxidized by this point; as the potential decreases, larger amounts of CO are present, until a slight drop is observed around 100mV, near the onset potential for methanol oxidation. As can be seen, the trimetallic PtRuIr, Figure 4.9(c), catalyst shows the lowest amount of CO present at its surface, definitely assisting in the performance enhancement.

From these spectra in Figure 4.8, an expected trend is also seen with the position of the CO_L band. A shift in the position of this band is observed as the applied potential is increased. Initially, for 4.8A Pt, the band appears at 2022 cm^{-1} and, as the potential is stepped up, this peak begins to shift to a higher frequency, with a maximum at 2058 cm^{-1}. At higher applied energies, the strength of the CO to metal bond increases due to the Stark effect[54] . This is also observed for the 4.8B PtRu (from 2021 cm^{-1} to 2037 cm^{-1}) and 4.8C PtRuIr (from 2009 cm^{-1} to 2033 cm^{-1}). The bipolar feature of the CO_L bands in the full spectra are created due to this shift.

Figure 4.10 presents the second ATR-configuration for the oxidation of methanol using the three test samples. Herein, the species which become desorbed from the electrode surface, will appear in the IR spectrum as they become trapped in the thin layer of solution. We can utilize this technique to garner a measure of the overall performance of the three catalysts. The main feature to be studied here is the appearance and intensity of the CO_2 band appearing at

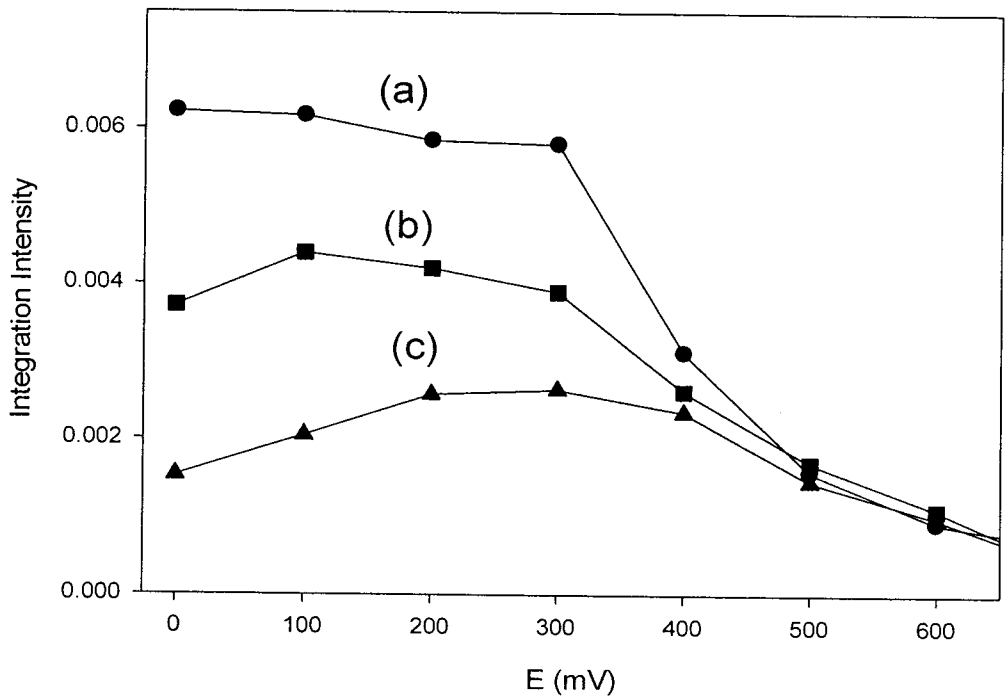

Figure 4.9 Comparison of the intensity of total CO vs applied potential based on CO_L band present in Figure 4.8.

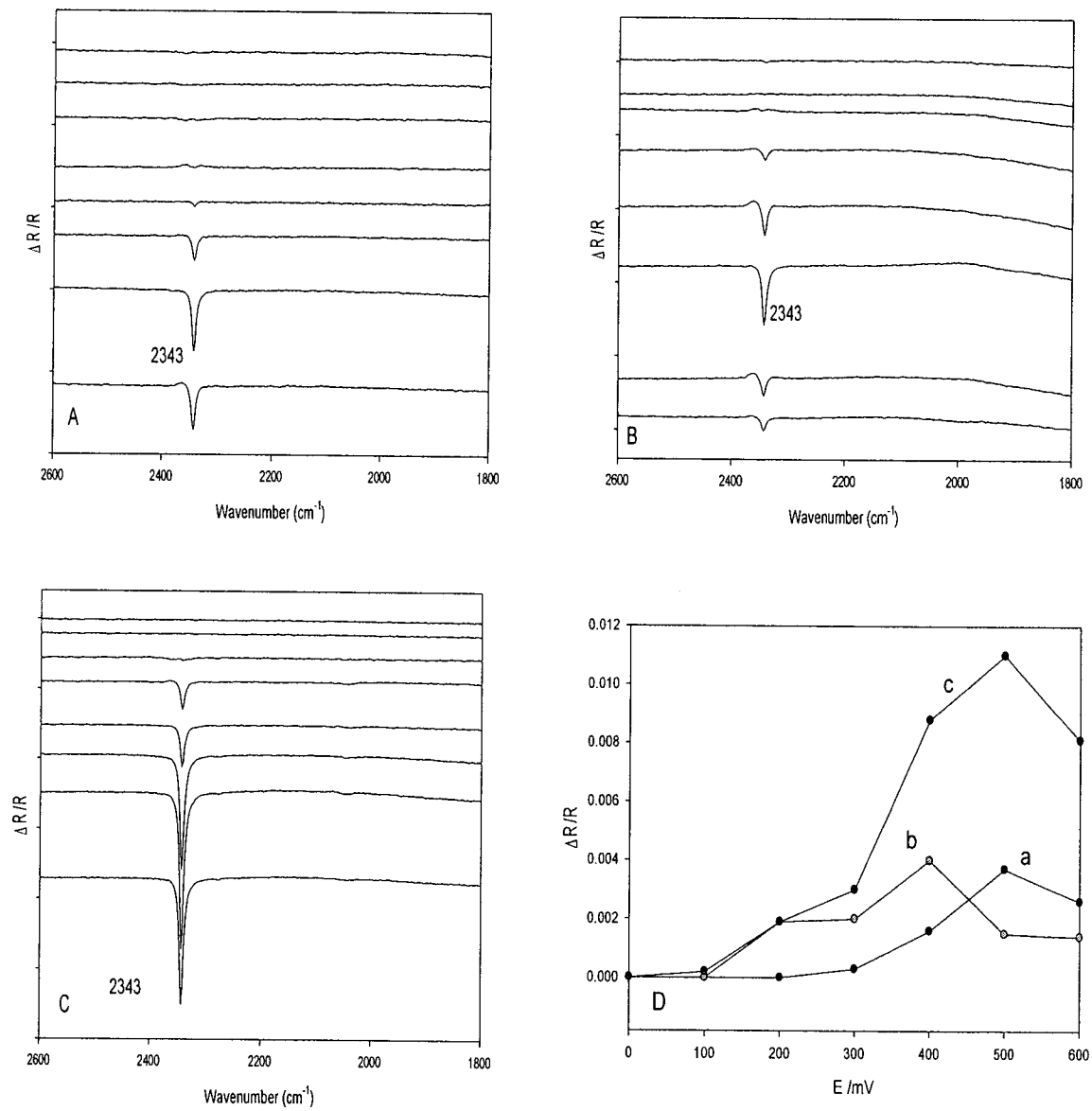

Figure 4.10 ATR-FTIR spectra collected in 0.1M CH_3OH + 0.5M H_2SO_4 for A) Pt B) PtRu C) PtRuIr displaying the appearance of CO_2 in the thin electrolyte layer as methanol is completely oxidized. D) comparison of the intensity of CO_2 as a variable of increasing applied potential.

~2343cm^{-1}. CO_2, as the final product of methanol oxidation, will provide an accurate account of the efficiency of the catalyst. In Figure 4.7, we cannot get an accurate representation of the extent of methanol oxidation, as desorbed species (such as CO_2) return to the bulk solution. Figure 4.10A shows the behavior of nanoporous Pt in the oxidation of methanol. The final product in the oxidation of methanol is CO_2 and this appears at 300 mV, corresponding to the onset of methanol oxidation seen in Figure 4.5. PtRu 4.10B also shows the production of CO_2, at 200 mV first appearance. The trimetallic catalyst, Figure 4.10C, has CO_2 appearing in a small amount at 100mV spectra, thus showing the earliest onset for methanol oxidation, due to the presence of Ir. This CO_2 band can be used to show the efficiency of each catalyst, and CO_2 is the final product in the oxidation of methanol. A larger amount of CO_2 shows a very efficient catalyst. Figure 4.10D gives a measure of the total intensity of CO_2 in the three methods versus applied potential. As can be seen, the largest amount of CO_2, and thus the largest extent of methanol oxidation through stronger performance, comes from the trimetallic PtRuIr.

The spectra described above give further information as to how the presence of Ir in the PtRu catalyst improves its activity. The bipolar feature for the ν(OH) range in the PtRu, and PtRuIr spectra shows the improvement for the oxidation of methanol through the addition of a co-catalyst to the Pt network. In Figure 4.7A , only a negative-going peak is present, due to an increased amount of water being brought to the electrode surface at the Pt sites to assist in removal of adsorbed surface CO at higher potentials, typical of Pt electrodes. In 4.7B and 4.7C, the bipolar feature of this band is due to a different mechanism occurring. In 4.7C, the higher intensity and quicker onset of this band is due to the presence of Ir enhancing the amount of OH-like species on the surface, thus driving the reaction further at lower potentials. The amount of CO at the electrode's surface is lowest for the PtRuIr, as shown in Figure 4.9, with less CO at the

surface, the catalyst will perform more strongly. Figure 4.10 tells of the efficiency of the catalysts by monitoring CO_2 production. The trimetallic PtRuIr, produces CO_2 at the lowest applied potential, 100mV, and also displays the largest extent of methanol oxidation making it the most efficient and strongest performing catalyst. The combination of the knowledge gathered through FTIR spectroscopy further illustrates the performance enhancement of PtRu with Ir.

4.6 Summary

In summary, novel 3D nanoporous trimetallic PtRuIr networks were fabricated with the facile one-step hydrothermal technique. The presence of Ir, in a molar ratio determined through the ratio of the metal precursor solutions, enhances the performance of PtRu. CV curves from the CO-stripping experiments show trimetallic PtRuIr providing the lowest onset potential as well as highest peak current density, with an identical trend appearing in the study of methanol oxidation. From the CO stripping curve, the calculation of the electroactive surface area can be performed. Upon correcting for the electroactive surface areas, in the methanol oxidation curve, it can be seen that the presence of Ir has a positive effect on the performance of the PtRu network. We believe the addition of the Ir co-catalyst improves the production of oxygen containing species at lower potentials, which can serve to oxidize the poisoning adsorbed CO. Through the addition of a small amount of Ir, the oxidation of methanol is improved. FTIR spectroscopy further backs this claim through three sources., 1)by providing insight into a change in the behaviour of water and OH species at the electrode surface in PtRu and $Pt_{55}Ru_{30}Ir_{15}$ compared with Pt, 2) a lower amount of CO at the trimetallic electrode surface, 3) lowest onset and largest extent of methanol oxidation through monitoring of the production of CO_2. Thus, in this chapter

a very promising trimetallic PtRuIr alloy for electrochemical oxidation of methanol was described.

4.7 References

1. Liu, H.; Zhang, L.; Zhang, J.; Wang, H.; Wilkinson, D.P. *J. of Power Sources* **2006,** 155, 95
2. Jiang, R.; Chu, D. *J. of Power Sources* **2006,** 161, 1192
3. Yajima, T.; Uchida, H.; Watanabe, M. *J. Phys. Chem. B.* **2004**, 108, 2654
4. Andreaus, B.; Eikerling, M. *Chem. Mater.* **2007**, 607, 121
5. Xia, M.; Wang, Q.; Eikerling, M.; Lui, Z. *Can. J. Chem.* **2008**, 86, 657
6. Wu, Y.M.; Li, W.S.; Lu, D.S.; Fu, J.M. *J. of Power Sources* **2005,** 145, 286
7. Martinez-Huerta, M.V.; Rodriguez, J.L.; Tsiouvaras, N.; Pena, M.A.; Pierro, J.L.G.; Pastor E. *Chem. Mater.* **2008**, 20, 4249
8. Bock, C.; Paquet, C.; Couillard, M.; Botton, G.A.; MacDougall, B.R. *J. Am. Chem. Soc.* **2004,** 126, 8028
9. Lin, W.F.; Iwasita, T.; Vielstich, W. *J. Phys. Chem. B* **1999,** 103, 3250
10. Gojkovic, S.L.; Vidakovic, T.R.; Durovic, D.R. *Electrochoim. Acta.* **2003,** 48, 3607
11. Peng, X.; Koczkur, K.; Chen, A. *Nanotech.* **2007,** 18, 561
12. Jiang, J.; Kucernak, A. *Chem. Mater*, **2004**, 16, 1362
13. Jiang, L.; Sun, G.; Sun, S.; Liu, J.; Tang, S.; Li, H.; Zhou, B.; Xin, Q. *Electrochim. Acta.* **2005,** 50, 5384
14. Colmati, F.; Antolini, E.; Gonzalez, E.R. *Electrochim. Acta.* **2005,** 50, 5496
15. Guo, Y.G.; Hu, J.S.; Zhang, H.M.; Liang, H.P.; Wan, L.J.; Bai, C.L. *Adv. Mater. (Weinheim, Ger.)* **2005,** 17, 746
16. Jayaraman, S.; Jaramillo, T.F.; Baeck, S.H.; McFarland, E.W. *J. Phys. Chem. B* **2005,** 109, 22958
17. Yang, L.X.; Bock, C.; MacDougall, B.; Park, J. *J. Appl. Electrochem.* **2004,** 34, 427
18. Raychowdhury, C.; Matsumoto, F.; Zeldovich, V.B.; Warren, S.C.; Mutolo, P.F.; Ballesteros, M.J.; Wiesner, U.; Abruna, H.D.; DiSalvo, F.J. *Chem Mater*, **2006,** 18, 3365

19. Wang, J.; Asmussen, R.M.; Adams, B.; Thomas, D.F.; Chen, A. Chem. Mater, 2009, 21, 1716

20. Moore, J.T.; Chu, D.; Jiang, R.; Deluga, G.A.; Lukehart, C.M. *Chem. Mater.*, **2003**, 15, 1119

21. Koczkur, K.; Yi, Q.; Chen, A. *Adv. Mater.* **2007,** 19, 2648

22. Ren, X.; Wilson, M.S.; Gottesfeld, S.; J. *Electrochem. Soc.* **1996**, 143, L12

23. Basnayake, R.; Li, Z.; Lakshmi, S.; Zhou, W.; Smotkin, E.S.; Casadonte, D.J.; Korzeniewski, C. *Langmuir* **2006**, 22, 10446

24. Hogarth, M.P.; Ralph, T.R. *Platinum Met. Rev.* **2002**, 46 117

25. Hogarth, M.P.; Ralph, T.R. *Platinum Met. Rev.* **2002**, 46 146

26. Holt-Hindle, P.; Nigro, S.; Asmussen M.; Chen, A. *Electrochem. Commun.* **2008,** 10, 1438

27. Chen, A.; La Russa D.J.; Miller, B. *Langmuir* **2004,** 20, 9695

28. Yan, Y.G.; Li, Q.X.; Huro, S.J.; Ma, M.; Cai, W.B.; Osawa, M. *J. Phys. Chem. B.* **2005**, 109, 7900

29. Miyake, H.; Okada, T.; Samjeske, G.; Osawa, M. *Phys. Chem. Chem. Phys.* **2008,** 10, 3662

30. Liu, Y.; Muraoka, M.; Mitsushima, S.; Ota, K.I.; Kamiya, N. *Electrochim. Acta.*, **2007**, 52, 5781

31. Kunimatsu, K.; Uchida, H.; Osawa, M.; Watanabe, M. *J. Electroanal. Chem.* **2006**, 587, 299

32. Park, Y.J.; Kim, J.H. *J. Disp. And Sci. Tech.* **2003**, 24, 537

33. Szabo, T.; Szekeres, M.; Dekany, I.; Jackers, C.; De Feyter, S.; Johnston, C.T.; Schoonheydt, R.A. *J. Phys. Chem. C* **2007**, 111(34), 12730

34. Mondelli, C.; Ferri, D.; Grunwaldt, J.D.; Krumeich, F.; Mangold, S.; Psaro, R.; Baiker, A. *J. Catal.* **2007**, 252, 77

35. Wang, M.L.; Zhang, Y.Y.; Xie, Q.J.; Yao, S.Z. *Electrochim. Acta.* **2005**, 51, 1059

36. Ohman, M.; Persson, D. *Electrochim. Acta.* **2007**, 52, 5159

37. Heinen, M.; Chen, Y.X.; Jusys, Z.; Behm, R.J. *Electrochim. Acta.* **2007**, 53, 1279

38. Sun, S.G.; Christensen, P.A.; Wieckowski, A. *In-Situ Spectroscopic Studies of Adsorption at the Electrode and Electrocatalysis*, Elsevier, Netherlands **2007**

39. Li, H.Q.; Chen, A.; Roscoe, S.G.; Lipkowski, J. *J. Electroanal. Chem.* **2001**, 500, 299

40. Wagner, C.D.; Riggs, W.M.; Davis, L.E.; Moulder, J.F.; Muilenberg, G.E. Handboook X-ray Photoelectron Spectroscopy, Perkin-Elmer Co. **1979**

41. Aric, A.S.; Creti, P.; Kim, H.; Mantegna, R.; Giordano, N.; Antonucci. V. *J. Electrochem. Soc.* **1996**, 143, 3950

42. Ioroi, T.; Yasuda, K. *Journal of The Electrochemical Society*, **2005**, 152, A1917

43. Wang, J.; Holt-Hindle, P.; MacDonald, D.; Thomas, D.; Chen, A. *Electrochim. Acta.* **2008,** 53, 6944

44. Gasteiger, H.A.; Markovic, N.; Ross Jr, P.N.; Cairns, E.J. *J. Phys. Chem.* **1993**, 97, 12020

45. Arico, A.S.; Antonucci, P.L.; Modica, E.; Bagilo, V.; Kim, H.; Antonucci, V. *Electrochim. Acta.* **2002**, 47, 3723

46. Casado-Rivera, E.; Volpe, D.J.; Alden, L.; Lind, C.; Downie, C.; V'azquez-Alvarez, T.; Angelo, A.C.D.; DiSalvo, F.J.; Abruna, H.D. *J. Am. Chem. Soc.* **2004** 126 4043

47. Liang, Y.; Zhang, H.; Zhong, H.; Zhu, X.; Tian, Z.; Dongyan, X.; Yi, B. *J. Catal.* **2006**, 238, 468

48. Sanicharin, S.; Bo, A.; Sompalli, B.; Gurau, B.; Smotkin, E.S. *J. Electrochem Soc.* **2002**, 149, A554

49. Tkach, I.; Panchenko, A.; Kaz, T.; Gogel, V.; Friedrich, K.A.; Roduner, E. *Phys. Chem. Chem. Phys.* **2004**, 6, 5419

50. Chen, Y.A.; Ye, S.; Heinen, M.; Jusys, Z.; Osawa, M.; Behm, R.J. *J. Phys. Chem. B.* **2006**, 110, 9534

51. Yeager, E.; Bockris, J.O.; Conway, B.E.; Sarangapani, S.; Comprehensive Treatise of Electrochemistry, *Electrodics: Experimental* Techniques, vol 9, Plenum Press, New York, 1984

52. Park, K.W.; Sung, Y.E. *J. Phys. Chem. B* **2005**, 109, 13585

53. Liu, Z.; Lee, J.Y.; Chen, W.; Han, M.; Gan, L.M. *Langmuir* **2004,** 20, 18

54. Lu, G.Q.; Sun, S.G.; Cai, L.R.; Chen, S.P.; Tian, Z.W.; Shui, K.K. *Langmuir* **2000**, 16, 778

Chapter 5

In situ ATR-FTIR study of the electrochemical oxidation of glucose on Pt-based nanostructured materials

5.1 Introduction

Over two million Canadians are affected by diabetes mellitus, which has become a worldwide health problem. This is a metabolic disorder in which insulin deficiency and hyperglycemia results in glucose levels falling outside of the normal range of 4.4-6.6mM. Diabetes has fast become one of the leading causes of death and disability in the world.[1] There is now a large demand for a quick and precise method for monitoring blood glucose levels to treat diabetes.[2-5] Over the past 40 years, much work has been done towards the development of a glucose sensor based on the use of an enzyme. However, some main drawbacks are that temperature, chemical and thermal instabilities, pH, and humidity can all denature the enzymes, thus hindering the performance of an enzyme sensor. Metal catalysts have been proposed as potential glucose sensors, with platinum leading this group.[6]

There exist three potential ranges in the electrochemical behaviour of glucose with the use of platinum at pH 7.0. Between -0.09 and 0.11V (vs. SCE) is referred to as the hydrogen region, where glucose adsorbs to the Pt surface through its OH bonds. Following this, there exists a double layer region between 0.16 and 0.56 V, in which only charging and double layer capacitance occur. Above a level of 0.86 V, the Pt surface becomes oxidized and cannot function further as a glucose chemical sensor.[7] Bulk metallic Pt surfaces have slow oxidation kinetics of glucose, with poor sensitivity and selectivity. However, nanostructured Pt-based materials show great promise in the preparation of a functional chemical sensor. An example

being highly ordered Pt-nanotube arrays, which were fabricated through electrochemical deposition, showed increased activity and sensitivity towards glucose oxidation.[8] Work has also been done modifying the Pt catalyst as Pt has high cost, and can also become poisoned if complete oxidation of glucose is carried out by intermediate species such as CO. Examples of co-catalysts added to improve the performance of Pt include Bi, Pb, Tl, WO_3.[9-12] Three very successful Pt-based nanostructures which have shown promise for glucose oxidation are PtIr, PtPb, and PtRu.[13-15] While electrochemical testing can provide information regarding the performance of the catalysts towards glucose oxidation, distinct mechanistic information is required to understand how the catalysts are improving the performance. This chapter will discuss mechanistic information gathered using the two ATR-FTIR systems for the oxidation of glucose using Pt, PtRu, PtIr, and PtPb.

5.2 Electrochemical Performance of Catalysts

Figure 5.1A displays the electrochemical oxidation of glucose using the 4 samples in 20 mM glucose + 0.1M PBS. In the oxidation using PtIr (long dash) a single peak at -300 mV is first observed (two peaks in this region for Pt) as the first step of the oxidation of glucose occurs; following this, a second band at 175 mV appears, due to the adsorption of glucose and conversion to one of its many intermediates, (which may overlap in this region) followed by the oxidation of glucose into its final products. The Pt displays lower current response, and a negative trait due to interference from intermediates. The short dashed line in Figure 5.1A. shows the oxidation of glucose with the PtRu electrode which displays similar traits to those of the Pt and PtIr. Finally the PtPb (shown as a dotted line) shows a large initial response, and a lower current response in the upper region. This is due to less intermediate species being present to be oxidized at higher potentials.[14] The same samples were tested with 20 mM glucose

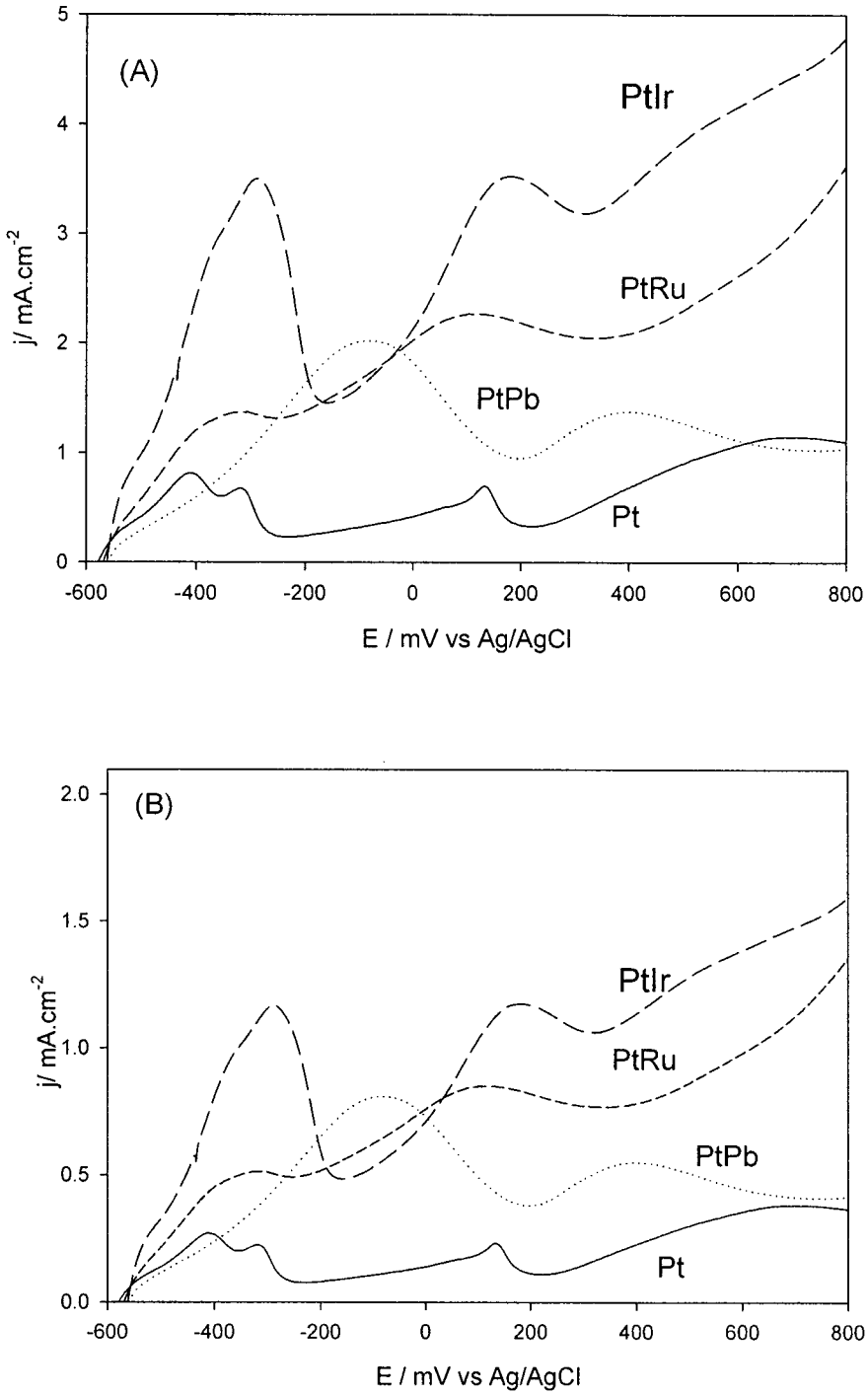

Figure 5.1 Cyclic voltammograms in 20mM d-Glucose in (A) 0.1M PBS for Pt (solid line) and PtRu (short dash), PtIr (long dash), PtPb (dotted) at a scan rate of 20mV/s and in (B) 0.1M $HClO_4$

+0.1M $HClO_4$. Similar trends in the CV are observed in Figure 5.1B, with a lower current response produced. Electrochemical studies are the standard test method in the development of an electrochemical glucose sensor, the following sections show how the ATR-FTIR is used to further understand the electrochemical results of glucose oxidation.

5.3 Oxidation of Glucose in PBS – Internal Study

Figure 5.2A displays the ATR-FTIR spectra using a thin film nanoporous Pt electrode with 100 ppm D-glucose + 0.1M PBS and the internal configuration. The spectra have a slight negative going band at 3450 cm^{-1} as water is brought to the surface to help oxidize the glucose. A CO band appears in the -400 mV spectra and grows with a bipolar feature until 300 mV, in which any CO previously present has been oxidized. Moving further, a negative going band at 1790 cm^{-1} appears and grows until 200 mV due to carbonyl groups being formed at the catalyst surface. Another band at 1097 cm^{-1} also appears negative going, due to an increased amount of a C-O group at the higher potential[16].

The second sample, PtRu, is a very strong electrocatalyst for the oxidation of small organic molecules and has shown selectivity towards the oxidation of glucose[16]. From the ATR-FTIR data collected the performance of PtRu can be examined. Figure 5.2B shows the internal configuration results from analyzing the PtRu electrocatalyst surface in the oxidation of glucose. In the displayed spectra, there is a positive going band at 2010 cm^{-1} due to CO_L forming in larger amounts, (abnormal behaviour of CO[17]). A positive band is present at 1817 cm^{-1}, as well as negative bands at 1695 cm^{-1} and 1640 cm^{-1}.

PtIr has been used as a potential candidate for a glucose chemical sensor[13]. In its electrochemical study, two clear bands appear, standard glucose oxidation curves. The catalyst

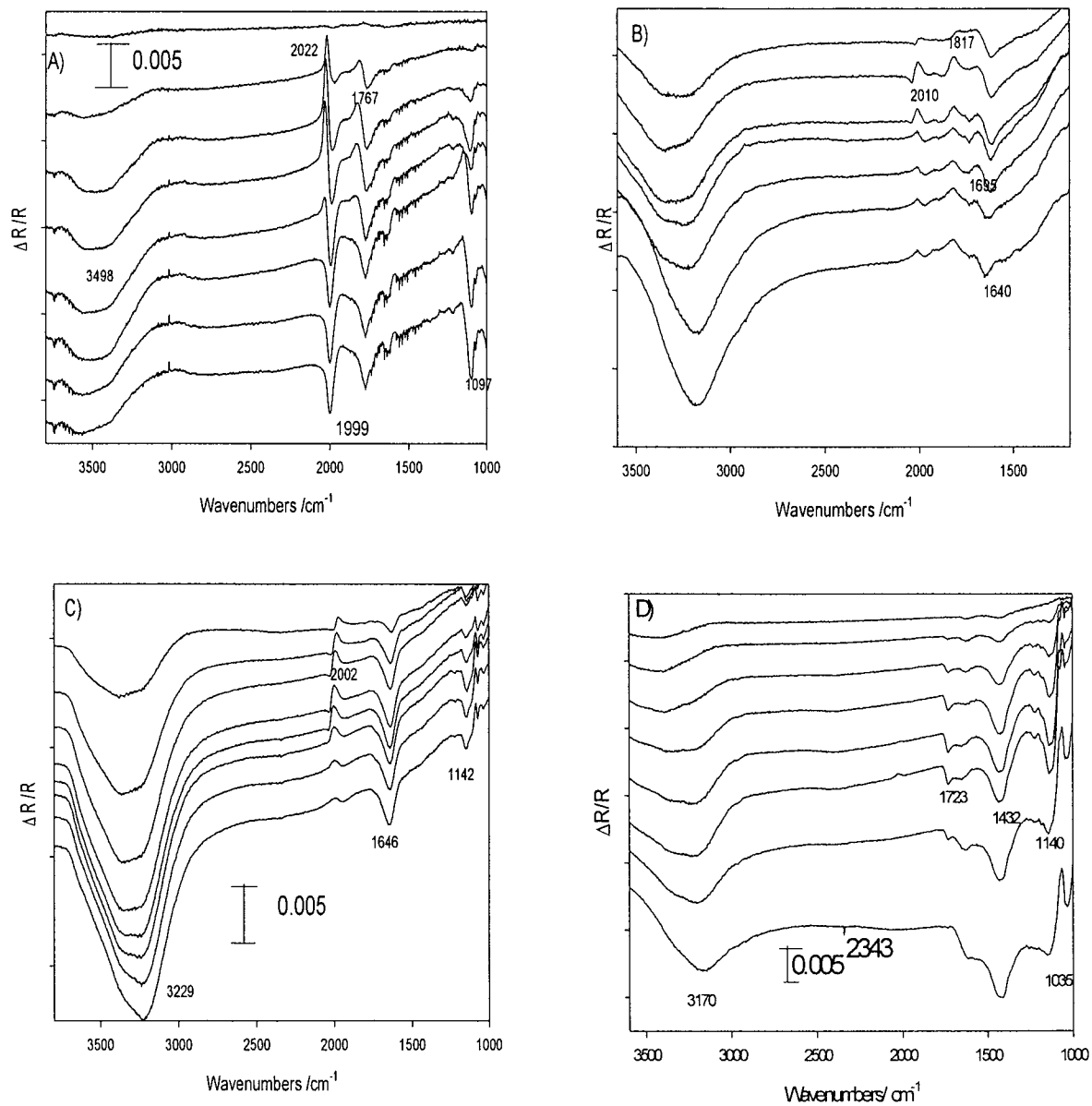

Figure 5.2 The oxidation of glucose (0.01M d-glucose in 0.1M PBS) monitored with the ATR-FTIR internal technique for A) Pt, B) PtRu, C)PtIr, D)PtPb with $R_{(E1)}$ set at -600 mV

performs strongly in the presence of interfering species[13]. Through monitoring with ATR-FTIR, some useful information is gained as shown in Figure 5.2C. As the reaction proceeds with a base spectrum collected at -600 mV, a positive going CO_L band appears due to an increased amount of carbon monoxide at the higher potential levels. In the ν(OH) region, a negative going band appears as water species are brought to the catalyst surface. A second band at 1142 cm^{-1} is present in this spectral series and grows with increasing the potential.

One of the most successful catalysts for the oxidation and detection of glucose, due to limited interference from intermediates, is PtPb[15]. This catalyst out performs the others studied here and the reason is seen in the data collected using ATR-FTIR. In Figure 5.2D, as the potential is increased, no CO is present at the surface of the catalyst, while a CO_2 band at 2343 cm^{-1} appears. A band at 1723 cm^{-1} appears and grows with potential increases, as well as a band at 1423 cm^{-1}, which does not appear in the other catalysts' spectra. The lack of CO shows that, in the complete oxidation of glucose, CO is not able to poison the catalyst surface as CO_2, the final possible product, is produced. All peak assignments can be found in Table 5.1

5.4 Oxidation of glucose in PBS – external study

Due to the orientation of this ATR-FTIR set-up, species which desorb from the catalyst surface are free to re-enter the bulk solution and become blind to the IR beam. The external ATR-FTIR configuration traps a thin layer of solution between the electrode and window, thus overcoming this issue. Using a bulk nanoporous Pt electrode and a 0.1M PBS electrolyte, the oxidation of glucose was monitored. In the spectra seen in Figure 5.3A, negative going bands appear at 2343 cm^{-1} (400 mV), 1740 cm^{-1} (0mV), 1629 cm^{-1}, 1558 cm-^{1} ,1405 cm^{-1} and 1239 cm^{-1}. The spectral assignments can be seen in Table 5.1. For the PtRu catalyst, an identical

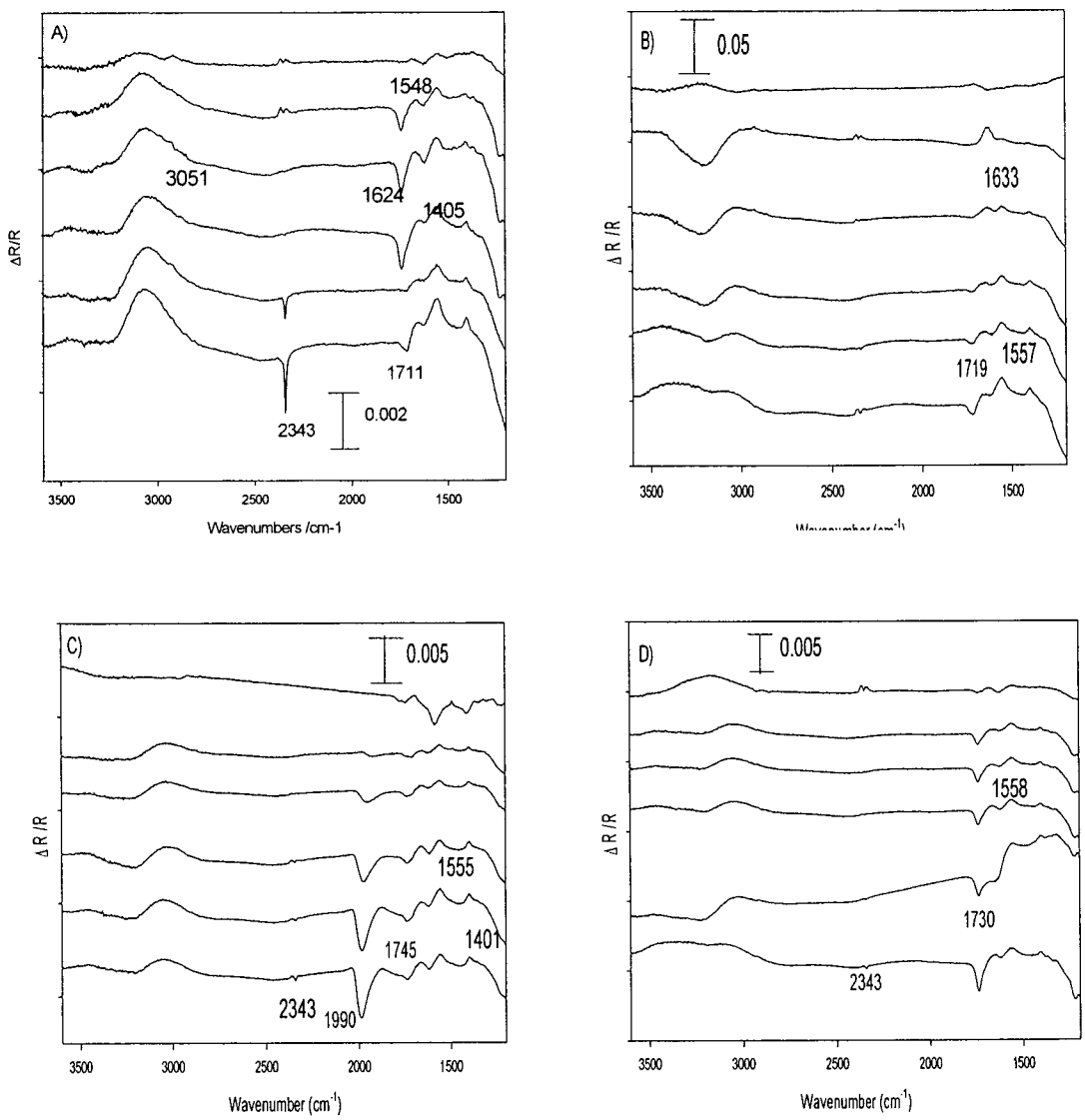

Figure 5.3 The oxidation of glucose (0.01M d-glucose in 0.1M PBS) monitored with the ATR-FTIR external technique for A) Pt, B)PtRu, C)PtIr, D) PtPb with $R_{(E1)}$ set at -600 mV

solution to that of the first test was added and, using a base of -600mV, a new spectrum is collected every 200mV with the resulting spectra are displayed in Figure 5.3B. Negative going bands appear at 2343 cm^{-1} (400mV) and1725 cm^{-1} (400mV). Also, positive bands at 1564 and 1403 cm^{-1} appear. There exists a multitude of bands below 1200 cm^{-1} due to the PBS electrolyte (due to intensity and size of these bands, this is not displayed).

Information from the solution close to the catalyst surface was gathered using the PtIr catalyst. In the spectra displayed in Figure 5.3C, there are negative going bands at 2344 cm^{-1} (200mV), 1995 cm^{-1} (0mV), 1740 cm^{-1} (0mV) and 1618 cm^{-1}. Positive bands are present at 3055 cm^{-1}, 1569 cm^{-1} and 1400 cm^{-1}.

Utilizing the PtPb catalyst, Figure 5.3D, the spectra display several features as species desorb from the catalyst surface and into the bulk solution. Negative going bands are observed at 2343 cm^{-1} (starting at 400mV), 1740 cm^{-1}, 1623 cm^{-1}, and 1232 cm^{-1} (-200mV), while positive going bands appear at 1566 cm^{-1} and 1407 cm^{-1}. Also present are the peaks below 1200 cm^{-1} due to the PBS solution.

5.5 Oxidation of Glucose in $HClO_4$ –external study

Due to the interference below 1200cm^{-1} from the PBS solution, these external configuration experiments were repeated using $HClO_4$ as an electrolyte. For the nanoporous Pt (Figure 5.4A), negative going bands appears at 2343 cm^{-1} (200 mV), 1740 cm^{-1} (0 mV), 1629 cm^{-1}, 1239 cm^{-1}, 1193 cm^{-1}, and 1125 cm^{-1}. There are also positive going bands at 3260 cm^{-1}, 2920 cm^{-1}, and 2859 cm^{-1}. All peak assignments for the corresponding bands are found in Table 5.1. For the PtRu, , Figure 5.4B, there are negative going bands at 2343 cm^{-1} (400 mV), 1626 cm^{-1} and 1105 cm^{-1}. A large positive going band appears at 3260 cm^{-1}; this is evidence of water being

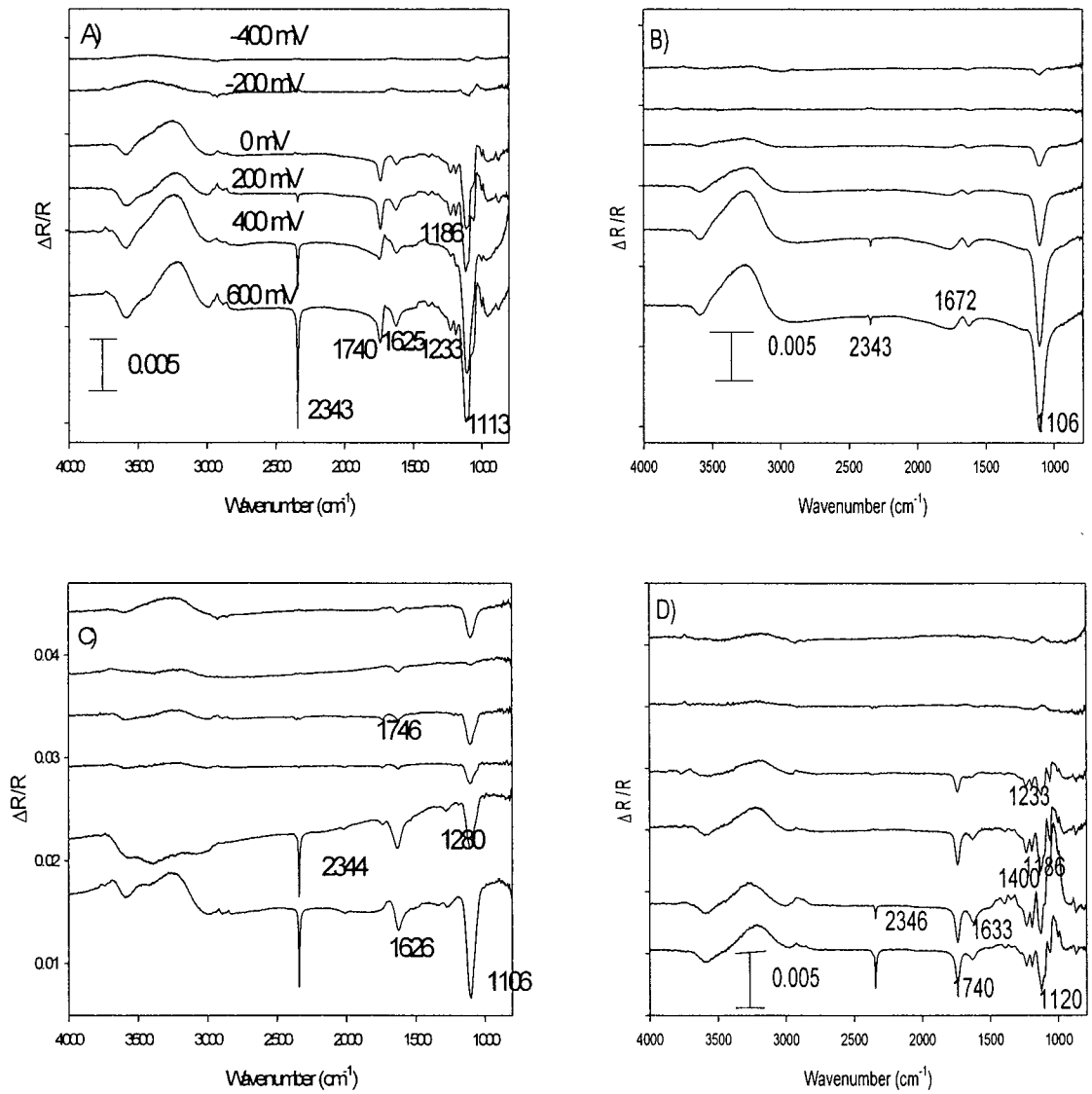

Figure 5.4 The oxidation of glucose (0.01M d-glucose in 0.1M $HClO_4$) monitored with the ATR-FTIR external technique for A) Pt, B)PtRu, C)PtIr, D) PtPb with $R_{(E1)}$ set at -600 mV

Catalyst	Technique	Wavenumber /cm^{-1}	Direction	Identity
Pt				
	Internal			
		3450	+ve	OH
		2071/2040	bipolar	CO_L
		1790	-ve	C=O
		1101	-ve	C-O (alcohol/ester)
	External -PBS			
		2343	-ve	CO_2
		1740	-ve	C=O
		1629	-ve	H_2O
		1558	+ve	RCO_2^-
		1405	+ve	RCO_2^-
		3260	+ve	OH
		2920	+ve	C-H
		2859	+ve	C-H
	External – $HClO_4$			
		2343	-ve	CO_2
		1740	-ve	C=O
		1629	-ve	H_2O
		1239	-ve	C-O (carboxylic acid)
		1193	-ve	C-O(alcohol/Ester)
		1125	-ve	C-O(alcohol/ester)
		3260		OH
		2920		C-H
		2859		C-H
PtRu				
	Internal			
		2010	+ve	CO_L
		1817	+ve	CO_B
		1710	-ve	C=O
		1650	-ve	H_2O
	External -PBS			
		2343	-ve	CO_2
		1725	-ve	C=O
		1564	+ve	RCO_2^-
		1403	+ve	RCO_2^-
	External- $HClO_4$			
		2343		CO_2

		1626		OH
		1105		C-O
PtIr				
	Internal			
		2002	+ve	CO
		3350	-ve	H_2O
		1142	-ve	C-O
	External - PBS			
		2344	-ve	CO_2
		1995	-ve	C=C=O
		1740	-ve	C=O
		1618	-ve	H_2O
		3055	+ve	OH
		1569	+ve	RCO_2^-
		1400	+ve	RCO_2^-
	External – $HClO_4$			
		2343	-ve	CO_2
		2018	-ve	C=C=O
		1737	-ve	C=O
		1626	-ve	OH
		1280	-ve	C-O(carboxylic)
		1108	-ve	C-O alcohol/ester
		3250	+ve	OH
		2920	+ve	-CH
		2858	+ve	-CH
PtPb				
	Internal			
		2343	-ve	CO_2
		1723	-ve	C=O
		1423	-ve	CHO
	External – PBS			
		2343	-ve	CO_2
		1740	-ve	C=O
		1623	-ve	H_2O
		1232	-ve	C-O carboxylic acid
		1566	+ve	RCO_2^-
		1407	+ve	RCO_2^-
	External- $HClO_4$			
		2343	-ve	CO_2
		1740	-ve	C=O
		1629	-ve	H_2O
		1400	-ve	CHO
		1235	-ve	C-O carboxylic
		1130	-ve	C-O

				alcohol/ester
		1119	-ve	C-O alcohol/ester
		875	-ve	
		3219	-ve	OH
		2915	+ve	-CH

Table 5.1: Identification of peaks in ATR-FTIR data

used up in the oxidation process. With the PtIr electrode, Figure 5.4C, there are negative going bands at 2343 cm^{-1} (400 mV), 2018 cm^{-1} (200 mV), 1737 cm^{-1} (200 mV), 1626 cm^{-1}(-200 mV), 1280 cm^{-1} (400 mV), and 1108 cm^{-1} (200 mV). Also, there are positive going bands at 3250 cm^{-1}, 2920 cm^{-1} and 2858 cm^{-1}. Finally the PtPb (Figure 5.5C) which displays negative going bands appearing at 2343 cm^{-1} (400 mV), 1740 cm^{-1} (0 mV), 1629 cm^{-1} (0 mV), 1400 cm^{-1} (200 mV), 1235 cm^{-1}, 1130 cm^{-1} (0 mV), 1119 cm^{-1} and 875 cm^{-1} (600 mV). Positive going bands appear at 3219 $cm^{-1}$and 2915 cm^{-1}.

5.6 Mechanistic Information

Using the ATR-FTIR data presented in Table 5.1, there are several points which can be drawn regarding the oxidation of glucose using the Pt-based nanomaterials. The IR results provide relevant information as to how each catalyst is performing in the oxidation of glucose.

The nanoporous Pt, having a lower current response than its counterparts, has acceptable performance as a potential glucose sensor. From the analysis of the surface during the oxidation, the main feature is the presence of a bipolar band at 2070/2040 cm^{-1} due to the formation of linearly bonded CO. At the same onset potential, a C=O band appears at 1740 cm^{-1}. There is also a negative going band at 3450 cm^{-1} due to water species being brought to the catalyst surface with increasing applied potential. A smaller negative going band at 1101 cm^{-1} corresponds to a C-O from alcohol or ether. This result indicates that CO is most likely being formed from an intermediate containing a carboxyl group. It has been reported in literature that one of the first intermediates in the oxidation of glucose is a five-member lactone ring[18]. This can then be oxidized with a C-C scissoring step to CO, which then can be oxidized with the assistance of a Pt-OH group, created from the increase of water at the catalyst surface.

From the analysis of the thin layer solution, common trends are observed in the spectra containing both $HClO_4$ and PBS. CO_2 appears at 400 mV, which corresponds well to the oxidation potential of CO adsorbed on a Pt surface. There is also an increase in the 1740 cm^{-1} band, as carboxyl containing intermediates desorb from the catalyst surface, most likely the 5-member lactone ring which appears at 0 mV. This band first appears at the surface at -400 mV, desorbtion occurs between -400 and 0 mV. A positive water band is representative of water being brought to the Pt surface to oxidize to the final CO_2 product. The positive going bands in the –C-H region indicate the oxidation of the glucose ring containing these groups. Finally, the bands at 1558 cm^{-1} and 1405 cm^{-1} are due to an RCO_2^- carboxylic acid, as both are the characteristic peaks of this group and appear simultaneously. With their positive orientation, less of this group is present in the thin layer solution. This group appears due to an intermediate formed at very low potential levels and is used up as the reaction proceeds.

The PtRu does not perform quite as well, as CO_2 is not observed at the surface of the catalyst. CO is formed, as well as two main intermediate bands at 2010cm^{-1} for CO_L, and 1817 cm^{-1}, arising from the 5 member lactone[19]. The solution analysis supports this, however, a CO_2 band is observed in the $HClO_4$ spectra at 400 mV but the CO_2 is not formed in sufficient amounts to be detected at the surface. A negative going band at 1725 cm^{-1} is observed as intermediates desorb from the surface. Two positive bands at 1564 cm^{-1} and 1403 cm^{-1} are again due to the initial RCO_2^- intermediate.

The PtIr has strong performance, as evidenced by the CO and CO_2 produced throughout the spectra. An increased amount of H_2O at the catalyst surface is also observed, this is expected of a PtIr catalyst as the Ir is utilized to produce water species to assist in the oxidation path. A negative going band at 1142 cm^{-1} is present due to the C-O stretch of a secondary

alcohol[20]. In the solution analysis, CO_2 first appears at 200 mV, an improvement over the Pt performance. However, there exists a band at 1995 cm^{-1} due a C=C=O group, as well as a band at 1740 cm^{-1} from a carbonyl containing intermediate (lactone). As with the PtRu, the 1564 cm^{-1} and 1400 cm^{-1} appear as positive bands due to the removal of RCO_2^- from the thin solution layer.

Finally, the PtPb was found as the best glucose oxidation catalyst with the following evidence. From the surface analysis, CO_2 is present at 600 mV, without any surface CO forming, a change from the previous three catalysts. Instead a negative going band at 1423 cm^{-1} appears and grows with increased potential until the appearance of CO_2 in the spectra. This band is due to a CHO methanol derivative[21], the reaction intermediate between the final intermediates before CO_2. The carbonyl containing intermediate is also visible at the surface, again most likely a five-membered lactone ring. In the solution analysis, CO_2, C=O species are observed and negative going, while positive peaks at 1566 and 1407 cm^{-1} are present, as with the PtIr and PtRu, due to the RCO_2^- initial intermediate. Other C-O intermediates from alcohol (1130 cm^{-1}) and carboxlyic acid (1232 cm^{-1}) also appear.

From the above we can see that: a) PtRu shows poor performance due to a low amount of CO_2 production in the oxidation of glucose, while PtRu stands as an effective catalyst in the oxidation of methanol and formic acid[16], the same is not true for glucose as one of the reaction intermediates serves to poison the surface; b) Nanoporous Pt can completely oxidize glucose through the production of a probable five-member lactone ring which is formed at the catalyst surface, then desorbs, where it can be further oxidized upon returning to the catalyst surface. Evidence of less –CH groups in the thin layer of solution is due to the glucose being oxidized completely to CO_2 ; c) PtIr, despite its strong electrochemical performance, exhibits a drawback

given the FTIR data: a large amount of CO formation at the catalyst surface which could potentially hinder its performance in the long term. The catalyst is functioning by using water to assist in complete oxidation. A large amount of species desorb from the surface, as evident by the solution analysis, such as the carbonyl group from the five member lactone which is joined by CHO from a $1995cm^{-1}$ band; d) PtPb has the highest performance, no surface CO is observed, however, the final product CO_2 is observed. The carbonyl, five member lactone, is observed at the surface as well as a CHO methanol derivative. The pathway changes from a CO containing pathway; to one in which the CO generation step is absent. The lack of CO will lead to eventual long term success of the catalyst; e) common intermediates such as alcohol, and carboxylic acids are observed, further analysis such as HPLC can used to further identify these; f) an initial intermediate formed in the $R_{(E1)}$ spectra at -600 mV is a RCO_2^- which desorbs from the catalyst surface.

5.7 Summary

In conclusion, analysis of the oxidation of glucose using Pt-based nanomaterials was performed using ATR-FTIR. Combined data from both the catalyst surface and solution close to surface was used to form initial mechanistic schemes for each catalyst. Pt, PtIr, PtRu, PtRuIr all display strong electrocatalytic activity towards the oxidation of glucose, however, in their oxidation pathways, CO is produced at low potentials, which must then be oxidized. PtPb shows strong electrochemical performance, as well as providing promising results from the spectroscopic data with no surface CO present. This is attributed to a different pathway for the oxidation of glucose on PtPb , illustrated through the study of the ATR-FTIR data, showing that the system can be used in the study of more complex oxidation processes than small organic molecules. Further study is required as this is an initial study in the understanding of the

complete oxidation of glucose. By studying the oxidation of several of the suggested intermediates we can clarify the mechanistic picture. However, practically, PtPb may not be the ideal sensor due to the metal toxicity of Pb. The search must continue to find the ideal catalyst for glucose chemical sensing. In the next chapter, the PtPb catalyst will be further investigated using the oxidation of several simple organic molecules, as well as investigation of PtPb and PtPd nanodendrites and their uses.

5.8 References

1. Wang, J. *Chemical Reviews* **2008**, 108, 814
2. Arnold, M.A.; Small, G.W. *Anal. Chem.* **2005**, 77, 5429.
3. Lee, J.; Park, S-M. *Analytica Chimica Acta*, **2005**, 545, 27.
4. Hrapovic, S., Luong, J.H.T. *Anal. Chem.* **2003**, 75, 3308.
5. Barone, P.W.; Parker, R.S.; Strano, M.S. *Anal. Chem.* **2005**, 77, 7556.
6. Park S.; Boo, H.; Ching, T.D. *Anal. Chim. Acta* **2006**, 556, 46
7. Clark Jr, L.C.; Lyons, C.; *N.Y. Acad. Sci.* 1962, 102, 29
8. Yuan, J.H.; Wang, K.; Xia, X. *Adv. Funct. Mater.* **2005**,15, 803.
9. Sakamoto, M.; Takamura, K. *Bioelectrochem. Bioenerg.* **1982**, 9, 571.
10. Kokkinidis, G.; Xonoglou, N. *Bioelectrochem. Bioenerg.* **1985**, 14, 375.
11. Wittstock, G.; Strubing, A.; Szargan, R.; Werner, G. *J. Electroanal. Chem.* **1998**, 444, 61.
12. X. Zhang, X.; Chan, K.-Y.; You, J.-K.; Lin, Z.-G.; Tseung, A.C.C. *J. Electroanal. Chem.* **1997**, 430, 147.
13. Holt-Hindle, P.; Nigro, S.; Asmussen, R.M.; Chen, A. *Electrochem. Commun.*, **2008**, 10, 1438
14. Wang, J.; Thomas, D.F.; Chen, A. *Anal. Chem.* **2008**, 8, 997
15. Li, L.H.; Zhang, W.D.; Ye, J.S. *Electroanal.* **2008**, 20, 2212
16. Koczkur, K.; Yi, Q.F.; Chen, A. *Adv. Mater.* **2007**, 19, 2648
17. Gong, H.; Sun, S.G.; Li, J.T.; Chen, Y.J.; Chen, S.P. *Electrochim. Acta* **2003,** 48, 2933

18. Zhang, X.; Chan, K.Y.; You, J.K.; Lin, Z.G.; Seung, C.C. *J. Electroanal. Chem.* **1997**, 430, 147
19. Bellamy, L. J., "The Infrared Spectra of Complex Molecules", 2nd edition, John Wiley & Sons, New York, **1961**.
20. Nakanishi, K. "Infrared Absorption spectroscopy - Practical", Holden-Day, Inc., San Francisco, **1962**.
21. Wieckowski, A. "Interfacial Electrochemistry: Theory, experiment and application" 1st edition, CRC, New York, **1999,** CH8, 885

Chapter 6

ATR-FTIR study of Pt-based nanodendrites

6.1 Introduction

Ranging from whale bones to the structure of leaves, dendrite and fractal structures are found throughout nature. At the nanoscale, these structures show promise in becoming potential nanosystems. Much work has been done in the synthesis of many simple nanostructured materials such as nanocrystal, nanowires and nanotubes[1-5], and there now exists a desire to fabricate more complex structures on the nanoscale. Dendritic and fractal structures are examples of this, and thus, are recognized as the most promising advanced building blocks. Dendrite structures have been previously fabricated for metals[6-8], metal oxides[9-10] and semiconductors[11-12], with only few examples of alloyed nanomaterials present as dendrites.[13-14]

Alloyed and intermetallic compounds have great importance due to their physical and chemical properties including superconductivity, shape-memory effects, catalytic activity, hydrogen storage, hardness, and corrosion resistance.[15] Precious metals, specifically Pt, have been researched for applications in fuel cell technology and development of chemical sensors and nanodevices.[16-20] To overcome some issues associated with the Pt catalysts such as high cost and inefficiency, intermetallic and alloyed catalyst can be used. These ordered intermetallic systems provide consistent control over structural, geometric and electronic features of the structures. In the study of nanoporous catalysts such as Pt, PtRu, PtIr, PtPd and PtPb, PtPb is able to outperform the other catalysts in the oxidation of formic acid.[21]

Nanodendrites also hold promise to serve as catalyst in eventual fuel cell applications. For these fuel cells, one of the prominent areas of focus is the direct methanol fuel cell (DMFC)

as methanol provides a high amount of energy per unit of fuel compared to hydrogen and is easily stored and distributed at ambient temperatures.[22] The catalyst in the DMFC was first proposed to be Pt. However, in the oxidation of methanol to the final product CO_2, several intermediates are produced which can poison the catalyst, specifically CO.[23-24] A significant amount of energy is required to electrochemical oxidize CO present at a catalyst surface using an activated water species[24]:

$$CO_{(ad)} + OH_{(ad)} \rightarrow CO_2 + H^+ + e^-$$

Along with the hindered performance due to intermediates, a second hurdle with the Pt catalyst is the high cost of a precious metal such as Pt. To overcome these hurdles, a second co-catalyst can be added to the Pt to both enhance its performance and lower the cost by lowering the total amount of Pt present. Much work has been done in this area with a wide range of co-catalysts such as Mo[25-26], Ru[27-30], Ir[31-32], Pb[33-34], Au[35-37], Bi[38-40], Os[41], and Pd.[42-46] Pd exists as an interesting metal catalyst on its own, as it shows activity towards simple fuels such as formic acid[47-49], and can be potentially used in the oxygen reduction reaction[50-53], an important reaction at the fuel cell cathode.

Research into a PtPd bimetallic catalyst has been done due to these potential gains at both catalysts, and there has been evidence of the effectiveness of PtPd towards methanol oxidation.[54-55] This study was performed to analyze the synthesized PtPd nanodendrites as effective catalysts in the oxidation of methanol, a potential fuel source. These novel bimetallic dendrites hold promise as an initial step in the development of advanced nanostructured materials for eventual use in nanoscaled systems. Our previous report[13] displayed the performance of nanodendrites in the oxidation of formic acid, and we now show the performance of nanodendrites in a more

complex system, the oxidation of methanol. The electrochemical and structural information will be combined with reaction data from the catalyst surface, collected using ATR-FTIR. Fourier transform infrared spectroscopy is a powerful analytical tool due to its rapid acquisition time and high sensitivity.[56] The attenuated total reflection mode of FTIR allows for *in-situ* monitoring of reactions at a catalyst surface by removing interference from the bulk electrolytic solution. We utilize this technique to study the oxidation of methanol at the PtPd surface to gather useful information towards understanding the nature of any performance enhancement observed. This chapter will first discuss the performance of PtPb nanodendrites in the oxidation of formic acid to show the strength of the system in testing complex nanosystems. Following this, the performance of PtPd nanodendrites in the oxidation of methanol, both studied using ATR-FTIR.

6.2 PtPb Nanodendrites

6.2.1 Characterization of PtPb Nanodendrites

Figure 7.1 displays the SEM images of the PtPb nanodendrites. Figure 6.1 A) shows nanoporous Pt lacking any dendritic features. However, Figure 6.1B) is PtPb 97.5:2.5 with such a small addition of Pb, dendritic features are observed. The dendrites become less ordered as the concentration of Pb is increased as can been seen in Figure 6.1C) PtPb 95:5 and 1D) PtPb 80:20 and 1E) PtPb 50:50. Figure 6.1F) shows the EDS spectra of the PtPb samples, confirming the presence of Pt and Pb in the nanodendrite structures.

The XRD patterns of the PtPb dendrites show interesting information.[13] Initially the PtPb structures show peaks standard to a face-centred cubic crystal structure. However, with a Pb concentration about 25% these peaks are joined by a new set of diffraction patterns, which grow with increased Pb levels. These peaks are due to hexagonal structure of NiAs crystal for the

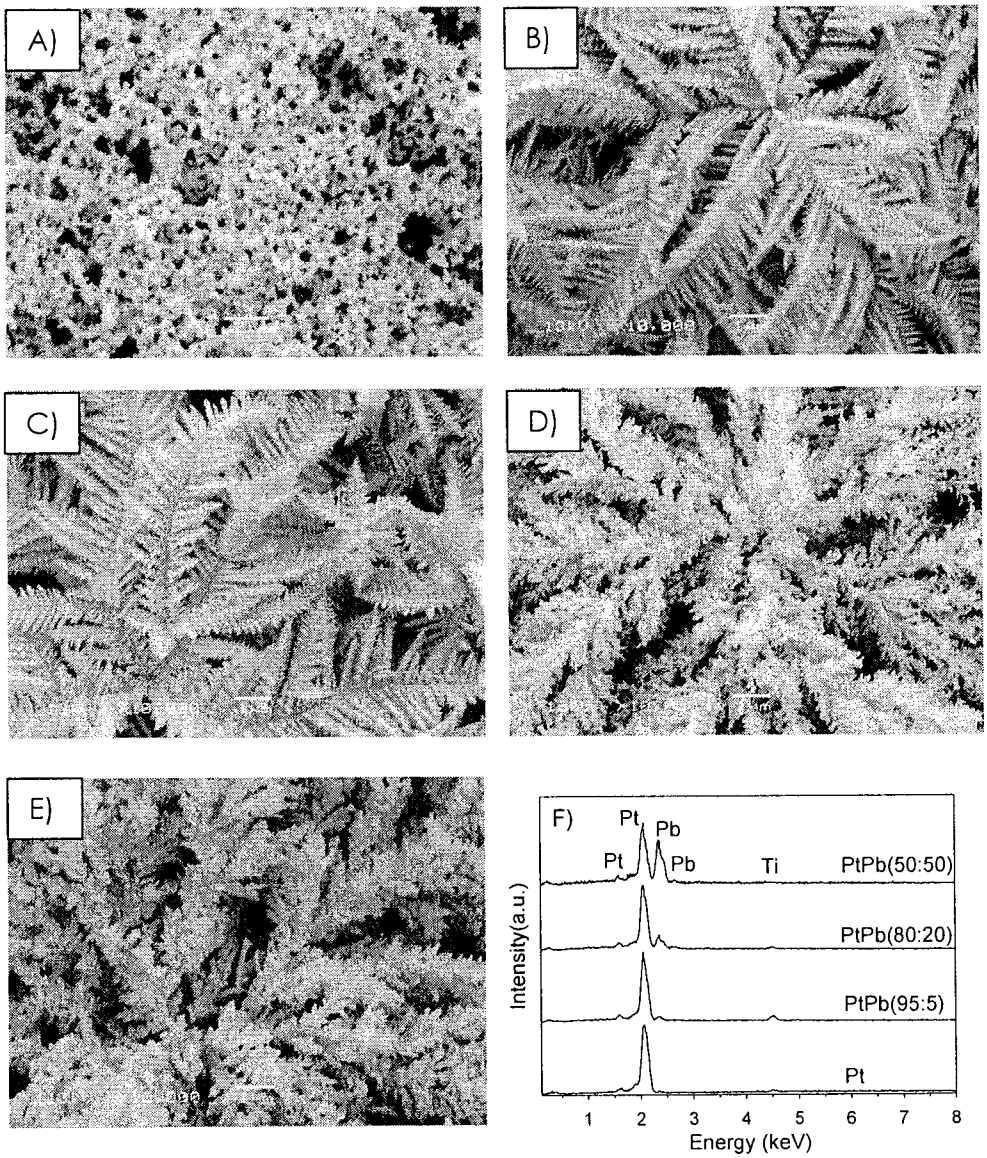

Figure 6.1 SEM images of the as-synthesized A) Pt, B) PtPb 97.5:2.5, C) PtPb 95:5, D) PtPb 80:20, E) PtPb 50:50 displaying dendrite structures. F) EDS spectra of the dendrite structures confirming the presence of Pt and Pd

PtPb. This phase conversion is essential in the electrochemical performance of the PtPb nanodendrites.

6.2.2 Electrochemical Oxidation of Formic Acid

Due to its strong performance as a nanoporous network, the oxidation of formic acid was employed as the test reaction for the performance of the PtPb nanodendrites. The scanning cyclic voltammograms of the synthesized PtPb dendrites in formic acid are presented in Figure 6.2. As the level of Pb is increased, there is a large increase in activity in the low potential regions of -100 mV to 500 mV. The increase in performance up to 5% Pb can be attributed to the lattice dilation as Pb atoms are incorporated in the Pt structure. This can prevent CO, which is produced from adsorbing in the three-fold or hollow Pt sites. This is occurring as the formic acid is oxidized via the dehydration pathway.

With Pb levels between 10-50%, this effect is also apparent as there exists an increased current density and lower onset potentials compared to the other Pt particles. To clarify this assumption, three of the PtPb catalysts were tested for formic acid oxidation using ATR-FTIR spectroscopy.

6.2.3 ATR-FTIR spectroscopy study of PtPb nanodendrites

Figure 6.3A displays the oxidation of formic acid on the PtPb 95:5, with the main feature being the large bipolar band centred at 2065 cm^{-1}, due to potential dependent absorption of linearly bonded CO at the catalyst surface. One feature of note from this band is the negative lobe of the bipolar band is independent of applied potential as its presence is due to the CO at the surface at the base potential of -200 mV; whereas the positive lobe shifts to higher potentials until 600 mV at which point it disappears as the surface CO is oxidized. At 1805 cm^{-1}, there

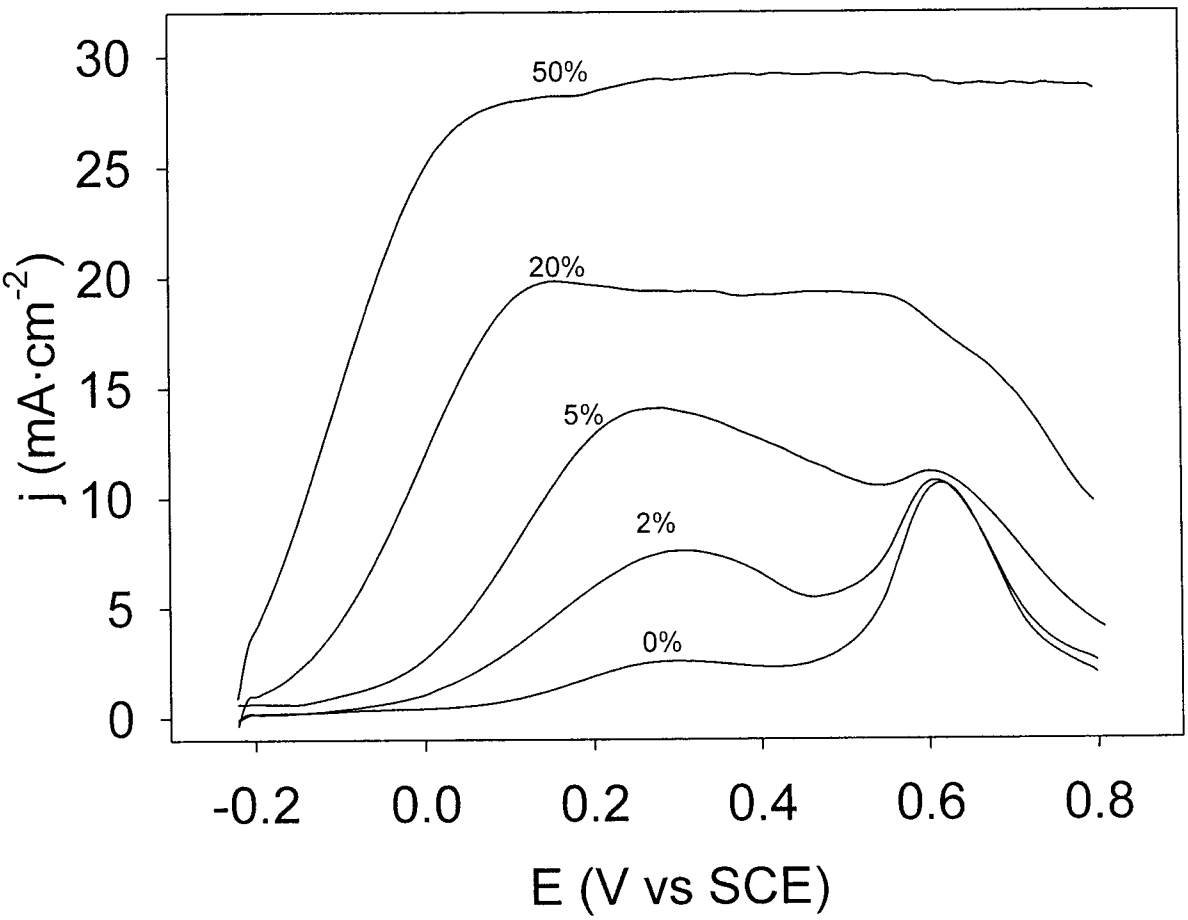

Figure 6.2: Cyclic voltammograms of the PtPb nanodendrites in 0.1 M HCOOH + 0.1 M H_2SO_4 with a scan rate of 20 mV/s

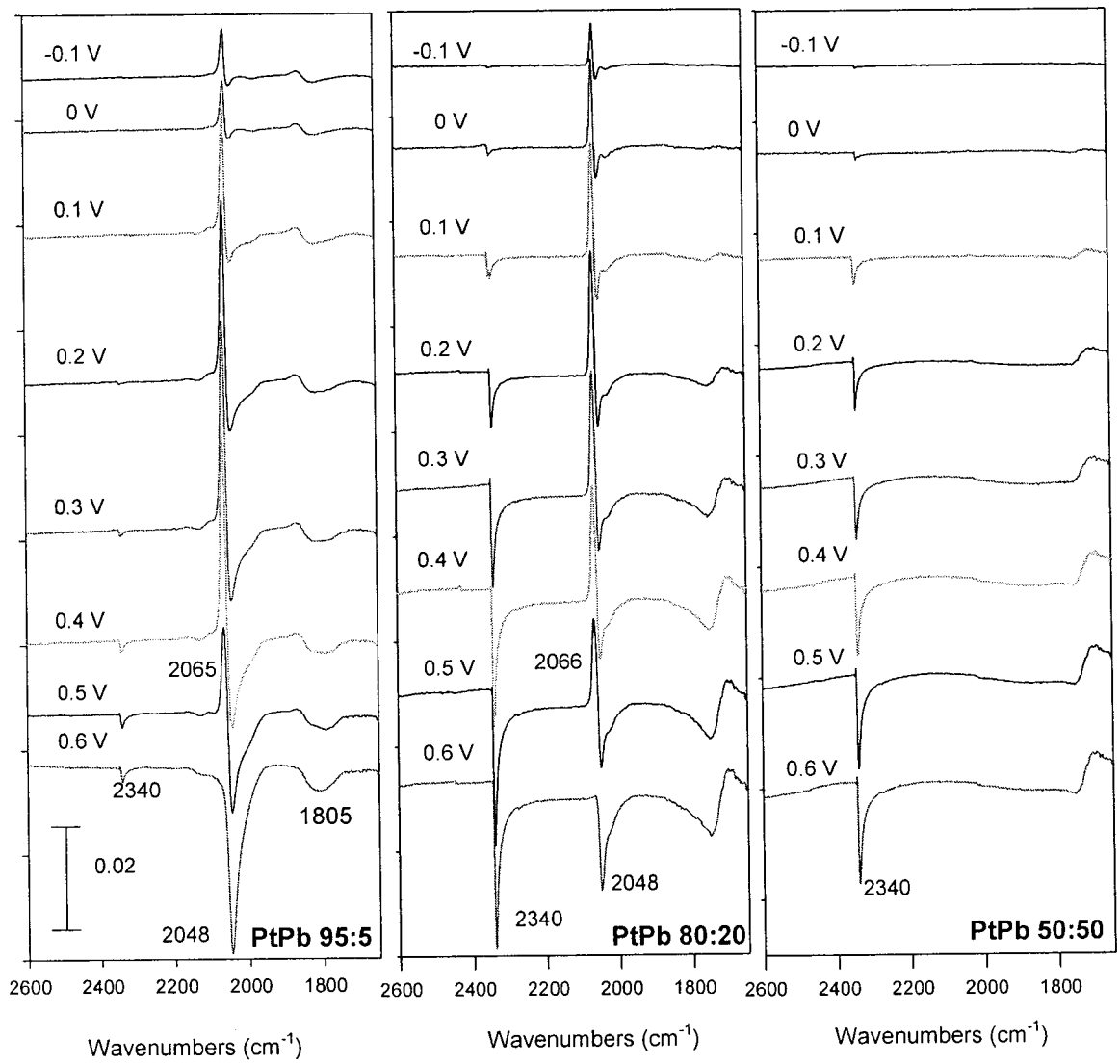

Figure 6.3 ATR-FTIR spectra using a) PtPb 95:5, b) PtPb 80:20, c) PtPb 50:50 for the oxidation of 0.1 M HCOOH + 0.1 M H_2SO_4 with $R_{(E1)}$ set to -200 mV

exists a band due to bridged CO at the catalyst surface. Once the surface CO is oxidized, CO_2 is produced and this appears in the spectra as a band at 2340 cm^{-1}, beginning at 300 mV. This corresponds to the increase in current density seen in the CV in Figure 6.2 for nanoporous Pt and PtPb 95:5. The dehydration pathway is occurring with the addition of 5% Pb from this spectroscopic evidence; i) intensity of CO_L peak, ii) no CO oxidation below 200 mV. Figure 6.3B is the oxidation of formic acid using PtPb 80:20, the threshold of the conversion of the dendrites to the hexagonal phase. The linearly bonded CO is still present as a prominent bipolar band, however the CO_2 band now appears at -100 mV, and until 300 mV grows in intensity along with the CO_L band. Above 300 mV, the intensity of the CO_L band decreases with a growth of the intensity of the CO_2 band. A new series of bands appears at 1720 cm^{-1}, due to the stretching mode of C=O in $-COOH_{ads}$[57]. The CO_B band is no longer present in the spectral series. The presence of both a CO_L band and $-COOH_{ads}$ band shows that the oxidation of formic acid by the dendrites is occurring by both the dehydration and dehydrogenation pathways. The absence of the CO_B band can be attributed to the lattice dilation through incorporation of 20% Pd.

Finally Figure 6.3C for the PtPb 50:50 nanodendrites shows visible evidence as to why the strongest electrochemical performance comes from this catalyst. No inverted bipolar band can be observed for CO_L while the CO_2 negative going band at 2340 cm^{-1} is present at -100 mV and all subsequent spectra. The C=O band at 1720 cm^{-1} has a bipolar feature and is present from 0mV until 600 mV and grows in intensity simultaneously with the CO_2 band. This explains that the CO_2 is being formed directly from the $-COOH_{ads}$ through the dehydrogenation pathway. This tells us that the PtPb 50:50 catalyst is able to catalyze the oxidation of formic acid to CO_2 solely through the dehydrogenation pathway, by completely preventing CO from adsorbing to

the catalyst surface. Next, a study on PtPd nanodendrites for the oxidation of methanol is presented.

6.3 PtPd nanodendrites

6.3.1 Characterization of PtPd Nanodendrites

Figure 6.4 displays the SEM images of the as-synthesized PtPd nanodendrites. Figure 6.4A shows 100% Pt, which displays no sign of dendritic features as the presence of secondary atoms is the root cause of growth. Figure 6.4B displays Pt:Pd 72:25 in which clear dendrites also appear, the same holds true for the Pt:Pd 50:50 structure (6.4C). The dendrites become less ordered as the amount of Pd is increased, this is apparent in the image of the Pt:Pd 25:75 as can be seen in Figure 6.4D. Figure 6.4E displays 100% Pd particles which are nanoporous, losing the dendritic feature with the absence of the second catalyst as a foreign particle induced growth mechanism is responsible for the creation of the dendrite structure.[13] The composition of these samples was confirmed using EDS, and the resulting spectra can be seen in Figure 6.4F. Herein we observe distinct Pt and Pd peaks for the various Pt:Pd dendrites. The dendrites achieved the desired catalyst compositions based on the precursor solutions used, the five samples are Pt 100, Pt:Pd 75:25, Pt:Pd 50:50, Pt:Pd 25:75, Pd 100.

Figure 6.5 presents the XRD patterns of our PtPd nanodendrites supported on a Ti substrate for (a) Pt, (b) PtPd 75:25, (c) PtPd 50:50, (d) PtPd 25:75, (e) Pd. There is no evident change in the phase of the catalysts from the conversion from nanoporous to dendrite structure as all have face-centered characteristic (fcc) with all displaying the (111), (200), (220) and (311) refraction characteristics. Negative shifts in 2θ values are observed, corresponding to the decreased d-spacing and lattice constants with increasing amounts of Pd.

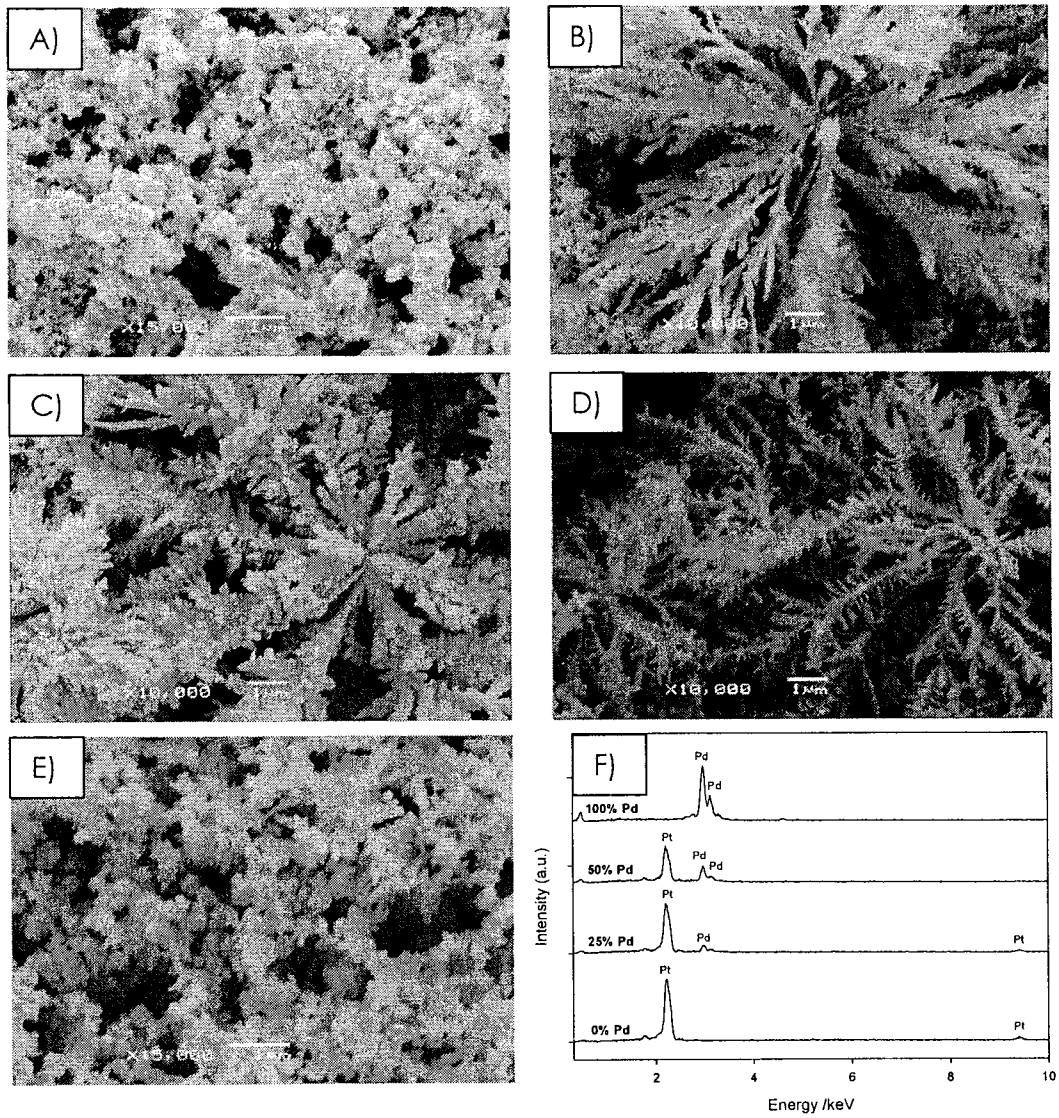

Figure 6.4 : SEM images of a) Pt 100 lacking dendrite features, b) PtPd 75:25, c) PtPd 50:50, d) PtPd 25:75, e) Pd 100 again lacking the dendrite features. f) EDS spectra of the catalysts showing the presence of both the Pt and Pd

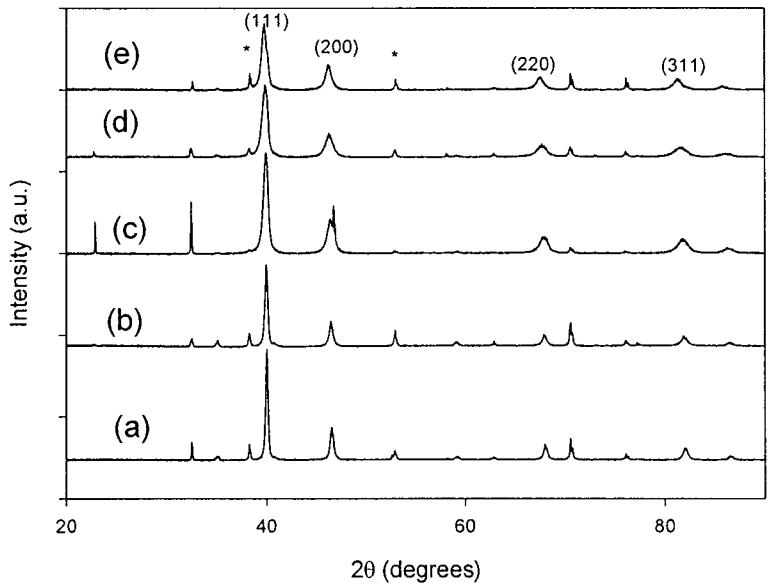

Figure 6.5 XRD spectra for the as-synthesized PtPd dendrites systems on a Ti substrate a) Pt, b) PtPd 75:25, c) PtPd 50:50, d) PtPd 25:75, e) Pd (* indicates Ti from substrate)

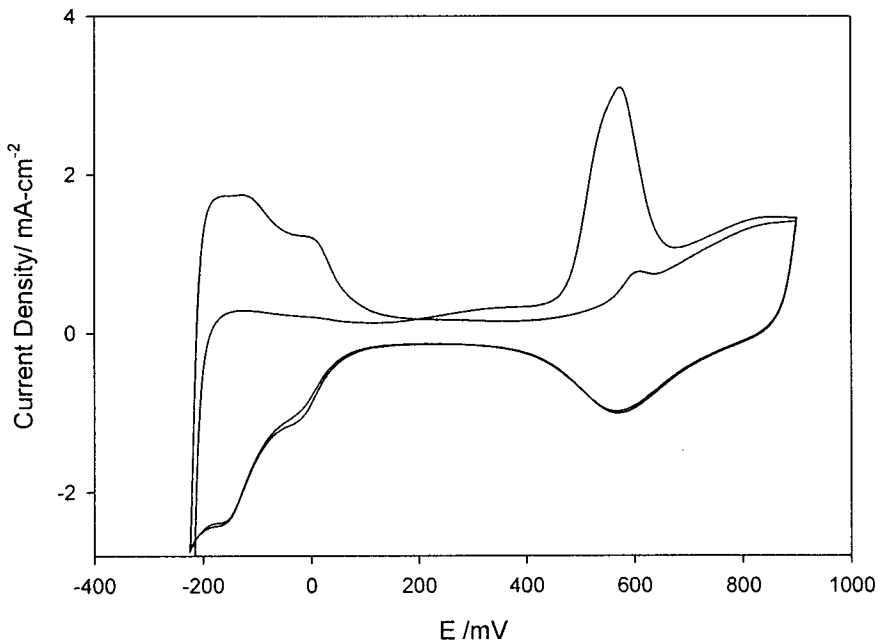

Figure 6.6 CO stripping curve in 0.5 M H_2SO_4 for the PtPd 50:50 nanodendrites at 20 mV/s. The electroactive surface area was calculated from the area underneath the CO oxidation peak in the first scan.

6.3.2 Electrochemical Oxidation of Methanol Using PtPd Nanodendrites.

The first test of the electrochemical performance of the PtPd nanodendrites was performed using a CO stripping experiment to garner a measure of the electroactive surface area of each catalyst. A layer of CO was formed on the catalyst surface at a potential of -100mV, followed by a potential sweep from low (-225 mV) to high (900 mV). The resulting CO stripping curve from the PtPd 50:50 nanodendrite catalyst can be seen in Figure 6.6. A band appears at 310 mV reaching its peak at 565 mV due to the oxidation of the surface CO. In the return scan, this feature is absent due to complete oxidation of the CO. Integration of the area under the CO oxidation band is a method of determining the electroactive surface area of the catalyst.[59] The resulting charges and electroactive surface areas, assuming a charge of 420 $\mu C\text{-}cm^{-2}$ for the process, are listed in Table 6.1.

Catalyst	Charge /mC	Electroactive Surface Area /cm^2
Pt	43.9	104.0
PtPd 75:25	49.8	118.5
PtPd 50:50	47.3	112.6
PtPd 25:75	46.1	109.8
Pd	41.4	98.6

Table 6.1: Listing of the charge and electroactive surface area for each of the five samples calculated through integration of the CO oxidation peak from Figure 3.

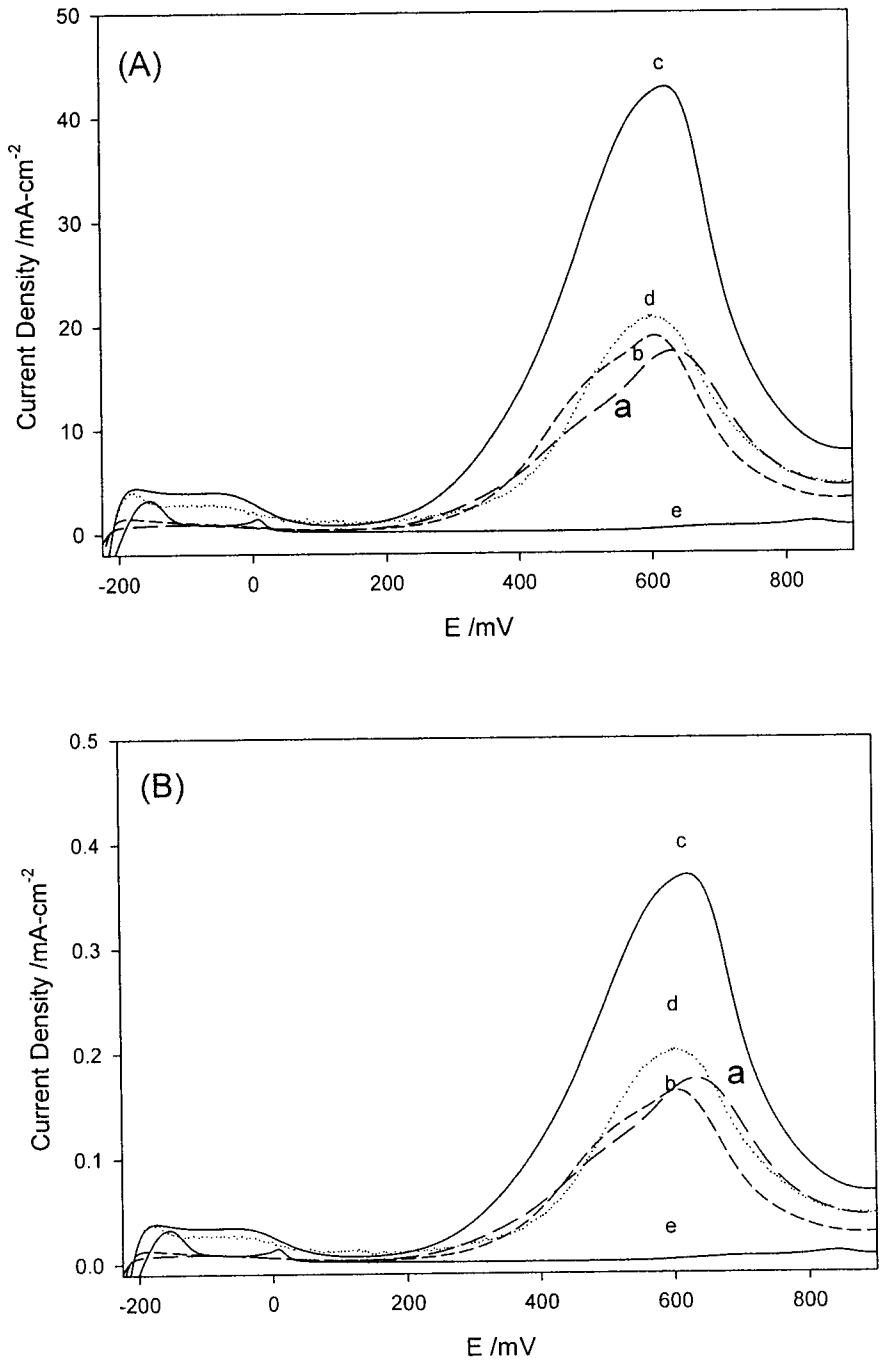

Figure 6.7: MeOH oxidation using the PtPd nanodendrites at 20 mV/s A) 0.1M MeOH + 0.1M H_2SO_4 at 20 mV/s B) Corrected for the electroactive surface areas found from CO stripping in Figure 6.6 for a)Pt(long dash), b) PtPd(short dash) 75:25. c) PtPd 50:50, d) PtPd 25:75 (dot), e)Pd

The nanodendrite catalyst performance was tested using the oxidation of methanol. Nanoporous Pt has shown improved performance in the oxidation of methanol over polycrystalline Pt. With the addition of Pd to the Pt catalyst, an improvement can be seen. Figure 6.7A presents the oxidation of methanol using the catalysts, displaying only the forward sweeps for clarity. Nanoporous Pt (a) shows an onset potential of 300 mV for the oxidation of methanol, whereas the nanoporous Pd (e), shows little sign of electroactivity towards the oxidation of methanol. The addition of Pt (25%) to the pure Pd catalyst does improve the electroactivity, giving a maximum current production of 22mA, slightly above the performance of Pt(17mA) and PtPd 75:25(18.5mA). The PtPd 50:50 nanodendrites greatly outperform all other four catalysts, giving a peak current of 43mA at 600 mV. The onset potential from the PtPd nanodendrites is also lowered by 100 mV to a potential of 200 mV. To gain a correct measure of the performance of the catalysts, the methanol oxidation curves are corrected for the electroactive surface areas. In doing so, the performance can be balanced, and any improvement is due to the composition alone. Figure 6.7B displays the methanol oxidation curves corrected for electroactive surface area, and the PtPd 50:50 nanodendrites still remain as top performing.

Figure 6.8 presents the chronoamperometric behaviour of the 100% (a)Pt and (e)Pd catalysts and (b)PtPd 75:25, (c)50:50, and (d)25:75 nanodendrites at the onset and peak potential of methanol oxidation at (A)300 mV and (B)600 mV respectively. Over the span of five minutes, the PtPd 50:50 (c) provides the highest current at both potentials, representative of its excellent performance compared to the PtPd 75:25, 25:75. Its equilibrium current reached is 1.9 mA at 300 mV compared with 1.5 mA to 0.03 mA for the other catalysts. With 600 mV applied,29.3 mA is achieved by the (c) PtPd 50:50, compared with a peak of (a)14.7 mA, (b) 13.25 mA, (d)11.81 mA and (e)0.72 mA for the others dendrites and pure nanoporous catalysts.

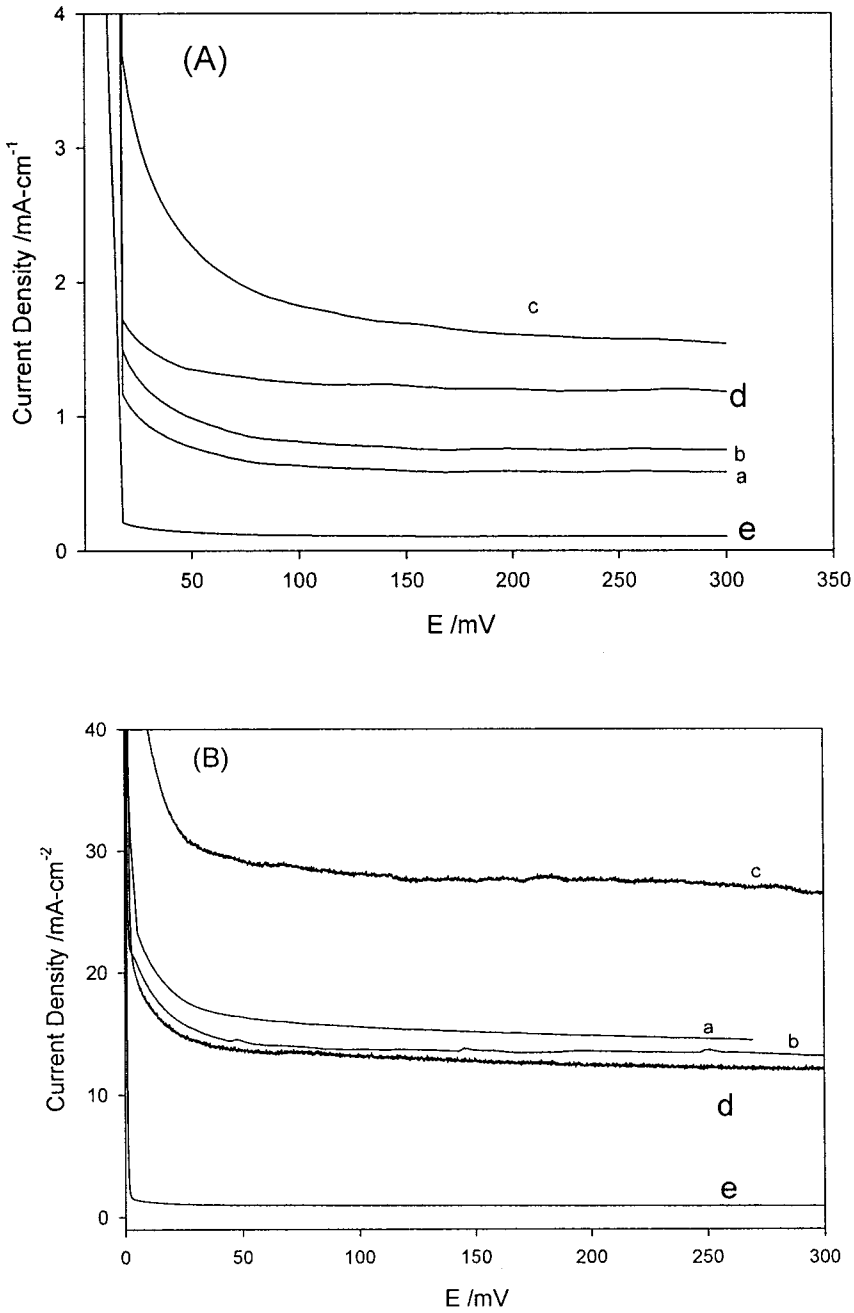

Figure 6.8 CA curves of the a) Pt, b) PtPd 75:25, c) PtPd 50:50, d) PtPd 25:75, e)Pd nanodendrites in 0.1M MeOH + 0.1 M H_2SO_4 at A) 300 mV and B) 600 mV

While there exist no structural change between the nanodendrites, and the surface areas are similar to one another, an explanation to the increased performance is not clear. ATR-FTIR spectroscopy can be utilized to provide insight into the increased performance from the catalysts.

6.3.3 ATR-FTIR analysis of PtPd nanodendrites

To study the behaviour of the catalysts at their surface during the oxidation of methanol, ATR-FTIR spectroscopy can be employed. Figure 6.9 shows analysis data collected at the surface of the Pt, Pd and PtPd catalysts during the oxidation of methanol. A base spectrum, $R_{(E1)}$, was collected at -200mV where very little is occurring at the surface of the electrode. Upon stepping the potential up in 100mV increments the presented spectra are produced. In the oxidation of methanol using the(a) Pt (b) PtPd 72:25 (c) 50:50 (d) 25:75 (e) Pd very similar traits are observed. CO_2 can be observed at 2343 cm^{-1} starting at 500 mV for the (b) PtPd 75:25 and (c) 50:50. However in this set-up CO_2 is only observed when created in large amounts, as it is free to desorb form the catalyst surface and return to the bulk solution. A large bipolar peak at ~2060/1950 cm^{-1} due to linear bonded CO (CO_L) can be seen in the (a-d) spectra, but not for (e)Pd. At 1863 cm^{-1} bridged CO (CO_B) can be seen in the (b) 75:25 and (c) 50:50 spectra as well as the (a)100% Pt, having a positive going feature. Both of these bands hold true to the abnormal behaviour of CO at a metal surface.[60]

The position of the CO bipolar band is of interest in this study. In the bipolar band, the negative going lobe is due to the CO at the surface at the low potential, $R_{(E1)}$, and remains constant in all spectra. The positive going lobe shifts to lower frequencies as the applied potential is increased, due to decreased strength of the M-CO bond. The Pd-CO frequency is at a lower value than Pt-CO.[56] As the level of Pd in the dendrite structure increases, the negative

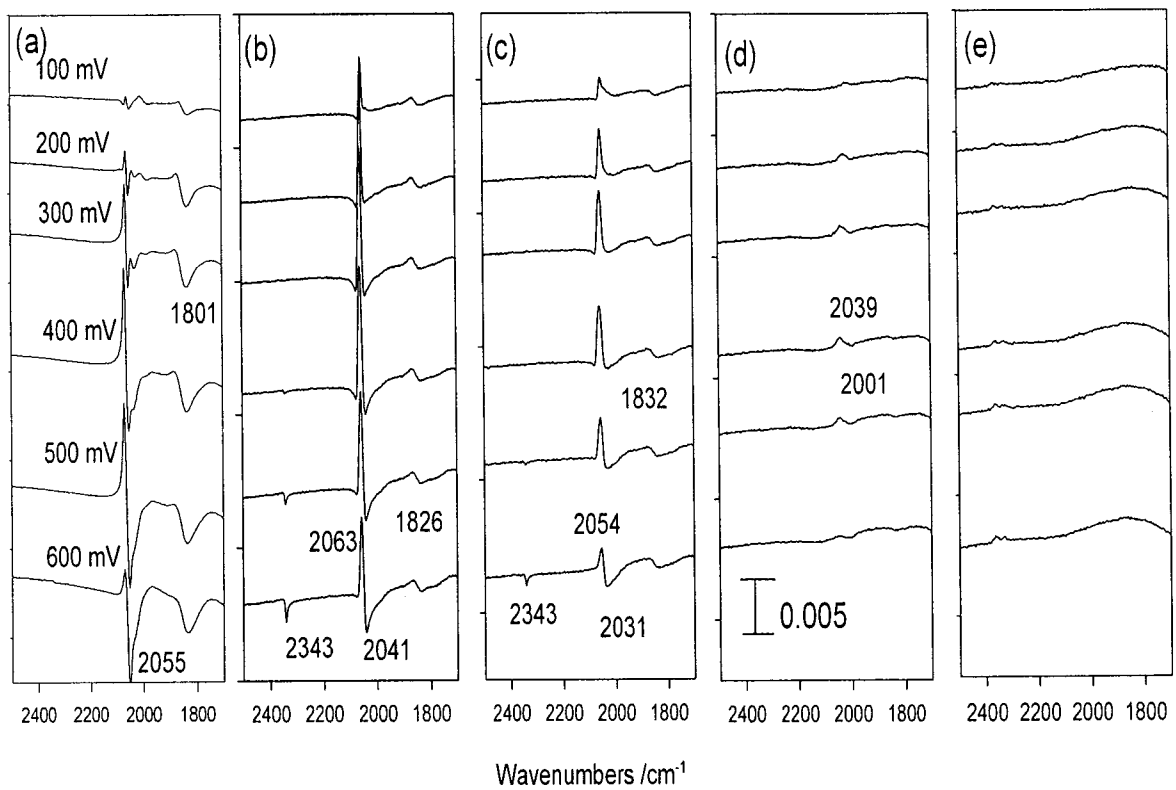

Figure 6.9 ATR-FTIR spectra collected with $R_{(E1)}$=-200 mV in 0.1M CH_3OH + 0.1M H_2SO_4 for a) Pt, b) PtPd 75:25, c) PtPd 50:50, d) PtPd 25:75, e) Pd.

going lobe of the CO bipolar band shifts to a lower frequency, the CO which is formed, from a formate intermediate is occurring near the Pd sites, instead of Pt leading to increases performance as poisoning from the Pt-CO species is reduced.

The second ATR-FTIR system set-up allows us to monitor species as they become desorbed from the catalyst's surface and become trapped in the thin solution layer. The spectra collected in this manner are presented in Figure 6.10. Here we see evidence of the oxidation mechanism occurring at the PtPd catalysts. A positive going band at 3350 cm^{-1} and 1640 cm^{-1} are due to water being used up in the thin layer to assist in the oxidation of methanol confirming a dehydration mechanism. Also, the appearance of a negative going band at 2343 cm^{-1} is due to the complete oxidation of methanol to CO_2. This is clear evidence as the onset of CO_2 production and level of methanol oxidation as all created CO_2 is visible, compared to Figure 6.9 in which it is free to re-enter the bulk solution. This CO_2 band can be used to garner a measure of the overall performance of the catalyst, as CO_2 is the final product in the oxidation process. This band first appears in the (a) Pt spectra at 400 mV, (b) PtPd 75:25 at 300 mV, (c) PtPd 50:50 100 mV, and (d) PtPd 25:75 at 300 mV. In (e) Pd, there exists no CO_2 band as the Pd does not function well in the oxidation of methanol. This shows that the PtPd nanodendrites lower the onset potential for methanol oxidation compared to Pt, with PtPd 50:50 having the lowest onset at 100 mV. The intensity of the CO_2 band can also be used as a representation of the efficiency of the catalyst. The plot of intensity of the CO_2 band vs. applied potential is presented in Figure 6.11. Here, the largest intensity is observed for the PtPd 50:50, thus making it the most powerful nanodendrite catalyst as it oxidizes a larger amount of total methanol to CO_2 at each potential level than its counterparts.

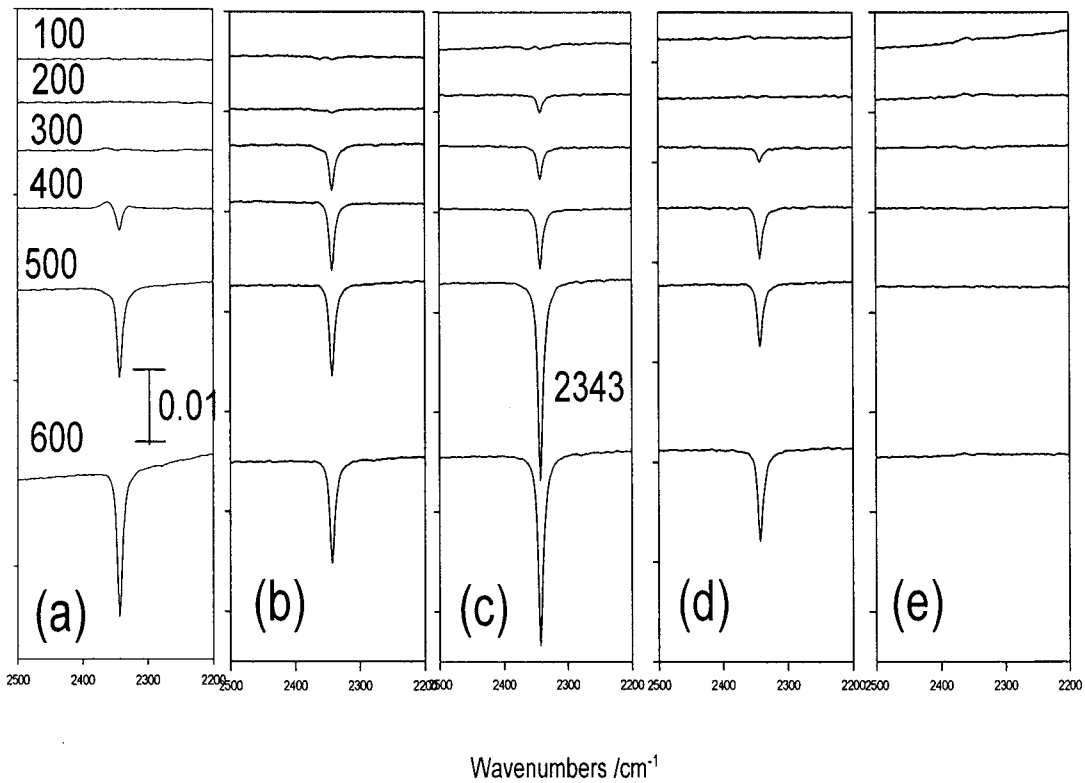

Figure 6.10: ATR-FTIR spectra collected using the second ATR configuration analyzing a thin layer of solution in 0.1M MeOH + 0.1M H_2SO_4 for a)Pt, b) PtPd 75:25, c) PtPd 50:50, d) PtPd 25:75 e) Pd

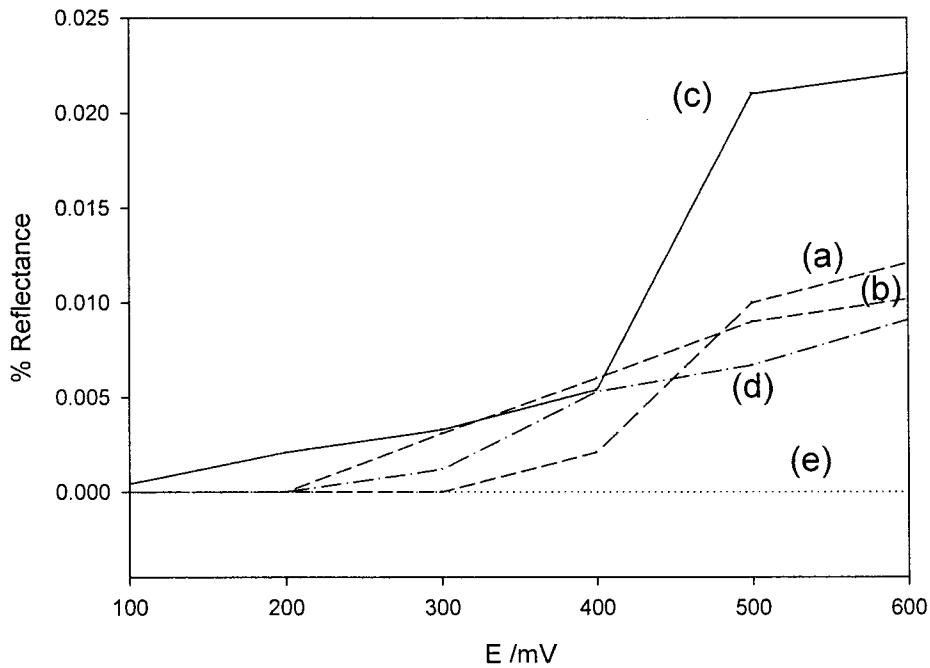

Figure 6.11 Analysis of the intensity of the CO_2 band appearing in Figure 7 for a) Pt (long dash line) b) PtPd 75:25 (short dotted line) c) PtPd 50:50 (solid line) d) PtPd 25:75 (dash dot dash) e)Pd

From the ATR-FTIR spectra we are able to learn more about the performance of these PtPd nanodendrites. Five main traits are observed in this study; i) A low level of CO is observed at the PtPd 50:50 surface while CO_2 appears as well, ii) the position of the CO band shifts to a lower frequency with increased Pd composition in the dendrites, thus leading to the CO being formed near the Pd sites in the catalyst, iii) CO_2, the final product of methanol oxidation is observed at a lower potential (100 mV) for the PtPd 50:50 than the other catalysts, iv) the PtPd 50:50 generates the largest amount of CO_2 at the higher potential levels than its counterparts, making it the most efficient catalyst. It is apparent that Pd has limited activity towards the oxidation of methanol, however becomes active with the addition of Pt to the catalyst, whereas the activity of Pt is increased due to the presence of Pd. It is a 50:50 composition of this catalyst which shows the highest performance towards the oxidation of methanol. Therefore it is thought to be a synergistic effect between the two metals.

6.4 Summary

This chapter presented work done on Pt-based nanodendrite systems, both PtPb and PtPd, synthesized from the hydrothermal technique. The PtPb nanodendrites undergo a phase transition from the face-centred-cubic phase to a hexagonal phase, and it is this transformation that creates an increase in activity towards the oxidation of formic acid. As the amount of Pb in the network is increased, the activity towards formic acid increases as well. ATR-FTIR spectroscopy was employed to learn that this improvement is due to the inability of CO to adsorb to the catalyst surface after the phase change occurs. This is also apparent with the oxidation of methanol and CO with PtPb. As for the PtPd nanodendrites, they show strong performance towards the oxidation of methanol. A synergistic mechanism is observed using ATR-FTIR with

the PtPd 50:50 nanodendrites having the strongest performance. These two nanodendrites represent first steps towards the use of more complex nanostructures in the development of nanosystems. The following chapter will examine the durability of the two FTIR systems as they will be employed to study photochemical degradation and electrochemical oxidation of nitrophenol compounds, based off of the development of novel bifunctional electrodes.

6.5 References

1. Burda, C.; Chen, X.; Narayanan, R.; El-Sayed, M. A. *Chem. Re*V. **2005**, 105, 1025
2. Patzke, G. R.; Krumeich, F.; Nesper, R. *Angew. Chem., Int. Ed.* **2002**, 41, 2446
3. Sun, S.; Murray, C. B.; Weller, D.; Folks, L.; Moser, A. *Science* **2000**, 287, 1989
4. Glotzer, S. C.; Solomon, M. J. *Nat. Mater.* **2007**, *6*, 557
5. Murphy, C. J. *Science* **2002**, *298*, 2139
6. Nakanishi, S.; Fukami, K.; Tada, T.; Nakato, Y. *J. Am. Chem. Soc.*, **2004**, 126, 9556
7. Xiao, J.; Xie, Y.; Tang, R.; Chen, M.; Tian, X. *Adv. Mater.*, **2001**, 13, 1887
8. Ye, J.; Chen, Q.W.; Qi, H.P.; Tao, N. *Crest. Growth Des*, **2008**, 8, 2464
9. Cao, M.; Liu, T.; Gao, S.; Sun, G.; Wu, X.; Hu, C.; Wang, Z.L.; *Agnew Chem.*, **2005,** 117, 4269
10. Balakrishnan, S.; Gun'ko, Y. K.; Perova, T.S.; Moore, R. A.; Venkatesan, M.; Douvalis, A.P.; Bourke, P. *Small,* **2006**, 2, 864
11. Sukhanova, A.; Baranov, A. V.; Perova, T. S.; Cohen, J. H. M.; Nabiev,I. *Angew. Chem., Int. Ed.* **2006**, 45, 2048
12. Li, G.-R.; Yao, C.-Z.; Lu, X.-H.; Zheng, F.-L.; Feng, Z.-P.; Yu, X.-L.; Su, C.-Y.; Tong, Y.-X. *Chem. Mater.* **2008**, 20, 3306
13. Wang, J.; Asmussen, R.M.; Adams, B.; Thomas, D.F.; Chen, *A. Chem. Mater,* **2009**, 21, 1716
14. Wang, J.; Thomas, D.F.; Chen, A. *Chem. Commun.* **2008** 5010
15. Ferrando, R.; Jellinek, J.; Johnston, R. L. *Chem. Re*V. **2008**, 108, 845

16. Bock, C.; Paquet, C.; Couillard, M.; Botton, G. A.; MacDougall, B. R. *J. Am. Chem. Soc.* **2004**, 126, 8028
17. Wang, J.; Thomas, D. F.; Chen, A. *Anal. Chem.* **2008**, 80, 997
18. Koczkur, K.; Yi, Q.; Chen, A. *AdV. Mater.* **2007**, 19, 2648
19. Teng, X.; Maksimuk, S.; Frommer, S.; Yang, H. *Chem. Mater.* **2007**,19, 36
20. Babu, P. K.; Kim, H. S.; Oldfield, E.; Wieckowski, A. *J. Phys. Chem.B* **2003**, 107, 7595.
21. . Wang, J.; Holt-Hindle, P.; MacDonald, D.; Thomas D.F.; Chen, A. *Electrochimica Acta* **2008**, 53, 6944
22. Liu, H.; Zhang, L.; Zhang, J.; Wang, H.; Wilkinson, D.P. *J. of Power Sources* **2006,** 155, 95
23. Jiang, R.; Chu, D. *J. of Power Sources* **2006,** 161, 1192
24. Yajima, T.; Uchida, H.; Watanabe, M. *J. Phys. Chem. B.* **2004**, 108, 2654
25. Wu, Y.M.; Li, W.S.; Lu, D.S.; Fu, J.M. *J. of Power Sources* **2005,** 145, 286
26. Martinez-Huerta, M.V.; Rodriguez, J.L.; Tsiouvaras, N.; Pena, M.A.; Pierro, J.L.G.; Pastor E. *Chem. Mater.* **2008**, 20, 4249
27. Bock, C.; Paquet, C.; Couillard, M.; Botton, G.A.; MacDougall, B.R. *J. Am. Chem. Soc.* **2004,** 126, 8028
28. Lin, W.F.; Iwasita, T.; Vielstich, W. *J. Phys. Chem. B* **1999,** 103, 3250
29. Gojkovic, S.L.; Vidakovic, T.R.; Durovic, D.R. *Electrochoim. Acta.* **2003,** 48, 3607
30. Peng, X.; Koczkur, K.; Chen, A. *Nanotech.* **2007,** 18, 561
31. Holt-Hindle, P.; Nigro, S.; Asmussen M.; Chen, A. *Electrochem. Commun.* **2008,** 10, 1438
32. Chen, A.; La Russa D.J.; Miller, B. *Langmuir* **2004,** 20, 9695
33. Basnayake, R.; Li, Z.; Lakshmi, S.; Zhou, W.; Smotkin, E.S.; Casadonte, D.J.; Korzeniewski, C. *Langmuir* **2006**, 22, 10446
34. Ghosh, T.; Matsumoto, F.; McInnis, J.; Weiss, M.; Abruna, H.D.; DiSalvo, F.J. *Nanopart. Res.*, **2009,** 11, 965
35. Choi, J.H.; Jeong, K.J.; Dong, Y.; Han, J.; Lim, T.H.; Lee, J.S.; Sung, Y.E. *J. Power. Source*, **2006**, 162, 71
36. Choi, J.H.; Park, K.W.; Park, I.S.; Kim, K.; Lee, J.S, Sung, Y.E. *J. Electrochem. Soc.*, **2006**, 153, A1812

37. Jin, C.C.; Song, Y.S.; Chen, Z.D. *Electrohim. Acta,* **2009**, 54, 4136

38. Tripkovic, A.V.; Popovic, K.D.; Stevanovic, R.M.; Socha, R. Kowal, A.; *Electrochem. Commun.*, **2006**, 8, 1492

39. Zhang, L.J.; Xia, D.G.; Wang, Z.Y.; Yuan, R.; Wu, Z.Y. *Acta.-Phys. Chim. Sin.* **2005**, 21, 287

40. Zhang, L.J.; Xia, D.G. *Chin. J. Inorg. Chem.* **2006**, 22, 1085

41. Moore, J.T.; Chu, D.; Jiang, R.; Deluga, G.A.; Lukehart, C.M. *Chem. Mater.*, **2003**, 15, 1119

42. Li, H.; Sun, G.; Li, N.; Sun, S.; Su, D.; Xin, Q. *J. Phys. Chem.* **2007,** 111, 5605

43. Vidal-Iglesias, F.J.; Al-Akl, A.; Watson, D.J.; Attard, G.A. *Electrochem. Commun.* **2006**, 8, 1147

44. Ye, H.; Crooks, R.M. *J. Am. Chem. Soc.* **2007**, 129, 3627

45. Jong Yoo, S.; Park, H.Y.; Jeon, T.Y.; Park, I.S.; Cho, Y.H.; Sung, Y.E. *Angew. Chem. Int. Ed.* **2008**, 47, 9307

46. Liu, B.; Li, H.Y.; Die, L.; Zhang, X.H.; Fan, Z.; Chen, J.H. *J. Pow. Source.* **2009,** 186, 62

47. Hoshi, N.; Kida, K.; Nakamura, M.; Makada, M.; Osada, K. *J. Phys. Chem. B,* **2006**, 110, 12480

48. Wang, Y.J.; Wu, B.; Gao, Y.; Tang, Y.W.; Lu, T.H.; Xing, W.; Liu, C.P., *J. Pow. Sour.* **2009**, 192, 372

49. Yang, S.D.; Zhang, X.G.; Mi, H.Y.; Ye, X.G. *.J. Pow. Sour.*, **2008**, 175, 26

50. Ye, J.S.; Bai, Y.C.; Zhang, W.D. *Microchim. Acta.* **2009**, 165, 361

51. Xiao, L.; Zhuang, L.; Liu, Y.; Lu, J.T.; Abruna, H.D.; Hector, D. *J. Am. Chem. Soc.* **2009**, 131, 602

52. Shao, M.H.; Huang, T.; Liu, P.; Zhang, J.; Sasaki, K.; Vukmirovic, M.B.; Adzic, R.R. **2006**, *Langmuir*, 22, 10409

53. Xiao, L.; Zhuang, L.; Liu, Y.; Lu, J.T.; Abruna, H.D. *J. Am. Chem. Soc.*, **2009**, 131, 602

54. Kim, I.T.; Lee, H.K.; Shim, J. *J. Nanosci. Nanotech.* **2008**, 8, 5302

55. Gokacgac, G.; Leger, J.M.; Hahn, F. *A. J. Chem. Sci.* **2003**, 58, 423

56. Miyake, H.; Okada, T.; Samjeske, G.; Osawa, M. *Phys. Chem. Chem. Phys.* **2008,** 10, 3662

57. Xia, X. H.; Liess, H.-D.; Iwasita, T. *J. Electroanal. Chem.* **1997**, *437*, 233.

58. Speight , J.G. *Perry's Standard Tables and Formulas for Chemical Engineers*, McGraw-Hill, **2003**, p 227

59. Yeager, E.; Bockris, J.O.; Conway, B.E.; Sarangapani, S.; Comprehensive Treatise of Electrochemistry, *Electrodics: Experimental* Techniques, vol 9, Plenum Press, New York, **1984**

60. Lu, G.Q.; Sun, S.G.; Cai, L.R.; Chen, S.P.; Tian, Z.W.; Shui, K.K. *Langmuir* **2000**, 16, 778

Chapter 7

Introductory ATR-FTIR study of nitrophenol degradation based on bifunctional electrodes

7.1 Introduction

The establishment and enforcement of limits for the discharge and/or disposal of toxic and hazardous materials has required the development of new technology to effectively remediate a variety of gaseous and liquid effluents, solid waste and sludge. Photocatalysis and electrochemistry have been gaining considerable attention owing to their promising applications in water disinfection and hazardous waste remediation.[1-4] In the removal of pollutants from waste effluents, a number of methods have been studied including electrochemical oxidation[5-9], chemical adsorption[10-11] and photocatalytic degradation.[12-16] In photocatalytic degradation, titania (TiO_2) is considered as one of the most promising photocatalysts due to its low cost, high photocatalytic activity and chemical stability.[17-19] Upon irradiation with UV light, photoexcitation promotes electrons from the valence band to the conduction band of a photocatalyst, leaving highly oxidizing photogenerated holes behind.[20-23] On one hand, the photogenerated holes react with adsorbed water molecules and hydroxide anions to produce hydroxyl radicals which are able to degrade various pollutants. Since the oxidative process occurs at or near the surface of the photocatalyst, a high surface area is thus desirable to increase photocatalytic efficiency. To achieve a large surface area, one main approach is dispersing titania nanoparticles as a suspension into waste effluents.[24,25] However, this approach requires separation and recycling of the TiO_2 fine particles by filtration, which is inconvenient in the practical application of the photocatalytic treatment of wastewater. A second disadvantage is the photogenerated charge carriers (holes and electrons) have a tendency to recombine with one another. The high degree of recombination between the photogenerated electrons and holes is a

major limiting factor controlling photocatalytic efficiency. It has been reported that the recombination between the photogenerated charge carriers can be effectively suppressed by an electrochemical method, applying an external anodic bias.[26,27]

Electrochemistry also offers promising approaches for the elimination of environmental pollution.[7,28,29] Pollutants can be directly oxidized by hydroxyl radicals and chemisorbed active oxygen species generated by electrochemical anodic oxidation. A variety of anode materials including carbon, Pt, PbO_2, IrO_2, SnO_2, Pt-Ir and boron-doped diamond electrodes have been extensively investigated.[2,30] Recent studies in our lab have shown that the dimensionally stable anode (DSA) Ti/Ta_2O_5-IrO_2 exhibits excellent electrochemical activity and high stability for the electrochemical remediation of sulfide effluents.[31,32]

This chapter gives a report on a novel approach, a marriage of photocatalytic degradation and electrochemical oxidation and novel FTIR studies, to wastewater remediation based on the use of bifunctional electrodes. A titanium (Ti) plate was used as the substrate in fabricating the bifunctional electrodes because of its high corrosion-resistance and relatively low cost. The photocatalyst (TiO_2 thin film) was coated on one side of the Ti plate; while the electrocatalyst (Ta_2O_5-IrO_2 thin film) was coated on the other side. We thus call the prepared samples bifunctional electrodes. For the first time, our study shows that the application of an anodic potential bias not only greatly enhances the performance of the TiO_2 photocatalyst, but also effectively drives electrochemical oxidation of pollutants at the Ta_2O_5-IrO_2 electrocatalyst.

To illustrate this proposed novel environmental technique, 4-nitrophenol (4-NPh) and 2-nitrophenol (2-NPh) were chosen as the model pollutants and tested in this study. Nitrophenols are among the most common toxic persistent pollutants in industrial and agricultural wastewater. They are considered to be hazardous waste and priority toxic pollutants by the U. S.

Environmental Protection Agency.[33] Generally speaking, purification of wastewater polluted with 4-NPh or 2-NPh is very difficult as the presence of a nitro group in the aromatic ring enhances the stability of the nitrophenolic compounds in chemical and biological degradation.[34] This study demonstrates that the prepared bifunctional electrode exhibits superb activity for 4-NPh and 2-NPh degradation and that the innovative approach described here is very promising for water purification and waste effluent treatment. In order to further improve and understand this technique, the mechanism through which the nitrophenol compounds degrade is studied. There has been limited work done in monitoring photochemical degradation reactions *in-situ* at the photocatalyst surface.[35-39] Secondly, the species formed near the electrocatalyst surface are also of interest. ATR-FTIR spectroscopy will allow for both of these to be studied. The intermediates at the photocatalyst surface will be observed using the internal technique, while the electrocatalyst intermediates can be observed using analysis of the solution. This chapter will report on the development of bifunctional electrodes and the initial work done to identify the intermediates formed during the oxidation and degradation processes using ATR-FTIR.

7.2 Characterization of the prepared TiO_2/Ti/Ta_2O_5-IrO_2 electrodes.

SEM was employed to characterize the surface morphology and structure of the synthesized oxide coatings. As seen in Figure 7.1A, the TiO_2 coating prepared with the thermal decomposition method displays a typical "cracked-mud" structure. Figure 7.1B shows the SEM image of the Ta_2O_5-IrO_2 coating. Along with the cracked-mud structure, some small "islands" are present on the Ta_2O_5-IrO_2 surface. Figure 7.1C presents the EDS spectra of the bifunctional electrodes, confirming that the Ta_2O_5-IrO_2 coating was formed on one side of the Ti substrate and the TiO_2 coating was formed on the other side. In the EDS spectrum of the Ta_2O_5-IrO_2 coating, the small peak, labeled Ti^*, is derived from the Ti substrate. Quantitative analysis of the

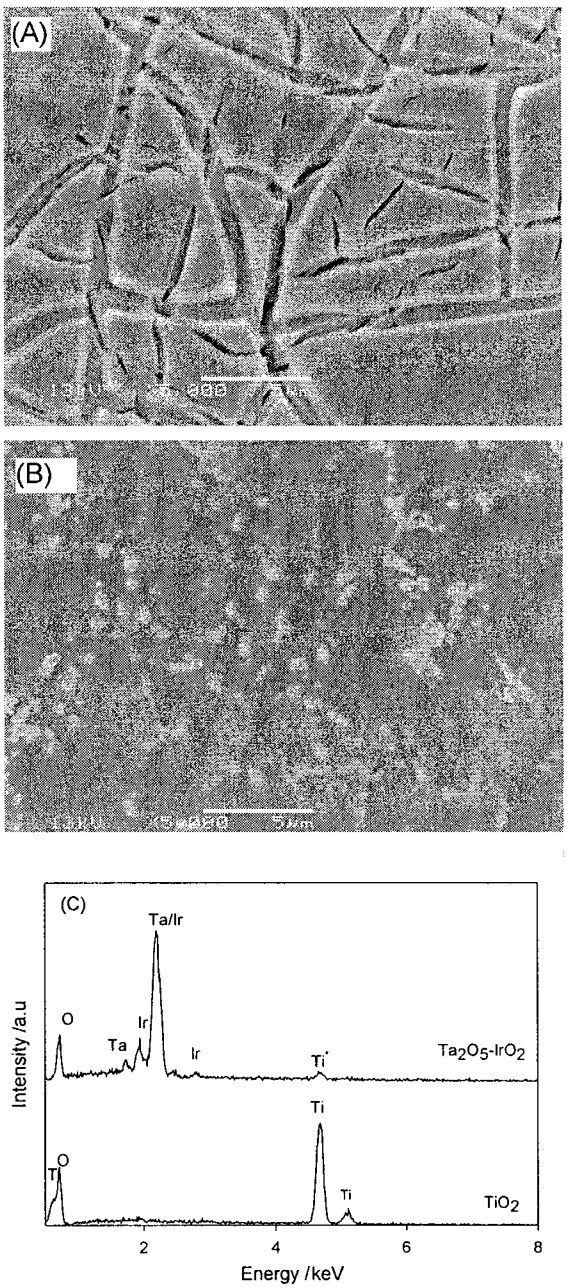

Figure 7.1 SEM images of A) TiO_2 displaying cracked mud structure, B) Ta_2O_5-IrO_2 electrocatalyst, C) EDS spectra of the TiO_2 and Ta_2O_5-IrO_2 catalysts

EDS spectrum reveals that the molar ratio of Ta_2O_5 to IrO_2 is 0.3 : 0.7 in the Ta_2O_5-IrO_2 coating, which is consistent with the composition of the Ta_2O_5-IrO_2 precursor solution.

To compare the induced photocurrent and electrochemical current of the bifunctional electrodes, linear voltammetric (LV) experiments at a potential scan rate of 20 mV/s in 0.15mM 4-NPh + 0.5M NaOH were performed on the TiO_2/Ti/Ta_2O_5-IrO_2 electrodes. The LV plots are presented in Figure 7.2A. In the absence of UV irradiation on the TiO_2 coating, the onset potential of oxygen evolution on the Ta_2O_5-IrO_2 coating is around 500 mV as shown in Curve *b*. The current is almost constant at potentials lower than 500 mV; the small current results from charging the electrical double layer when scanning the potential from -200 mV to 500 mV. Further scanning the potential from 500 to 800 mV, the electrochemical current undergoes a rapid linear increase due to oxygen evolution. Curve *a* is the LV plot of the TiO_2/Ti/Ta_2O_5-IrO_2 electrode in the presence of UV irradiation on the TiO_2 coating. Comparison of Curve *a* and *b* shows that: (i) the onset potential of the electrochemical oxygen evolution shifts from ~500 mV to ~450 mV upon the UV irradiation; (ii) the photocurrent created by the UV irradiation at potentials lower than 450 mV is ~2.5 mA arrived at by subtracting the double layer charging current (Curve *b*) from the total current (Curve *a*); and (iii) the UV irradiation creates a much larger current when the applied potential bias is higher than 450 mV. For instance, at 600 mV, the total current including the electrochemical current and the photocurrent of the TiO_2/Ti/Ta_2O_5-IrO_2 (Curve *b*) is 20.22 mA. This is much higher than the electrochemical current of the Ta_2O_5-IrO_2 coating (Curve *a*), 5.63 mA. We further measured the steady-state currents using the chronoamperometric (CA) method. The CA experiments were performed with a potential of 600mV applied with (Curve *c*) or without (Curve *d*) the UV irradiation. As seen in Figure 7.2B, under the applied 600 mV bias electrode potential, the electrochemical current of the Ta_2O_5-

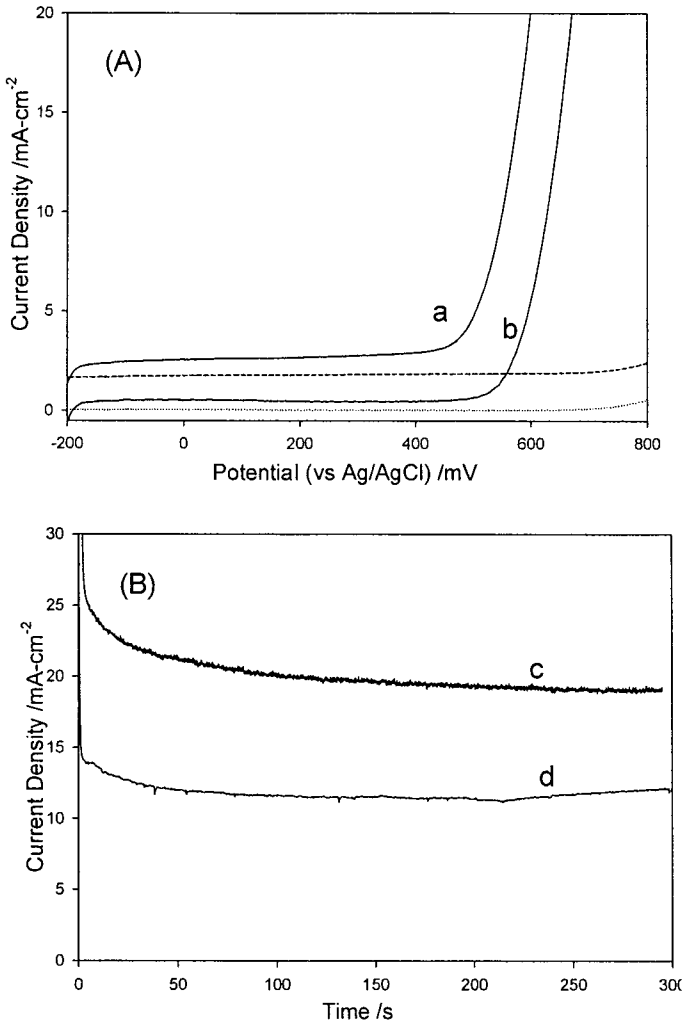

Figure 7.2 (A) Linear sweep voltammetric curves at 20 mV/s in 0.15mM 4-NPh + 0.5M NaOH: the $TiO_2/Ti/Ta_2O_5$-IrO_2 bifunctional electrode in the presence of (a) and in the absence of the UV irradiation (b); the TiO_2/Ti monofunctional electrode with (dashed line) and without the UV irradiation. (B) Steady state current of the $TiO_2/Ti/Ta_2O_5$-IrO_2 bifunctional electrode measured at 600mV in 0.15mM 4-NPh + 0.5M NaOH: under the UV irradiation (c); and without the UV irradiation (d)

$IrO_2/Ti/TiO_2$ electrode without the UV irradiation holds near steady at approximately 13 mA (Curve *d*); in contrast, upon the UV irradiation, the steady-state current reaches a level of over 20 mA (Curve *c*), showing a significant synergetic effect of the UV irradiation and the applied electrode potential on the induced current of the bifunctional electrode.

7.3 Degradation of 4- and 2- Nitrophenol

The performance of the fabricated bifunctional electrodes was tested using 4-NPh as a model pollutant. UV-Vis spectroscopy was employed to monitor the absorbance of 4-NPh *in-situ* during the degradation experiments. Figure 7.3 presents the scanning kinetics graphs taken at 15-minute intervals during the degradation of 4-NPh: on the $TiO_2/Ti/Ta_2O_5$-IrO_2 bifunctional electrode under the UV irradiation only (A). The main absorption band centered at 400nm is representative of the amount of 4-NPh in solution. The decrease of the intensity of this peak over time is confirmation of the degradation of 4-NPh. In addition, a new band appears at ca. 320 nm, indicating that intermediates are formed during the degradation of 4-NPh. After rising to its maximum intensity, the new band begins to decrease and finally disappears, demonstrating that the intermediates are also completely oxidized. Figure 7.3A shows the results of the photochemical degradation of 4-NPh using the $TiO_2/Ti/Ta_2O_5$ bifunctional electrodes under the UV irradiation but without any external anodic potential bias. This method gives very little degradation with the $TiO_2/Ti/Ta_2O_5$-IrO_2 electrode, only degrading 6.9% over 180 min.

The benefit from the application of a potential bias to a photocatalyst is illustrated in Figure 7.3B. Here the TiO_2/Ti photocatalytic electrode was held at 600 mV with UV irradiation. 32% of 4-NPh was degraded over 180 min. The energy from the anodic potential bias resulted in slowing of the rate of recombination of electrons and holes, giving better results than without anodic potential bias.

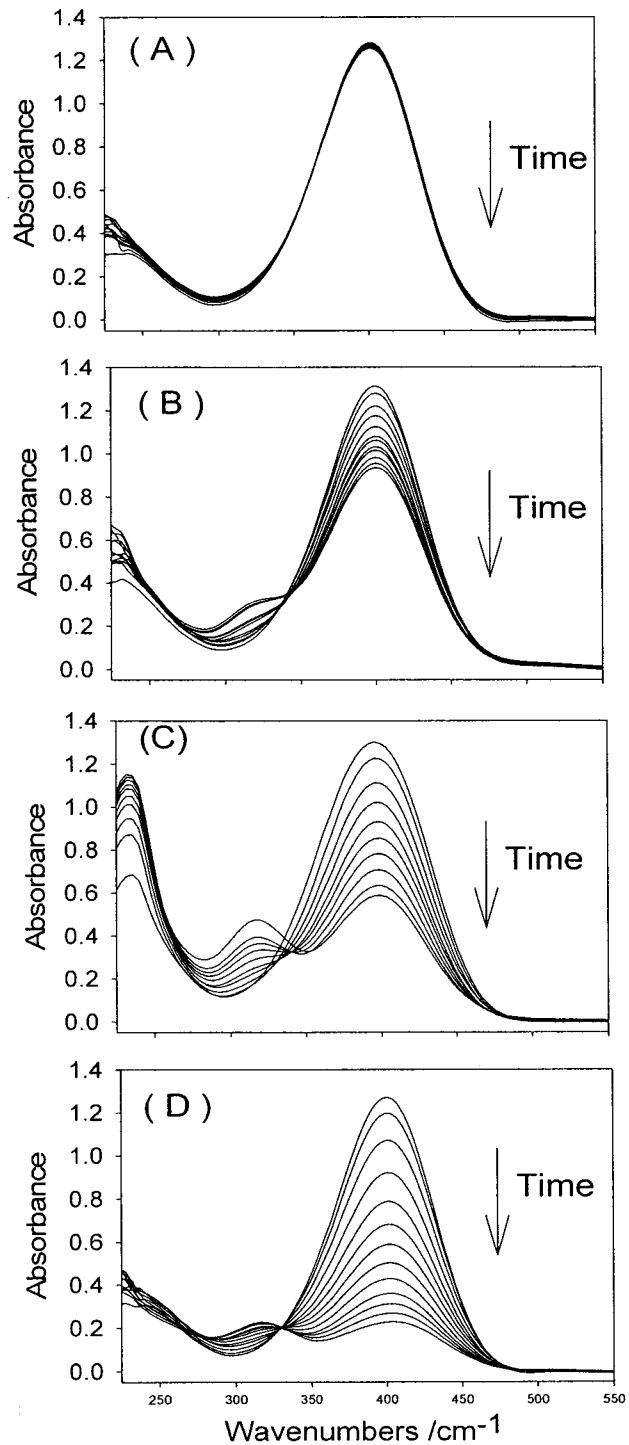

Figure 7.3 *in-situ* UV-Vis spectra acquired in 0.15mM 4-NPh + 0.5M NaOH during: (A) photochemical oxidation on the TiO_2/Ti/Ta_2O_5-IrO_2 bifunctional electrode under the UV irradiation only; (B) the TiO_2/Ti monofunctional electrode under the UV irradiation and with 600 mV applied electrode potential; photoelectrochemical oxidation at 600mV by TiO_2/Ti, (C) electrochemical oxidation at 600 mV(D) combination of UV irradiation and electrochemical oxidation at 600mV.

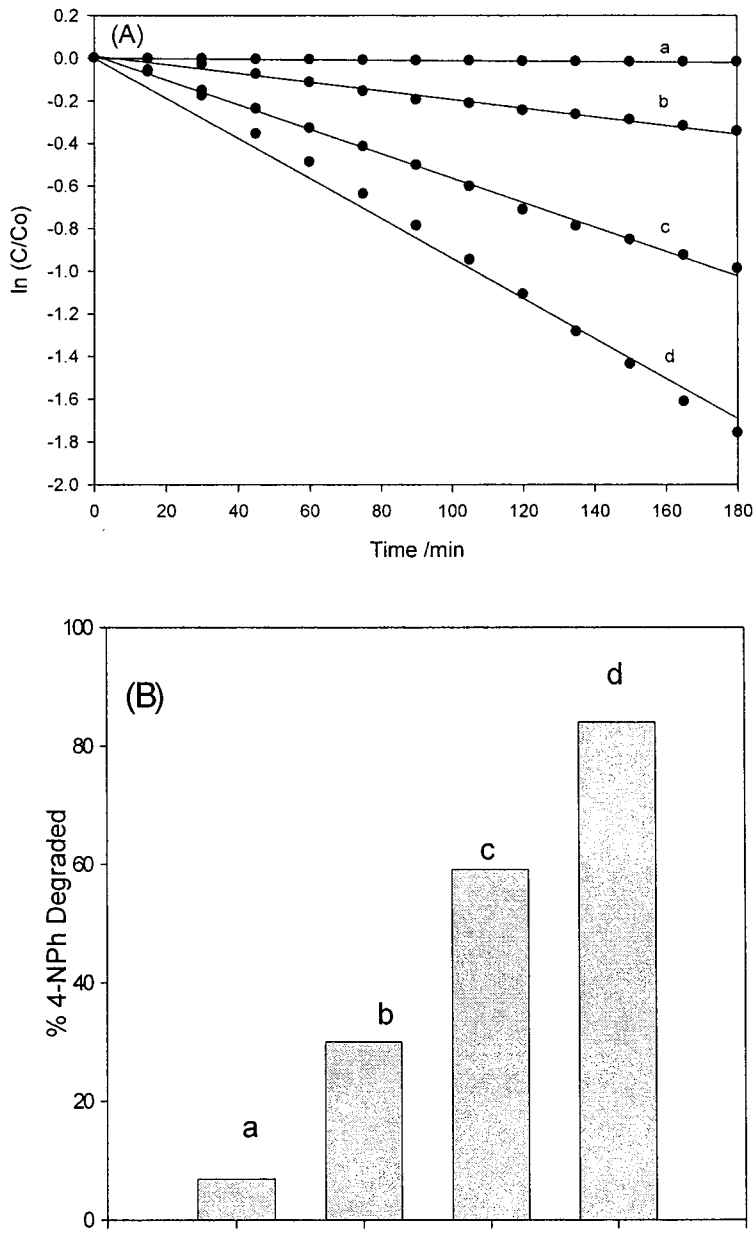

Figure 7.4 (A) Plot of the ln C/Co of 4-NPh from Fig 3 over time for determination of experimental rate constant (a) UV irradiation of bifunctional electrode, (b) photoelectrochemical oxidation by TiO_2/Ti at 600mV, (c) electrochemical oxidation at 600 mV on bifunctional electrode (d) combination of UV irradiation and electrochemical oxidation on bifunctional at 600mV. (B) comparison of the percentage of initial 4-NPh degraded over the span of three hours using the three previous methods

The performance of the electrochemical face of the bifunctional electrode is shown in Figure 7.3C. Here an anodic potential bias of 600 mV is applied to the $TiO_2/Ti/Ta_2O_5$-IrO_2 electrode without any irradiation of the photocatalyst. Over the span of 3 hours, 59.1% of the 4-NPh is removed through electrochemical oxidation.

The novel technique of combining photochemical degradation and electrochemical oxidation was tested by irradiating the bifunctional $TiO_2/Ti/Ta_2O_5$-IrO_2 electrode with UV light and applying a potential of 600 mV. Very promising results are observed. The combination results are seen in Figure 7.3D; a degradation of 83% of 4-NPh over three hours.

The concentration of 4-NPh in solution decreases with time during the degradation experiments. Using a calibration curve, the absorbance value of the 400 nm peak can be related back to the concentration of the 4-NPh. Figure 7.4A presents the corresponding ln c/c_o *vs.* t plots for the tests reported in Figure 7.3. The linear relationship of ln c/c_o *vs.* t shows that the degradation of 4-NPh using either the monofunctional or bifunctional electrodes follows pseudo-first order kinetics:

$$\ln\frac{c}{c_0} = -kt \qquad \textbf{(1)}$$

where c/c_0 is the normalized 4-NPh concentration, t is the reaction time, and k is the reaction rate constant in term of min^{-1}. The $TiO_2/Ti/Ta_2O_5$-IrO_2 electrode under the UV irradiation but without any external anodic potential bias has the lowest photochemical degradation rate constant, 1.11 $x10^{-4}$ min^{-1}, Figure 7.4 A(a), caused by the high degree of recombination between the photogenerated electrons and holes. As shown in Figure 7.4A(b), the photoelectrochemical rate constant of the TiO_2/Ti electrode at the applied electrode potential 600 mV with UV irradiation is $2.03x10^{-3}$ min^{-1}. This is much larger than the slope of (a), demonstrating that the applied potential bias effectively suppressed recombination between the photogenerated

electrons and holes. Figure 7.4A(c), from the electrochemical oxidation of 4NPh gives a rate constant of 5.74×10^{-3} min^{-1}. Among the four plots, Figure 7.4A(d) for the $TiO_2/Ti/Ta_2O_5$-IrO_2 bifunctional electrode at the applied electrode potential 600 mV and upon UV irradiation has the highest slope, 1.06×10^{-2} min^{-1}, demonstrating the huge benefits of the marriage of photocatalytic degradation and electrochemical oxidation for the environmental remediation of organic pollutants. All of the above listed rate constants can be seen in Table 7.1.

The benefit of the new method can also be seen in the total amount of 4-NPh degraded during the three hour experiments. Figure 7.4B gives a graphical representation of the total amount of 4-NPh removed from solution by the methods (a) photochemical, (b) photoelectrochemical, (c) electrochemical, (d) bifunctional. The combination of photochemical degradation and electrochemical oxidation degraded more than double the amount of the two individual methods combined.

To further test the strengths of this novel method, a second compound, 2-NPh, was used in degradation studies. Again, an initial concentration of 0.15mM 2-NPh in 0.5 M NaOH was used, and the resulting UV absorption spectra show a main absorption band at 412nm, which corresponds to the concentration of 2-NPh. The appearance of the secondary band at ~320 nm, can be accredited to the formation of various aromatic ring intermediates in solution. Figure 7.5 shows the kinetic plots, taken every 15 minutes for 90 minutes, of the 2-NPh using the following degradation methods. Figure 7.5A shows the UV irradiation of a $TiO_2/Ti/Ta_2O_5$-IrO_2 electrode without an electrochemical anodic bias. Over three hours, only 16% of the 2-NPh is degraded, a very low value and a similar result to that of the 4-NPh.

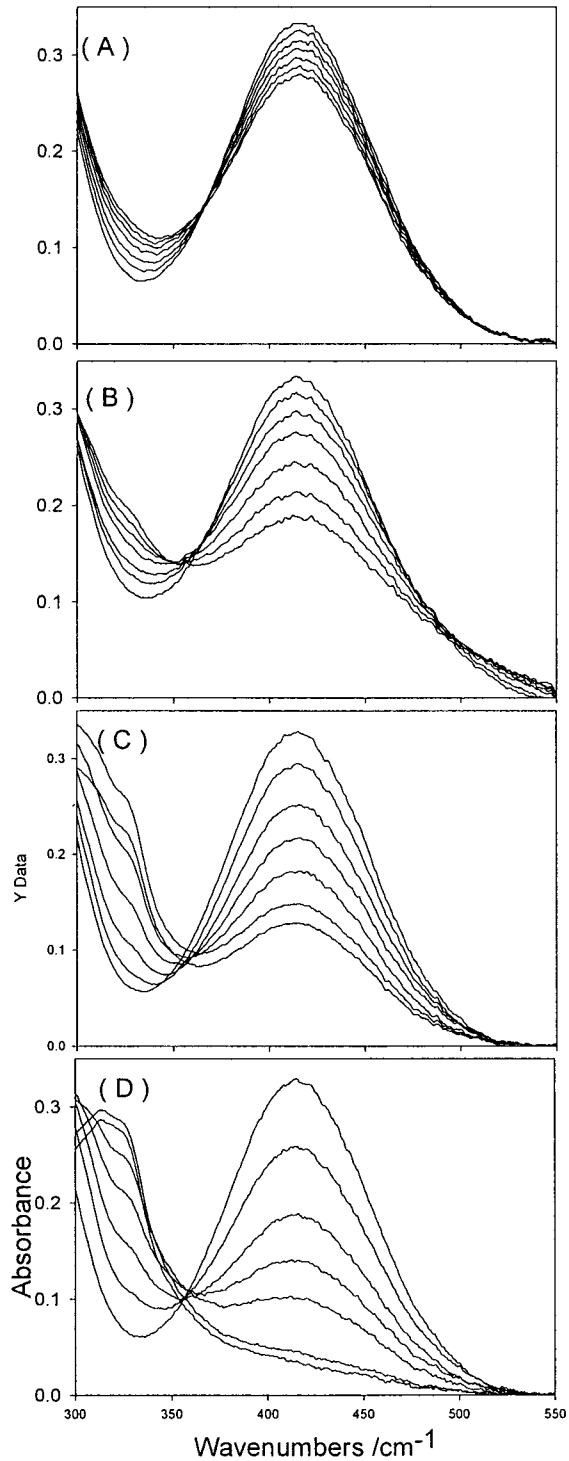

Figure 7.5 *in-situ* UV-Vis spectra from 0.15mM 2-NPh in 0.5 M NaOH collected every 15 minutes using the following degradation methods (A) UV irradiation of bifunctional electrode, (B) photoelectrochemical oxidation by TiO_2/Ti at 600mV, (C)electrochemical oxidation at 600 mV (D) combination of UV irradiation and electrochemical oxidation on bifunctional at 600 mV

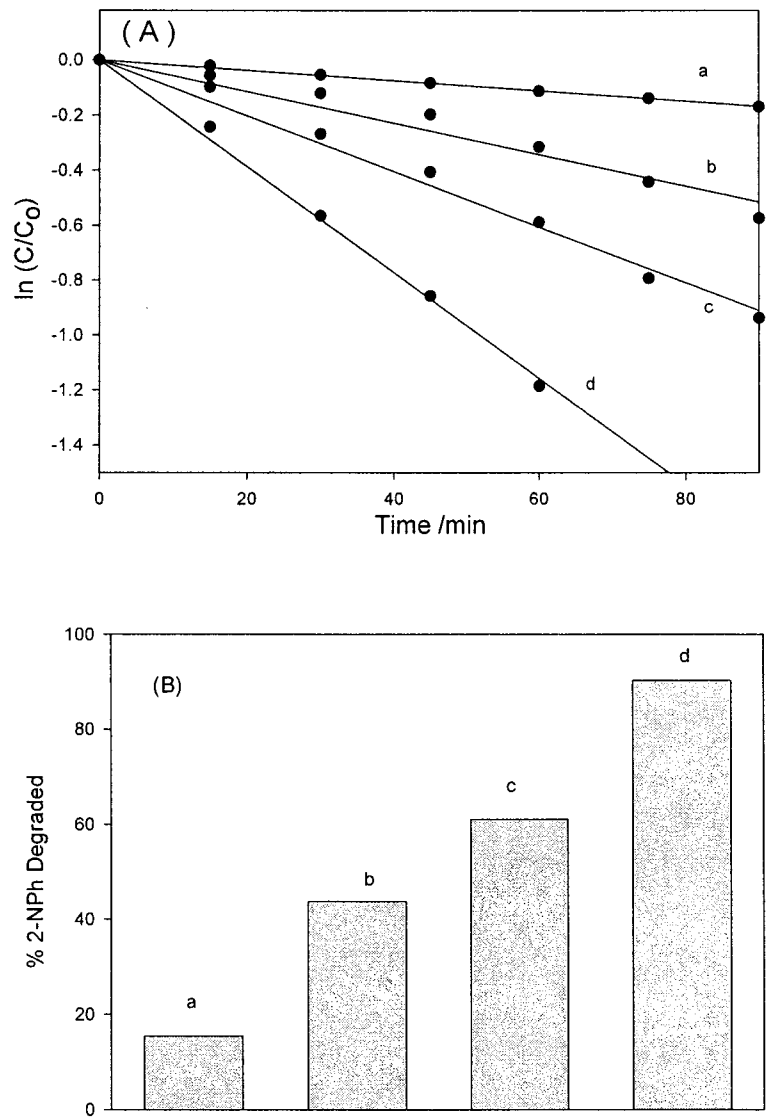

Figure 7.6 (A) Plot of the log C/Co of 2-NPh over time for determination of experimental rate constant for (a) UV irradiation of bifunctional electrode, (b) photoelectrochemical oxidation by TiO_2/Ti at 600mV, (c) electrochemical oxidation at 600 mV using bifunctional electrode (d) combination of UV irradiation and electrochemical oxidation on bifunctional at 600 mV (B) comparison of the percentage of initial 2-NPh degraded over the span of three hours using the previous three methods

Upon applying a potential bias of 600mV and no UV irradiation to a $TiO_2/Ti/Ta_2O_5$-IrO_2 electrode, 43.7% of the 2-NPh was removed in three hours (Figure 7.5B). Again we see an improvement of the photocatalyst through the application of a potential bias.

The electrochemical face of the bifunctional electrode on its own, Figure 7.5C, shows the greatest level of degradation than the previous two methods, removing 61% of 2-NPh over the span of 3 hours.

The performance of the novel bifunctional electrodes shows a great level of effectiveness in the degradation of 2-NPh. Through UV irradiation and the application of a potential bias, 90.3% of the initial 2-NPh was degraded as shown in Figure 7.5D.

The bifunctional electrode degraded an amount 46% greater than the photoelectrochemical method and at a much greater degradation rate. When viewing the experimental rate constants, calculated using a calibration curve from the 412 nm absorption band in the UV spectra, the bifunctional electrode showed the highest rate with a value of $1.93x10^{-2}$ min^{-1}. This is over triple the rate given by the sole photoelectrochemical degradation, $5.27x10^{-3}$ min^{-1}, while the poor performing UV only experiment lead to a nearly double rate constant of $1.86x10^{-3}$ min^{-1}. The electrochemical oxidation of 2-NPh produced a rate constant of $9.88x10^{-3}$ min^{-1}. All of these values were calculated from the slope of a log c/c_o vs. t plot displaying pseudo-first order kinetics (Figure 7.6A) and are reported in Table 7.1. Figure 7.6B shows the comparison of the total amount of 2-NPh removed in the 90-min experiment for all four degradation methods, once again illustrating the advantages of the bifunctional electrode.

Experiments	Photochemical	Photoelectrochemical	Electrochemical	Combination Bifunctional
4-NPh	$1.11x10^{-4}$ min^{-1}	$2.03x10^{-3}$ min^{-1}	$5.74x10^{-3}$	$1.06x10^{-2}$ min^{-1}
2-NPh	$1.86x10^{-3}$ min^{-1}	$5.72x10^{-3}$ min^{-1}	$9.88x10^{-3}$	$1.93x10^{-2}$ min^{-1}

Table 7.1 Comparison of the different rate constants derived from Figures 4 and 5 for the various degradation experiments carried out in this study.

From these rate constants, it can be seen that the degradation of 2-NPh is much easier than that of 4-NPh. This is expected due to 4-NPh's higher level of stability and this can be used to explain the smaller difference in total degradation between the novel bifunctional and photoelectrochemical methods when compared to those with 4-NPh. The rate at which the 2-NPh is degraded is much greater for the bifunctional photoelectrochemical method. Therefore the bifunctional electrodes are very successful in the degradation of pollutants, to further improve the performance, the reactions at each catalyst surface must be understood.

7.4 ATR-FTIR study of nitrophenol degradation

The reaction at the photocatalytic TiO_2 surface is to be studied first, using 4-nitrophenol. Upon adding the nitrophenol solution to the ATR-FTIR cell, the solution rested for 5 min, the background $R_{(E1)}$ spectrum used was the final spectrum collected in the dark. The UV light was then applied, and immediately the first $R_{(E2)}$ spectra collected, then again after 15 min. The resulting spectra are displayed in Figure 7.7. Many peaks appear as the reaction progresses with time, first a negative going band at 3642 cm^{-1} grows with time, as does a band at 1680 cm^{-1} due to water being brought to the TiO_2 surface to be activated to hydroxyl species. The negative going bands at 2924 cm^{-1} and 2860 cm^{-1} are brought upon by –CH and CH_2 groups, being

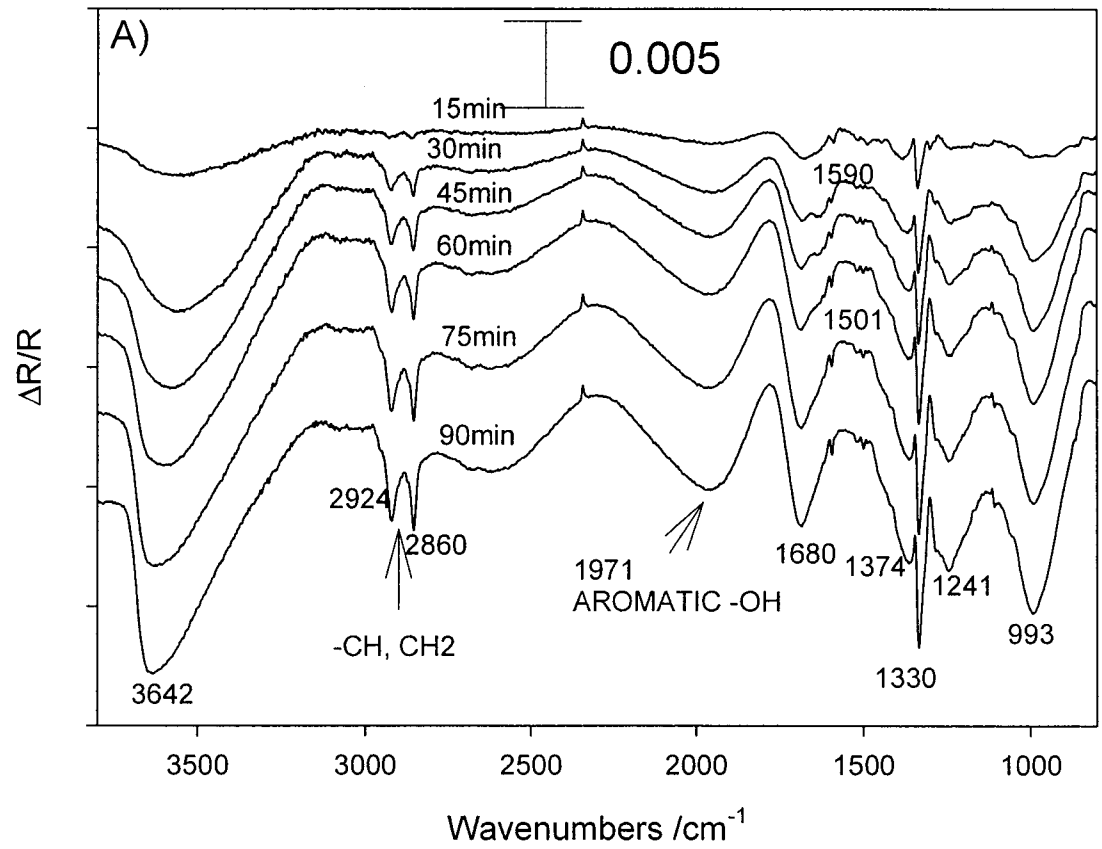

Figure 7.7 The degradation of 4-NPh on TiO_2 monitored with internal ATR-FTIR, a base spectra was collected in the dark and subsequent spectra collected every ten minutes

present at the TiO_2 surface in larger amounts, as the 4-NPh is brought to the surface to be directly degraded by the photocatalyst. A very interesting band is the one which grows at 1971 cm^{-1}. This band arises from aromatic –OH groups[40]. Other bands and their assignments are presented in Table 7.2:

Band	Direction	ID
3642	negative	Ti-surface OH- radical[40]
2920	negative	-C-H
2860	negative	-C-H of (CHO)
1971	negative	Aromatic OH[39]
1680	negative	H_2O
1590	negative	N-H amine[41]
1501	negative	Aromatic C=C[41]
1374	negative	C-H alkane
1330	negative	Nitro NO_2
1241	negative	C-O[41]
993	negative	C-O

Table 7.2 Spectral assignments from Figure 7.7

These results indicate what is occurring at the TiO_2 surface. First, we observe both water and the 4-NPh being brought to the catalyst surface; the 4-NPh to be directly degraded and the water to form –OH radicals. These radicals can then attack the 4-NPh ring at the surface, creating more aromatic –OH groups, represented by the band at 1971 cm^{-1}. This leads to the presentation of the other bands below 1650 cm^{-1} as the 4-NPh is degraded. From this increase in the C-O bands characteristic of aromatic alcohols, the attack via the OH radicals is observed, the increase in the nitro groups at the surface is due to increased amounts of 4-NPh being brought to the catalyst surface, as well as the aromatic C=C band.

Following this, the external ATR-FTIR set-up was employed to monitor the electrochemical oxidation of 4-NPh. A thin layer solution in 0.01M 4-NPh + 0.1M NaOH was prepared with a Ti/Ta_2O_5-IrO_2 bulk electrode. A potential of 600 mV was selected to simulate

the electrochemical studies, with the $R_{(E1)}$ spectra collected at the beginning of the potential application and the $R_{(E2)}$ subsequently in 15 min intervals. This spectral series is displayed in Figure 7.8. A negative going band appears in the standard water region, however, below 1650 cm^{-1} there are five bands which grow more negative as they are produced in larger amounts, the summary of their identification is seen in Table 7.3 below.

Band	Direction	ID
1647	Negative- broad	H_2O
1582	Negative- med	-NH amine
1492	Negative – weak	-C-H of (CHO)
1292	Negative – med	CO stretch from carboxylic acid
1174	Negative – weak	C-N
1117	Negative- med	C-O stretch

Table 7.3 Spectral assignments for Figure 7.8

The mechanism of the electrochemical degradation of 4-NPh has been suggested in literature[42] with intermediates such as p-aminophenol, benzoquinone, malonic and maleic acid being suggested. Our results can elucidate this process as they reflect the monitoring of the solution close to the electrode surface. As new species are formed, they will appear in the spectra. The band at 1647 cm^{-1} is observed as water is a product of the steps of the electrochemical oxidation of 4-NPh. One of the first steps is the conversion of 4-NPh to p-aminophenol, with the only difference being an amine instead of nitro group. This would be the cause of the 1582 cm^{-1} band, which grows with time. At 1492 cm^{-1} a weak band appears due to the –CH stretch of a CHO group, an increased amount of this group corresponds to the attack of the nitrophenol from OH species formed at the electrocatalyst surface. There is no increase in aromatic C=C bands, thus ruling out these bands resulting from to new nitrophenol entering the thin layer. At 1292 cm^{-1} the CO stretch of a carboxylic acid is observed, and there are several

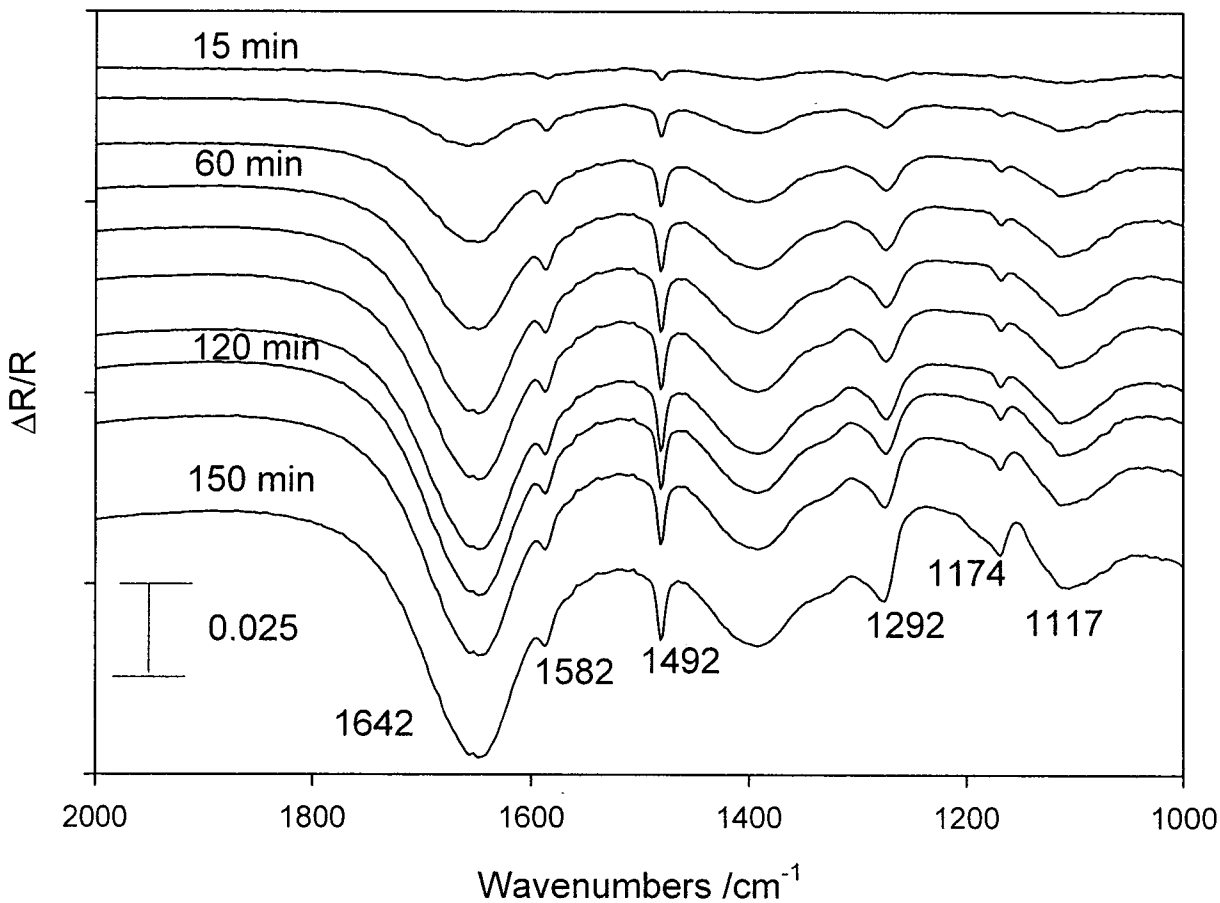

Figure 7.8 The electrochemical degradation of 4-NPh using a Ta_2O_5-IrO_2/Ti electrode monitored with the external ATR-FTIR technique

carboxylic acids formed such as malonic and maleic. This band grows at the largest rate, suggesting the formation of several acids is occurring. A C-N stretch from an amine is present as a characteristic weak band at 1174 cm^{-1}, and appears and grows at a similar rate to the N-H band at 1582 cm^{-1}. Finally the band at 1117 cm^{-1} is due to a C-O stretch. Several of the suggested intermediates can be observed in these spectra, by eventually combining this technique with other techniques such as HPLC or MS, a confirmed mechanism will be gathered.

7.5 Summary

In summary, this chapter viewed initial work done in the identification of the degradation mechanism of 4-NPh based on the use of bifunctional electrodes. I have demonstrated a novel and facile approach for wastewater treatment based on the use of bifunctional electrodes with the presence of electrocatalysts (i.e. Ta_2O_5-IrO_2) on one face and photocatalysts (i.e. TiO_2) on the other face. This innovative approach has four major advantages: (i) as the photocatalysts are coated on the Ti substrate, the tedious procedure for separation and recycling of the TiO_2 suspension in the waste effluents is avoided; (ii) an anodic potential bias can be easily applied to the bifunctional electrode, thus effectively suppressing the recombination of photogenerated electrons and holes on the photocatalyst face; (iii) full use of the extra applied energy as it can also drive the electrocatalyst; and (iv) the anodic potential bias applied to the bifunctional electrode promotes hydroxyl radical formation and oxygen evolution at the electrocatalyst face. This oxygen can move to the surface of the TiO_2 catalyst and scavenge the conduction band electrons to form superoxide ions (O_2^{*-})[1], further decreasing the recombination of the photogenerated charge carriers. The produced superoxide ion can also act as an oxidant to mineralize organic pollutants. The prepared TiO_2/Ti/Ta_2O_5-IrO_2 bifunctional electrode exhibits

superb activity for 4-NPh and 2-NPh degradation and the approach described in this study provides a very promising environmental technology for water purification and waste effluent treatment. To further improve upon this work, the ATR-FTIR systems were utilized to begin to monitor the degradation of 4-NPh at both the electrocatalyst and photocatalyst surfaces. At the TiO_2 it was found that both water species and 4-NPh are observed at the TiO_2 surface, with hydroxyl radicals attacking the 4-NPh ring, forming more aromatic OH groups, eventually leading to complete degradation. At the electrochemical face, the FTIR results show some of the intermediate groups formed during the oxidation of 4-NPh such as increased C-O stretches of carboxylic acid groups and standard amine stretches appearing in the solution close to the catalyst surface. These studies are essential to improving the already successful bifunctional electrodes.

7.6 References

1. Augugliaro, V.; Litter, M.; Palmisano, L.; Soria, J. *J. Photochem. Photobiol. C: Photochem Rev.* **2006**, 7, 127

2. Martinez-Huitle, C.A.; Ferro,. *Chem. Soc. Rev.* **2006,** 35, 1324

3. Xu, C.; Killmeyer, R.; Gray, M.L.; Khan, *Electrochem. Commun.* **2006**, 8, 1650

4. Allan, N.S; Edge, M.; Verran, J.; Stratton, J.; Maltby, J.; Bygott, C.. *Poly. Degrad. Stab.* **2008**, 93, 1632

5. Ezerskis, Z.; Jusys, Z.. *J. App. Electrochem.* **2002**, 32, 543

6. Zhu, X.; Shi, S.; Wei, J.; Lu, F.; Zhao, H.; Kong, J.; He, Q.; Ni, J.. *Environ. Sci. Technol.* **2007**, 41, 6541

7. Tian, M.; Bakovic, L.; Chen, A. *Electrochim. Acta,* **2007**, 52, 6517

8. Raju, T.; Chung, S.J.; Pillai, K.C.; Moon, I.S. *Clean-Soil. Air Wat.* **2008**, 36, 476

9. Martinez-Huitle, C.A.; De Battisti, A.; Ferro, S.; Reyna, S.; Cerro-Lopez, M.; Quiro, M.A.. *Environ. Sci. Technol.* **2008**, 42, 6929

10. Chai, X.L.; Zhao, Y.C. *J. Hazard. Mat.* **2006,** 138, 116

11. Pena, M.; Meng, X.; Korfiatis, G.P.; Jing, C. *Environ. Sci. Technol.* **2006**, 40, 1257

12. Christensen, P.A.; Egerton, T.A.; Kosa, S.A.M.; Tinlin, J.R.; Scott, K. *J. App. Electrochem.* **2006**, 35, 683

13. Malpass, G.R.P.; Miwa, D.W.; Miwa, A.C.P.; Machado, A.S.; Motheo, A.J.. *Environ. Sci. Technol.* **2007**, 41, 7120

14. Peng, X.; Chen, A. *Adv. Funct. Mater.* **2006**, 16, 1355

15. Ye, X.J.; Chen, D.; Li, K.Y.; Shah, V. . *Chem. Eng. Commun.* **2007**, 194, 368

16. Liu, Z.Y.; Zhang, X.T.; Nishimoto, S.; Mruakami, T.; Fujishima, A.. *Environ. Sci. Technol.* **2008**, 42, 8547

17. Fujishima, A.; Rao, T.N.; Tryk, D.. *J. Photochem. Photobio. C: Photochem. Rev.* **2000**, 1, 1

18. Amano F.; Yamaguchi T.; Tanaka T.. *J. Phys. Chem. B*, **2006,** 110, 281

19. Xu, T.; Cai, Y.; O'Shea, K.E. *Environ. Sci. Technol.* **2007**, 41, 5471

20. Chen, A.; Peng, X.; Holt-Hindle, P. In *Frontal Nanotechnology Research*; M. V. Berg, M.V., Ed.; Nova Science Publishers, Inc., **2007**; 131

21. Ryu, J.; Choi, W. *Environ. Sci. Technol.* **2006**, 40, 7034

22. Amano F.; Suzuki S.; Yamamoto T.; Tanaka T.. *Appl. Catal. B. Environ.* **2006**, 64, 282.

23. Yoon, S.H.; Lee, J.H.. *Environ. Sci. Technol.* **2005**, 39, 9695

24. Nosaka Y.; Koenuma K.; Ushida K.; Kira A. *Langmuir,* **1996**, 12, 736

25. Lair, A.; Ferronato, C.; Chovelon, J.M.; Herrmann, J.M. *J. Photochem. Photobio. A.: Chem.* **2008**, 193, 193

26. Agrios, A.; Pichat, P.. *J. Appl. Electrochem.* **2005**, 35, 655

27. Wu, G.; Nishikawa, T.; Ohtani, B.; Chen, A.. *Chem. Mater.* **2007**, 19, 4530

28. Canizares, P.; Martinez, F.; Jimenez, C.; Lobato, J.; Rodrigo, M.A. *Environ. Sci. Technol.* **2006**, 40, 6418

29. Wang, J.W.; Bejan, D.; Bunce, N.J.. *Ind. Eng. Chem Res.* **2005**, 44, 3384

30. Comninellis, C.. *Electrochim. Acta*, **1994**, 39, 1857

31. Chen, A.; Miller, B.;. *J. Phys. Chem. B*, **2004**, 108, 2245

32. Miller B.; Chen, A.. *Electrochim. Acta*, **2005**, 50, 2203

33. 4-Nitrophenol Health and Environmental Effects Profiles No. 135, U.S. Environmental Protection Agency (EPA), U.S. Government Printing Office, District of Columbia, **1980**

34. Quiroz, M.A. ; Reyna, S. ; Martinez-Huitle, C.A. ; Ferro, S.; De Battisti, A. *App. Catal. B: Environ.* **2005,** 59, 259

35. Kibanov, D.; Trejo, M.; Destaillats, H.; Silva, J.C. *Appl. Clay. Sci.* **2009**, 42, 563

36. Augugliaro, V.; Loddo, V.; Lopez-Munoz, M.J.; Marquez-Alvarez, C.; Palmisano, G.; Palmisano, L.; Yurdakal, S. *Photochem. & Photobio Sci.* **2009,** 8, 663

37. Tryba, B.; Inagaki, Toyoda, M.; Morawski, A.W. *J. Adv. Oxi. Tech.* **2007**, 10, 25

38. Arana, J.; Tello-Rendon, E.; Dona Rodriguez, J.M.; Herrera J.A.; Gonzalez, O.; Perez Pena, J. *Chemosph.* **2001**, 44, 1017

39. Vargas R.; Nunez, O. *J. Mol. Catal. A.: Chem.* **2009,** 300, 65

40. Nakamura, R.; Imanshi, A.; Murakowski, K.; Nakato, Y. *J. Am. Chem. Soc.* **2003**, 125, 7443

41. Speight , J.G. *Perry's Standard Tables and Formulas for Chemical Engineers*, McGraw-Hill, **2003**, 227

42. Liu, Y.; Liu H.; Li, Y. *Appl. Catal. B: Enviro.* **2008**, 84, 297

Chapter 8

Summary and Future work

Fourier Transform Infrared Spectroscopy is a very powerful technique for the analysis of reactions occurring near the surface of an electro- or photocatalyst. The Attenuate Total Reflection technique overcomes several of the problems surrounding *in-situ* electrochemical FTIR including interference from the bulk electrolyte solution. In this work, two *in-situ* electrochemical FTIR systems were developed, an internal system for monitoring of surface species at a thin film catalyst and an external system for the monitoring of species which desorb into the bulk solution. These systems were applied in a wide range of studies on nanostructured materials for fuel cell applications, non-enzymatic chemical sensing and wastewater treatment.

The ATR-FTIR systems were built in-house using Teflon© electrochemical cells. The initial tests were performed to discover the set conditions to be employed throughout the work presented. Upon design of the systems, they were tested using standard reactions. The internal system used a sputtered Pt electrode and the oxidation of CO, showing the ability of the system to identify both CO and CO_2 at the catalyst surface. The external system was tested using the oxidation of methanol at Pt electrode, and the resulting spectra displayed both products and reactants. To further test the internal system, nanoporous Pt was tested in the oxidation of two simple fuel systems, CO and formic acid.

With both systems developed, a complete study on the enhancement of the PtRu catalyst with the addition of Ir was performed. This catalyst, fabricated using the hydrothermal technique, was tested electrochemically with Pt and PtRu. In the oxidation of methanol, the PtRuIr outperforms the PtRu by ~15% with the addition of 15% Iridium. This improvement

comes from a change in behaviour of the OH species present at the catalyst surface, the Ir lowering the onset potential for the oxidation of methanol and the trimetallic catalyst performing at a higher rate than with the Pt and PtRu. This information was gathered using both the internal and external ATR-FTIR systems.

The ATR-FTIR systems were also used to study more complex reactions occurring at the surface of Pt-based nanomaterials. The electro-oxidation of glucose was monitored for four separate catalysts, Pt, PtRu, PtIr and PtPb, each of which have shown promise as potential glucose chemical sensors. It is the oxidation of glucose which generates the current response needed for a functional sensor, and each catalyst shows this sensitivity. In the analysis of data gathered from both the internal and external systems, it was found that PtPb shows the highest performance, and greatest potential for a chemical glucose sensor, due to a lack of CO present at the catalyst surface in the complete oxidation of glucose to CO_2. Intermediate information is also gathered in this study as evidence of a 5-member lactone as well as several C-O and C-OH containing groups are observed as well.

PtPb can serve not only as a potential glucose sensor, but also in a more complex structure in the oxidation of potential fuels. Both PtPb and PtPd nanodendrites were fabricated with the hydrothermal technique and studied for their performance in formic acid and methanol oxidation, respectively. The PtPb nanodendrites undergo a phase transition to a hexagonal phase with increased Pb levels. Through this transition the activity towards formic acid oxidation is increased due to a conversion from the dehydration pathway to the dehydrogenation pathway. This change in mechanism was confirmed using the internal ATR-FTIR system. A series of PtPd nanodendrites were tested in the oxidation of methanol, with a PtPd (50:50) catalyst showing the strongest performance. From the ATR-FTIR data, a synergistic effect between the

Pt and Pd is suggested. Pd lacks activity towards methanol oxidation, yet outperforms pure Pt in the oxidation of formic acid. The Pt in the nanodendrite structure is used to catalyze the initial steps of methanol oxidation, while Pd is present to strongly oxidize the smaller intermediates, such as formate, to CO_2.

Finally, the versatility of the system was tested for the monitoring of the degradation of 4-NPh at both a photocatalyst and electrocatalyst surface. This study was developed based on the fabrication and performance of novel bifunctional electrodes which are made up of a photocatalytic face and, on the opposite face, an electrocatalytic face. These electrodes perform strongly in the degradation of both 4- and 2-NPh, and present a potential green method for waste water remediation. The reactions occurring at each face were studied with ATR-FTIR, with the internal system identifying important intermediates such as Ti-OH radicals and aromatic –OH groups. The external system studied the electrochemical degradation of nitrophenol, showing increased nitro groups as well as C-OH containing intermediates being present during the oxidation of 4-NPh.

In summary, two separate ATR-FTIR systems, one for surface analysis and the second to monitor solution species were successfully designed and developed. These systems were able to garner useful information in a wide range of applications of nanostructured materials and will continue to be a strong asset in our laboratory. The technique will be further applied in all studies of Pt-based nanomaterials in our laboratory. In the study of the glucose oxidation mechanism, further tests using the successful PtPb and PtIr catalysts will be performed using the 5-member lactone ring as a starting molecule. The FTIR data can also be compared with chromatography and mass spectrometry data to fully identify the intermediate species. The

technique will also be widely used in the study of the degradation pathways of many organic pollutants in both photochemical and electrochemical processes.